

Search for Gluinos in the final states with Jets, Leptons and Missing transverse momentum in the ATLAS Experiment.

Shion Chen ^{*}

Department of Physics, Graduate School of Science, The University of Tokyo
7-3-1, Hongo, Bunkyo-ku, 113-0033, Tokyo, Japan

^{*}chen@icepp.s.u-tokyo.ac.jp

Contents

1	Introduction	2
1.1	The Standard Model of Elementary Particles	2
1.1.1	Quantum Mechanics and Quantum Field Theory	2
1.1.2	Electroweak theory and Quantum Chromo-Dynamics	2
1.1.3	Electroweak symmetry breaking and the Higgs boson	2
1.1.4	Homework from the Standard Model and the beyond	2
1.2	The Super-symmetry Theory	2
1.2.1	Theoretical Framework in a nutshell	2
1.2.2	SUSY breaking	2
1.2.3	Minimal Super-symmetric Standard Model	2
1.2.4	Running masses and GUT	2
1.3	R-parity	2
1.4	Experimental Constraints on SUSY so far	2
1.4.1	Constraint from Observed Standard Model Higgs Mass	2
1.4.2	Constraint from Dark Mater Measurement and Detection experiments	2
1.4.3	Constraint from Indirect Search Experiments	2
1.4.4	Constraint from Direct search at Colliders Experiments	2
1.5	Targeted SUSY Scenario and the Search Strategy in this work	2
1.5.1	Targeted SUSY scenario	2
1.5.2	Topology-based Search and the simplified model	2
1.5.3	Targeted Gluino Signatures	3
1.6	Structure of the thesis	4
1.7	Terminology	4
2	The ATLAS Experiment at the LHC	6
2.1	The Large Hadron Collider	6
2.2	The ATLAS Detector	6
2.2.1	Overview	6
2.2.2	Inner Detectors	6
2.2.3	Calorimetry	6
2.2.4	Muon System	6
2.2.5	Trigger and Data Acquisition System	6
3	Object Reconstruction and Identification	7
3.1	Primary vertices	7
3.2	Tracks	7
3.3	Electron	7
3.3.1	Reconstruction and Identification	7
3.3.2	Calibration	7
3.3.3	Performance	7
3.4	Muon	7
3.4.1	Reconstruction and Identification	7

3.4.2	Calibration	7
3.4.3	Performance	7
3.5	Jet	7
3.5.1	Reconstruction and Identification	7
3.5.2	Calibration	7
3.5.3	Performance	7
3.6	Missing ET	7
3.6.1	Algorithm	7
3.6.2	The Soft Term	7
3.6.3	Performance	7
3.7	Overlap Removal between Reconstructed Objects	7
3.8	Isolation	7
4	Collected Data and Monte Carlo Simulation	8
4.1	Data Sample recorded in ATLAS	8
4.1.1	Luminosity Measurement	8
4.1.2	Qualification	8
4.2	Simulated Samples	8
4.2.1	Generators	8
4.2.2	Detector simulation	9
4.2.3	Design of SUSY Signal Grid for Interpretation	10
5	Event Selection	12
5.1	Trigger	12
5.2	Event Cleaning and the Pre-selection	14
5.3	Signal Region Definition	16
5.3.1	Binning Strategy	16
5.3.2	Discriminating variables	21
5.3.3	Cut Optimization	30
5.3.4	Expected Sensitivity	45
6	Standard Model Background Estimation	48
6.1	Background Breakdown in the Signal Regions	48
6.2	MC vs Data Comparison and the MC mis-modeling	52
6.2.1	$W + \text{jets}$	52
6.2.2	Tops	57
6.3	The Kinematical Extrapolation Method	66
6.3.1	Definition of Control Regions and Validation Regions	66
6.3.2	Result of Background-only Fit	66
6.3.3	Evaluation on the Non-closure	66
6.4	The Object Replacement Method	70
6.4.1	Per-event Procedure	70
6.4.2	Closure Test using $t\bar{t}$ MC Samples	78
6.4.3	Closure test with loose selection.	78

6.4.4	Source of non-closure	85
6.4.5	Closuer test with tigher selection	87
6.4.6	Closure test using data in 1-lepton validation regions.	91
6.5	Multi-jet Validation using Data	93
6.6	Unblinded Validation Regions	96
7	Systematic Uncertainties	97
7.1	Impact on Kinematical Extrapolation Method	97
7.1.1	Instrumental Systematic Uncertainty	97
7.1.2	Theoretical Uncertainty	98
7.1.3	Others	98
7.2	Impact on the Object Replacement Method	99
8	Result	104
8.1	Procedure of Statical Analysis	104
8.2	Unblinded Signal Regions	104
8.3	Observed Constraints on SUSY Models.	104
8.3.1	Constraints on Simplified Models.	104

1 Introduction

1.1 The Standard Model of Elementary Particles

1.1.1 Quantum Mechanics and Quantum Field Theory

1.1.2 Electroweak theory and Quantum Chromo-Dynamics

1.1.3 Electroweak symmetry breaking and the Higgs boson

One outstanding problem in the guidance principle of Gauge symmetry is prohibition of fermion mass terms, where left-handed and right-handed spinor flatly couples therefore violating gauge-invariance. In other words,

Higgs boson (Breit-Englere-Higgs boson) was discovered in LHC in 2012, bringing the last piece of the Standard Model in human knowledge. Measurements on its properties including the mass, spin and couplings follow, and they show all consistent to the SM at the moment. Precision measurement on its couplings is planning in the later stages in LHC.

1.1.4 Homework from the Standard Model and the beyond

Quadratic divergence of Higgs mass and The Naturalness

1.2 The Super-symmetry Theory

1.2.1 Theoretical Framework in a nutshell

1.2.2 SUSY breaking

1.2.3 Minimal Super-symmetric Standard Model

1.2.4 Running masses and GUT

1.3 R-parity

1.4 Experimental Constraints on SUSY so far

1.4.1 Constraint from Observed Standard Model Higgs Mass

1.4.2 Constraint from Dark Mater Measurement and Detection experiments.

1.4.3 Constraint from Indirect Search Experiments

Flavor

Proton Decay

Limit on long-lived gluino from cosmology

1.4.4 Constraint from Direct search at Colliders Experiments

1.5 Targeted SUSY Scenario and the Search Strategy in this work

1.5.1 Targeted SUSY scenario

1.5.2 Topology-based Search and the simplified model

Thgough it sounds impossible to cover and constrain the whole 118 dimensional MSSM parameter space, here the strategy of topology-based search is employed. In this approach, instead of model point in the

parameters space, upper limits are set to individual gluino decay topology assuming 100% decay branch into the final state, therefore the result is model-independent in terms of branch ratio. Considering that most of the MSSM parameters only affect the branchings rather than kinematics, this will

1.5.3 Targeted Gluino Signatures

Gluinos are generated in pair under the assumption of R-parity conservation. The decay is always 3-body through heavy virtual squarks which now we assume are all decoupled, ending up in 2 SM quarks and a EW gaugino. The pattern and branch ratio are highly dependent on properties of EW gauginos such as mass spectra and its mixing.

In LHC, analyses are conventionally divided based on number of hard leptons in the final state . As for gluino decays, under the slepton-free scenario, leptons are always generated via decays of W/Z/H boson. Therefore, giving their small leptonical branching ratio, 0-lepton or 1-lepton final state are the most promising channel for inclusive search, while 2/3-leptons final states are more specialized in specific types of scenarios such as long-chain multi-step gluino decays where more W/Z/H bosons are involved.

This thesis focus on the search using the 1-lepton final state. Although the 0-lepton final state often is more advantageous in terms of coverage of models and signal acceptance, 1-lepton addresses some unique merits over the 0-lepton channel as following:

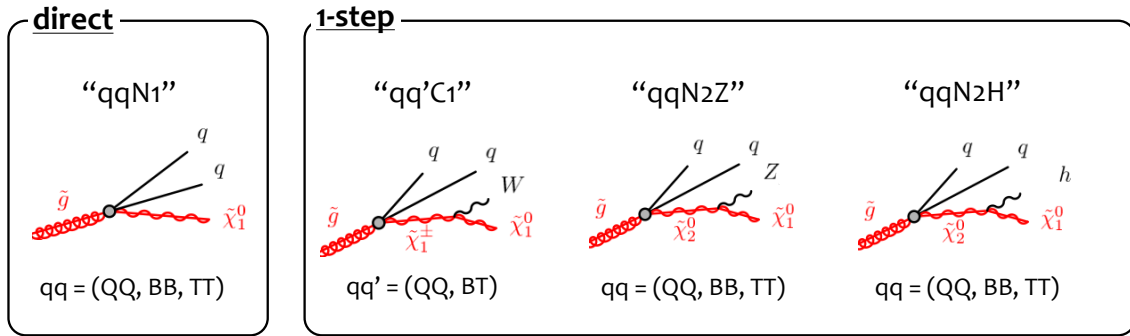


Figure 1:

$$\text{Model name} := aaXXbbYY \quad (1)$$

$$aa, bb = \text{"QQ", "BB", "TT", "BT"} \quad (2)$$

$$XX, YY = \text{"N1", "C1", "N2Z", "N2H"} \quad (3)$$

$$(4)$$

Table 1: Models with events of no b-jets at tree level.

Model name	n_J (tr.)	n_B (tr.)	$\text{Br}(1\text{L})/\text{Br}(0\text{L})$	$\text{Br}(1\text{L})/\text{Br}(2\text{L})$	full sim.?
QQC1QQC1	6	0	0.67	6	✓
QQN1QQC1	4	0	0.33	-	
QQC1QQN2Z	6	0	0.33	-	✓
QQC1QQN2H	6	0-2	0.33	-	✓

Table 2: Models with events of 1 or 2 real b-jets at tree level.

Model name	n_J (tr.)	n_B (tr.)	$\text{Br}(1\text{L})/\text{Br}(0\text{L})$	$\text{Br}(1\text{L})/\text{Br}(2\text{L})$	full sim.?
QQC1BTC1	8	2	1	2	
QQN1TTN1	6	2	0.67	6	
QQN1BTC1	6	2	0.67	6	
QQN1TTN2Z	8	2	0.67	6	
QQC1BBN2Z	6	2	0.33	-	
QQC1BBN2H	6	2-4	0.33	-	
QQC1TTN2Z	10	2	1	2	
QQC1TTN2H	10	2-4	1	2	
QQN2ZTTN2Z	10	2	0.67	6	
QQN2ZTTN2H	10	2-4	0.67	6	
BBN1QQC1	4	2	0.33	-	
BTC1QQN2Z	8	2	0.67	6	
BTC1QQN2H	8	2-4	0.67	6	
TTN1QQC1	8	2	1	2	
TTN1QQN2Z	8	2	0.67	6	
TTN2ZQQN2H	10	2-4	0.67	6	

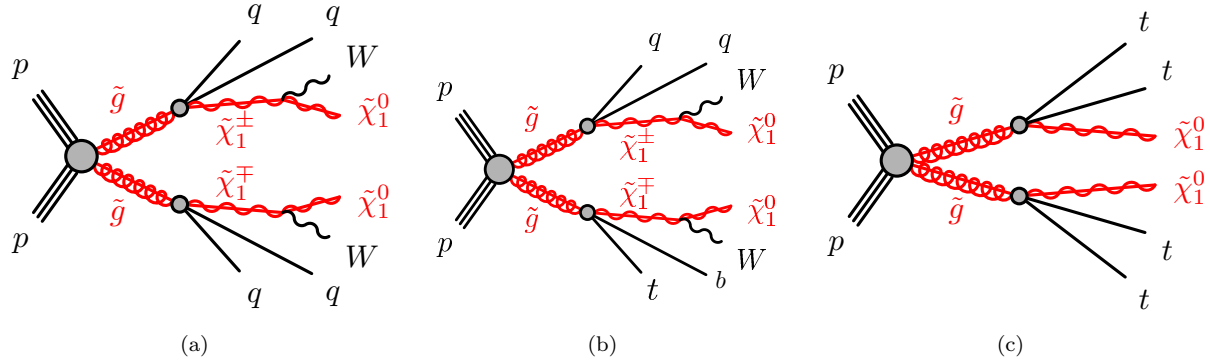


Figure 2: Feynmann diagrams for the Benchmark models (a) QQC1QQC1 (b) QQC1BTC1 (c) TTN1TTN1.

1.6 Structure of the thesis

1.7 Terminology

Table 3: Models with events of 3 or more real b-jets at tree level.

Model name	n_J (tr.)	n_B (tr.)	$\text{Br}(1\text{L})/\text{Br}(0\text{L})$	$\text{Br}(1\text{L})/\text{Br}(2\text{L})$	full sim.?
QQN1TTN2H	8	4	0.67	6	
BBN1TTN1	6	4	0.67	6	
BBN1BTC1	6	4	0.67	6	
BBN1TTN2Z	8	4	0.67	6	
BBN1TTN2H	8	6	0.67	6	
BTC1BTC1	10	4	1.33	1.33	
BTC1BBN2Z	10	4	0.67	6	
BTC1BBN2H	10	6	0.67	6	
BTC1TTN2Z	12	4	1.33	1.33	
BTC1TTN2H	12	6	1.33	1.33	
TTN1TTN1	10	4	1.33	1.33	✓
TTN1QQN2H	8	4	0.67	6	
TTN1BTC1	10	4	1	2	
TTN1BBN2Z	8	4	0.67	6	
TTN1BBN2H	8	6	0.67	6	
TTN1TTN2Z	12	4	1.33	1.33	
TTN1TTN2H	12	6	1.33	1.33	
BBN2ZTTN2Z	10	4	0.67	6	
BBN2ZTTN2H	10	6	0.67	6	
TTN2ZTTN2Z	14	4	1.33	1.33	
TTN2ZBBN2H	10	6	0.67	6	
TTN2ZTTN2H	14	6	1.33	1.33	
QQN2HTTN2H	10	6	0.67	6	
BBN2HTTN2H	10	8-12	0.67	6	
TTN2HTTN2H	14	8-12	1.33	1.33	

2 The ATLAS Experiment at the LHC

2.1 The Large Hadron Collider

2.2 The ATLAS Detector

2.2.1 Overview

Multi-purpose detector integrated with 1) Inner detectors (ID) 2) Caloremeters 3) 4) 5) from the inner to outer.

2.2.2 Inner Detectors

2.2.3 Calorimetery

2.2.4 Muon System

2.2.5 Trigger and Data Acquisition System

3 Object Reconstruction and Identification

3.1 Primary vertices

The position of interaction points of proton-proton collisions is important for all objects as it defines the pointing direction of reconstructed particles and provide critical information for pileup rejection. These are

In order to distinguish against secondary vertices generated by the late decaying particles, these are referred as “primary vertices”.

3.2 Tracks

Charged tracks are also fundamental units that are used almost in all the higher level particle reconstruction. These are firstly seeded by the

3.3 Electron

3.3.1 Reconstruction and Identification

Electrons are reconstructed by Sliding window algorithms

3.3.2 Calibration

3.3.3 Performance

3.4 Muon

3.4.1 Reconstruction and Identification

3.4.2 Calibration

3.4.3 Performance

3.5 Jet

3.5.1 Reconstruction and Identification

Jet reconstruction starts from forming sub-clusters based on the energy deposits in the calorimeter

Re In the LHC-Run2 enjoys 20-40 collisions per bunch crossing

Electrons and hadronically decaying taus (charged / neutral pions) are also clustered as jets and pass the JVT requirement. While a tau jet is consequently labeled as a jet in the analysis as the it is tau-agonistic, electrons experience the “overlap removal” procedure described in the following sub-section, to prevent the double-counting.

3.5.2 Calibration

3.5.3 Performance

3.6 Missing ET

3.6.1 Algorithm

3.6.2 The Soft Term

3.6.3 Performance

3.7 Overlap Removal between Reconstructed Objects

3.8 Isolation

4 Collected Data and Monte Carlo Simulation

4.1 Data Sample recorded in ATLAS

The protonproton data analysed in this paper were collected by ATLAS during 2015 and 2016 at a centre-of-mass energy of 13 TeV with up to 50 simultaneous interactions per proton bunch crossing. After application of data-quality requirements related to the beam and detector conditions, the total integrated luminosity corresponds to 36.1 fb⁻¹. The uncertainty on the combined 2015 and 2016 integrated luminosity is $\pm 3.2\%$.

4.1.1 Luminosity Measurement

Calibration of luminosity scale are done by the Val der Meer scan [?].

4.1.2 Qualification

4.2 Simulated Samples

MC simulation is a highly powerful toolkit that are used extensively from studying signal/background separation, estimating background and calculating final observed limit and so on. In this sub-section, the setup of simulated samples used in the analysis is described. For SUSY signal samples, the scheme of choosing mass points are also illustrated.

4.2.1 Generators

V + jets The W/Z+jets events are normalised to their NNLO cross-sections [?]. The diboson samples [?] are generated using the Sherpa 2.1.1 and 2.2.1 generators with the same PDF setup as the W/Z+jets samples described above. The fully leptonic diboson processes are simulated including final states with four charged leptons, three charged leptons and one neutrino, two charged leptons and two neutrinos, and one charged lepton and three neutrinos.

The semi-leptonic diboson processes are simulated with one of the bosons decaying hadronically and the other leptonically. The processes are calculated for up to one parton (for ZZ) or no additional partons (for WW, WZ) at NLO and up to three partons at LO. Each of the diboson processes is normalised to the corresponding NLO cross-section [?].

t \bar{t} and sinlep-top To generate t \bar{t} and single top quark events in the Wt and s-channel, the powheg-box v2 [?] generator with the CT10 [?] PDF sets in the matrix-element calculations is used.

Electroweak t-channel single-top-quark events are generated using the powheg-box v1 generator. This generator uses the four-flavor scheme for the NLO matrix-element calculations together with the fixed four-flavor PDF set CT10f4.

For all top-quark processes, top-quark spin correlations are preserved (for the single-top t-channel, top quarks are decayed using MadSpin [?]).

The parton shower, fragmentation, and the underlying event are simulated using Pythia 6.428 [?] with the CTEQ6L1 [?] PDF set and the corresponding Perugia2012 tune (P2012) [?].

The top-quark mass is set to 172.5 GeV. The EvtGen v1.2.0 program is also used to describe the properties of the bottom and charm hadron decays in the t \bar{t} and the single-top-quark samples.

The `hdamp` parameter, which controls the pT of the first additional emission beyond the Born configuration, is set to the mass of the top-quark. The main effect of this is to regulate the high pT emission against which the $t\bar{t}$ system recoils.

The $t\bar{t}$ events are normalised to the cross-sections computed at next-to-next-to-leading order (NNLO) with next-to-next-to-leading-logarithmic (NNLL) corrections [?].

The single-top quark events are normalised to the NLO+NNLL cross-sections for the Wt-channel [?] and to the NLO cross-sections for the t- and s-channels [?].

Events containing W or Z bosons with associated jets (W/Z+jets) [?] are simulated using the Sherpa 2.2.1 generator [?] Matrix elements are calculated for up to two partons at NLO and four partons at LO using the Comix [?] and OpenLoops [?] generators. They are merged with the Sherpa 2.2.1 parton shower [?] with massive b and c quarks using the ME+PS@NLO prescription [?]. The NNPDF3.0 NNLO PDF set [?] is used in conjunction with a dedicated parton-shower tuning developed by the Sherpa authors.

$t\bar{t} + W/Z/h/WW$ For the $t\bar{t} + W/Z/WW$ processes [?], all events are simulated using MG5_aMC NLO 2.2.2 at LO interfaced to the Pythia 8.186 parton shower model, with up to two ($t\bar{t} + W$), one ($t\bar{t} + Z$) or no ($t\bar{t} + WW$) extra partons included in the matrix element. The EvtGen v1.2.0 program [?] is used to describe the properties of the bottom and charm hadron decays. The ATLAS shower and underlying-event tune A14 is used together with the NNPDF2.3 LO PDF set. The events are normalised to their NLO cross-sections [?, ?].

SUSY signals The signal samples are generated at leading order (LO) using MG5_aMC NLO 2.2.2 [?] with up to two extra partons in the matrix element, interfaced to Pythia 8.186 [?] for parton showers and hadronisation. The CKKW-L matching scheme [?] is applied for the matching of the matrix element and the parton shower, with a scale parameter set to a quarter of the mass of the sparticle produced. The ATLAS A14 [?] set of tuned parameters (tune) is used for the shower and the underlying event, together with the NNPDF2.3 LO [?] parton distribution function (PDF) set.

The EvtGen v1.2.0 program [?] is used to describe the properties of the bottom and charm hadron decays in the signal samples.

The signal cross-sections are calculated at next-to-leading order (NLO) in the strong coupling constant, adding the resummation of soft gluon emission at next-to-leading-logarithmic accuracy (NLL) [?].

The nominal cross-section and its uncertainty are taken from an envelope of cross-section predictions using different PDF sets and factorisation and renormalisation scales, as described in Ref. [?], considering only the four light-flavor left-handed squarks (u_L , d_L , s_L , and c_L).

The simulated event samples for the signal and SM backgrounds are summarised in Table 1. Additional samples are used to assess systematic uncertainties, as explained in Section 6.

Benchmark SUSY signals The summary of generator, hadronization schemea and tuning is shown in Tab.1.

4.2.2 Detector simulation

The response of the detector to particles is modelled either with a full ATLAS detector simulation [?] using Geant4 [?] or with a fast simulation [?]. The fast simulation is based on a parameterisation of the performance of the electromagnetic and hadronic calorimeters and on Geant4 elsewhere. All background (signal) samples are prepared using the full (fast) detector simulation. All simulated events are generated with

a varying number of minimum-bias interactions overlaid on the hard-scattering event to model the multiple proton-proton interactions in the same and the nearby bunch crossings. The minimum-bias interactions are simulated with the soft QCD processes of Pythia 8.186 using the A2 tune [?] and the MSTW2008LO PDF set [?]. Corrections are applied to the samples to account for differences between data and simulation for trigger, identification and reconstruction efficiencies.

4.2.3 Design of SUSY Signal Grid for Interpretation

To derive the upperlimit as a continuous function of masses, or to announce the mass reach of exclusion, signal samples are generated with masses in discrete steps so that the results can be interpolated eventually. For example, in case of models with direct gluino decays, parameter space is spanned by two masses $m_{\tilde{g}}$ and $m_{\tilde{\chi}_1^0}$, therefore the samples are generated by a 2D-grid. Fig. 1 is the example of the TTN1TTN1 grid where 112 points are generated in total.

There are three relevant masses in case of 1-step gluino decay: $m_{\tilde{g}}$, $m_{\tilde{\chi}_1^\pm/\tilde{\chi}_2^0}$ and $m_{\tilde{\chi}_1^0}$. As the 3D-grid is by far computational expensive compared with the 2D one, a realistic approach is to choose out a couple of sensible 2D-slices with losing minimum generality.

Note that the relative mass splitting parameter is defined as:

$$x := \Delta m(\tilde{\chi}_1^\pm/\tilde{\chi}_2^0, \tilde{\chi}_1^0) / \Delta m(\tilde{g}, \tilde{\chi}_1^0),$$

ranging from 0 to 1.

In addition to them, the regime of small- x and non-massless LSP is attractive in context of dark matter. Therefore in some of the models particularly when $\Delta m(\tilde{\chi}_1^\pm/\tilde{\chi}_2^0, \tilde{\chi}_1^0) = 20 \sim 30 \text{ GeV}$.

A dedicated tower **Low-x** then is designed specifically for this scenario where hard jets ($p_T > 80 \text{ GeV}$) and one soft lepton is required. Although the phase space is overlapped with tower **2J**, it addresses unique sensitivity in the $\Delta m(\tilde{\chi}_1^\pm, \tilde{\chi}_1^0)$ $n = 20, 30 \text{ GeV}$ grid.

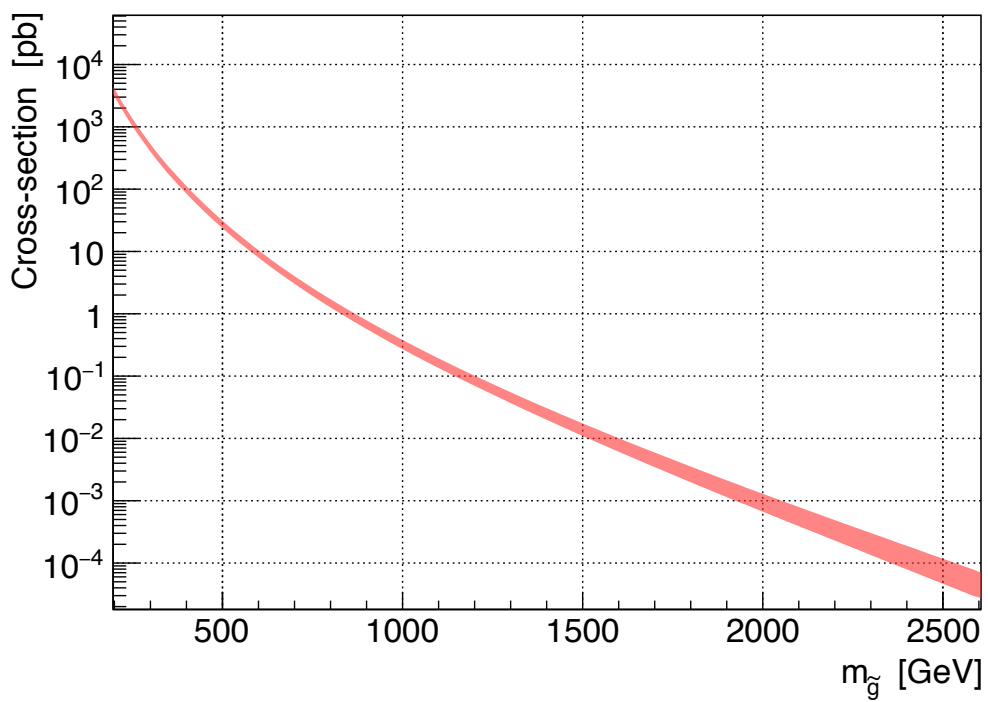


Figure 3:

5 Event Selection

5.1 Trigger

Taking the advantage that most of the signal models we consider result in large missing ET (MET) due to the LSPs, the lowest unprescaled MET trigger HLT_xe110_mth_XE50 is used for triggering events throughout the analysis. Thanks to the fact that MET is calculated from global information of an event rather than the feature of a single particular particle, the plateau efficiency amounts almost 100 %. This is a significant advantage over the use of leptonic trigger where efficiency is typically 70% \sim 90%. Meanwhile, the potential downside of MET trigger is its slow turn-on in terms of the off-line MET that needs nearly 200GeV to assure the plateau efficiency despite much lower trigger threshold (50GeV for L1 and 110GeV for HLT). This is due to the deteriorated resolution of on-line MET which is purely based on calorimeter clusters, with respect to the off-line one which is take into muons and soft tracks into account.

The turn-on also has dependency on event topology and kinematics due to varying MET resolution in particular sensitive to magnitude of jet activity, however this does not affect the plateau efficiency. Fig. 4 shows turn-ons with different jet multiplicity and $\min_{i=1-4} \Delta\phi(j_i, E_T^{\text{miss}})$.

All in all, the efficiency safely reaches the plateau after 200GeV in off-line MET. Therefore here it is promised to always require $E_T^{\text{miss}} > 200\text{GeV}$ as well as the online trigger bit in case of trigger requirement. The signal acceptance by the trigger requirement is $> 95\%$ except when gluino mass and LSP mass are compressed. Nevertheless, given that it is impossible for such signal to be discriminated against background without the MET generated by associated ISRs, the loss in trigger is not problematic.

The single-lepton trigger (SLT) is also used for supplemental purpose including the efficacy measurement of MET trigger and closure tests of data-driven background estimation. The trigger turn-on is about 28GeV (26GeV) for single-electron (muon) in its transverse momentum and 30GeV (28GeV) is required as off-line threshold.

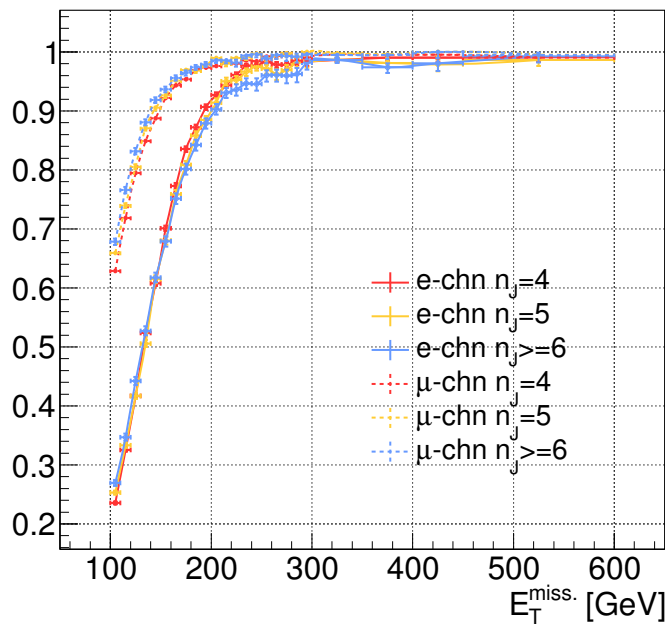


Figure 4: Efficiency curve of MET trigger measured with data by tagging a lepton with $p_T(\ell_1) > 35\text{GeV}$ firing the single-lepton trigger.

5.2 Event Cleaning and the Pre-selection

Event cleaning is applied to get rid of funky data events that are either in bad quality due to inappropriate detector status and badly measured objects, or with objects stemming from somewhere other than the hard collision such as cosmic muons and beam-induced background. As those events could result in extraordinary observables, for instance extremely high jet pt or MET, they are generally critical for search analyses probing the high-end of kinematics where only a few background events in signal regions are in discussion where therefore even a single event of the accidental contamination makes huge impact on the final result. The list of procedure and cut efficiencies are summarized in Tab. 4.

Table 4: List of cuts applied as event cleaning. Data and MC shows different efficiencies up-to the top four since MC does not emulates bad data quality and cosmic muons in it.

Cut	Efficiency (Data) [%]	Efficiency (MC, $t\bar{t}$) [%]
Veto bad lumi-clocks	95.12	100.0
Veto bad DAQ events	99.81	100.0
Veto events with no primary vertex	100.0	100.0
Veto events with cosmic muons	95.83	98.52
Veto events with badly measured jets	99.49	99.65
Veto events with badly measured muons	99.99	98.56

Lumi-blocks with more than 10% of the detector in the bad status are firstly removed. Events affected by noise bursts in LAr and SCT, corrupted data transmission in LAr and the Tile calorimeter are then vetoed subsequently.

Cosmic muon are vetoed by requiring the muon track passing reasonably close-by the primary vertex i.e.

$$|z_0| < 1 \text{ mm}, \quad d_0 < 0.2 \text{ mm}.$$

The beam induced backgrounds are events with muons that are generated by the secondary cascades of protons traveling upstream of the interaction point. The energy depositions created by these muons can be reconstructed as jets with energy as high as the beam energy therefore becomes highly signal-like. To reject the fake jets, event with jets flagged as “BadLoose” described in [?] are vetoed.

Badly measured high energy muons are also the source of fake high MET ranging upto a few TeV. Bad muons are defined as the muons passing either of the criteria:

- $\sigma(q/p)/(q/p) > 0.2$
- ... (to be added later)

and the entire events containing at least one bad muon are similarly vetoed.

Fig. 5 demonstrate the performance of bad muon veto. While bad muon events typically peak in $\Delta\phi(l, E_T^{\text{miss}})$ since the fake MET aligns with the muon, it is exclusively resolved by the veto. Also, the role of bad muon veto is shown to be very important in this analysis as the 1-muon high MET phase space generally suffers from severe contaminaton by bad muon events upto about 20% (90%) with $E_T^{\text{miss}} > 1(2)\text{TeV}$.

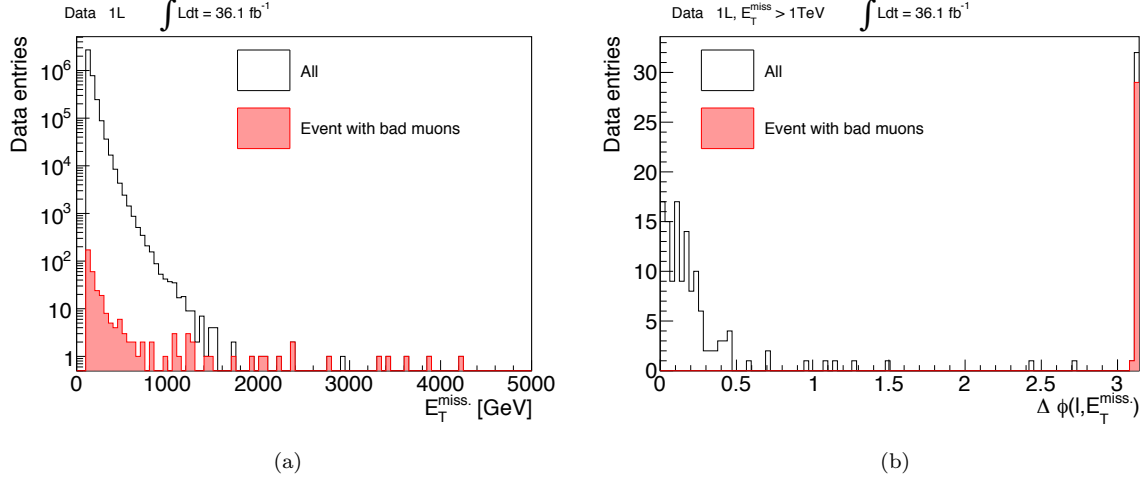


Figure 5: (a) MET distribution after requiring exactly one signal muon and MET trigger, and (b) $\Delta\phi(l, E_T^{\text{miss}})$ distribution with $E_T^{\text{miss}} > 1\text{TeV}$ being applied. The pink histogram corresponds to events dropped by the bad muon veto. The veto looks working reasonably considering the apparent spike due to the fake MET: $\Delta\phi \sim \pi$ is cleared.

The pre-selection is the common selection applied in the analysis. The 1-lepton pre-selection is defined as Tab. 1.

Table 5: List of requirements for the 1-lepton pre-selection.

Event cleaning
Pass the MET trigger and $E_T^{\text{miss}} > 250\text{GeV}$
At least one signal electron (muon) with $p_T > 7(6)\text{GeV}$.
At least two jets with $p_T > 30\text{GeV}$.

5.3 Signal Region Definition

5.3.1 Binning Strategy

To inclusively address to all the 45 decay models and all possible mass spectra, a set of tailored multi-bin signal regions (SRs) are employed. Specifically, different decay models are covered by splitting the signal regions in terms of b-jet multiplicity (“categories”), and various mass spectra are dealt by splitting in terms of kinematics (“towers”). SR bins are basically designed to be exclusive for each other, aiming at an easy combination afterward so that no signals are lost due to the binning.

The definition of the b-jet based categories: b-vetoed (BV), b-tagged (BT) and 3B follows Tab. 6, respectively targeting the models in Tab. 1, 2 and 3 in Sec. 1.5.3. The b-jet multiplicity for the benchmark signals versus background at the pre-selection level is shown in Fig. 6. Note that despite a fraction of signal events falling into other categories than the benchmarked one, they will not be wasted thanks to the combined fit performed in deriving the final result. As the S/N ratio and the background kinematics in BV/BT are found to be more or less similar, further kinematical selections in those categories are set to identical for simplicity. On the other hand, different selection strategy is adopted for the 3B categories since the background level is significantly lower and also the composition is very different.

Table 6: The definition of the b-jet based categories and the main backgrounds there.

Category	b-jet multiplicity	Main background
B-vetoed (BV)	0	$W + \text{jets}$
B-tagged (BT)	1-2	$t\bar{t}$
3B	≥ 3	$t\bar{t}, t\bar{t} + cc/bb$

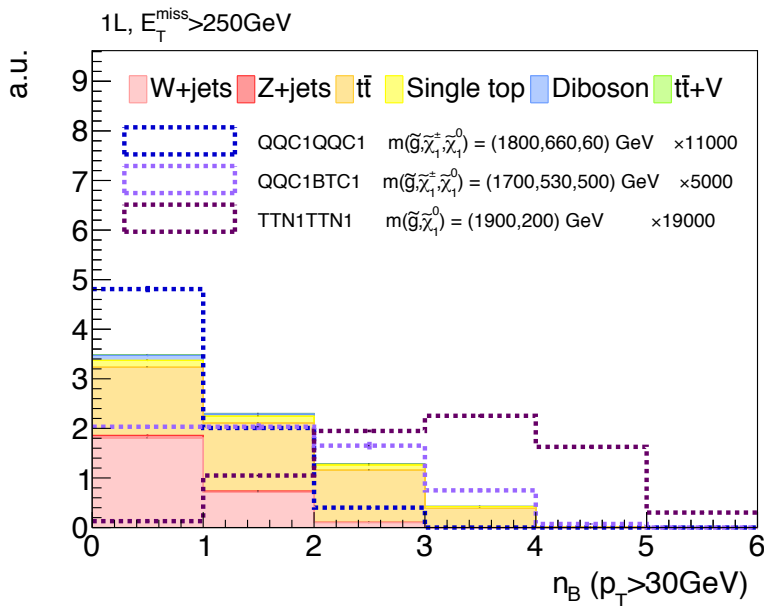


Figure 6: B-tagged jet multiplicity for standard model backgrounds and the benchmark signals (QQC1QQC1 for BV, QQC1BTC1 for BT and TTN1TTN1 for 3B categories respectively) after the 1-lepton pre-selection.

The BV/BT categories are further divided into 4 SR “towers” accommodate the 4 different mass configurations in terms of the relative mass splitting between the gluino, intermediate EW gaugino and the LSP in the 1-step decays. Fig. 7 illustrates the mass configurations and the associated SR towers in case of the benchmark model “QQC1QQC1” as example, each of which is further detailed as below.

1. The mass of intermediate EW gaugino is roughly in the middle of those of gluino and the LSP ($x \sim 1/2$). This is the most standard configuration where particles from both gluino and the intermediate EW gaugino decays are hard enough to pass the criteria of hard lepton ($> 35\text{GeV}$) and jets ($p_T > 30\text{GeV}$). As the signals targeted by the BV/BT categories typically result in 4–10 jets at the tree-level, a tower **6J** with $n_J \geq 6$ is defined.
2. Gluino and EW gauginos are all compressed. From either trigger and background separation point of view, hard ISRs are inexpensive for probing this type of signatures so that the $\tilde{g}\tilde{g}$ system gets kicked and resulting in large MET. On the other hand, as the kicked gluinos are typically enough heavy to be non-relativistic, the transverse momentum of the boosted $\tilde{g}\tilde{g}$ system is almost solely converted into MET. As a result the particles from gluino decays stay soft, thus a tower **2J** consisting of a soft lepton, at least two hard jets and large MET is defined for targeting the signature.
- 3.,4. The intermediate EW gaugino and either gluino or LSP are compressed ($x \sim 0, 1$). There is also an extreme case where the intermediate EW gaugino mass is put close by the gluino or LSP, and the signal region towers: *High-x* and *Low-x* are employed to cover the scenario.

Similar discussion holds for direct gluino decay models as well i.e. the tower **2J** covers the scenario of compressed mass spectra while the tower **6J** is used for general cases.

In contrast to the BV/BT category, the 3B does not undergo the additional classification in towers since the targeted signal models usually involve top quarks that can result in hard jets, leptons and MET. Therefore the kinematics does not dramatically vary between the mass configurations unless the top-quarks are on-shell. The only exception is when gluino and the intermediate EW gaugino get compressed, and the top-quarks turn to off-shell ending up in soft decay particles. However such events are then covered by the BT towers instead, thanks to the dropped ≥ 3 b-jet acceptance according to the decreasing b-quarks’ p_T .

To summarize, 5 towers out of 3 categories are defined as Tab. 7, and the coverage in sensitivity by each signal region tower on the mass grid of the signal models are shown in Fig. 8.

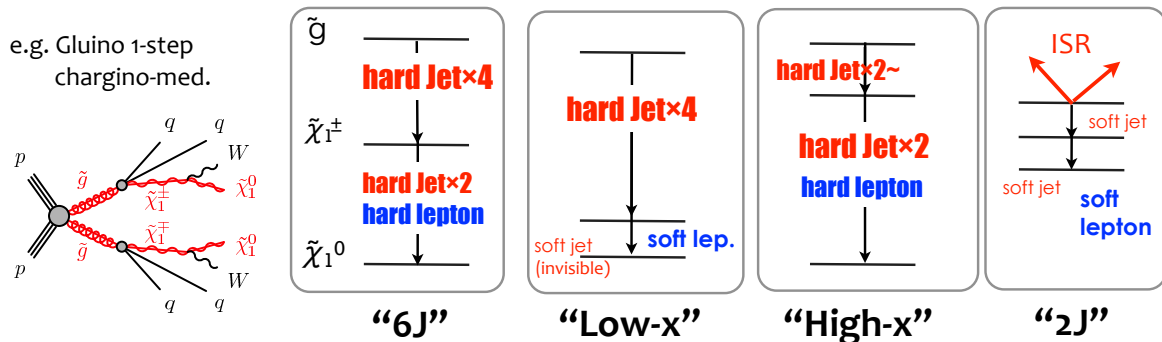


Figure 7: BT/BV towers and their targeted mass configuration.

Table 7: List of defined towers in each b-category and t kinamtical selection required. **2J** and **6J**, **Low-x** and **High-x** are orthogonal to each other. **3B** are orthogonal to all the other towers.

Category	Tower	Electron (muon) p_T [GeV]	$n_J (p_T > 30\text{GeV})$
BV/BT	2J	$\in [7(6), 35]$	≥ 2
	6J	> 35	≥ 6
	Low-x	$\in [7(6), 35]$	≥ 5
	High-x	> 35	≥ 4
3B	3B	> 15	≥ 7

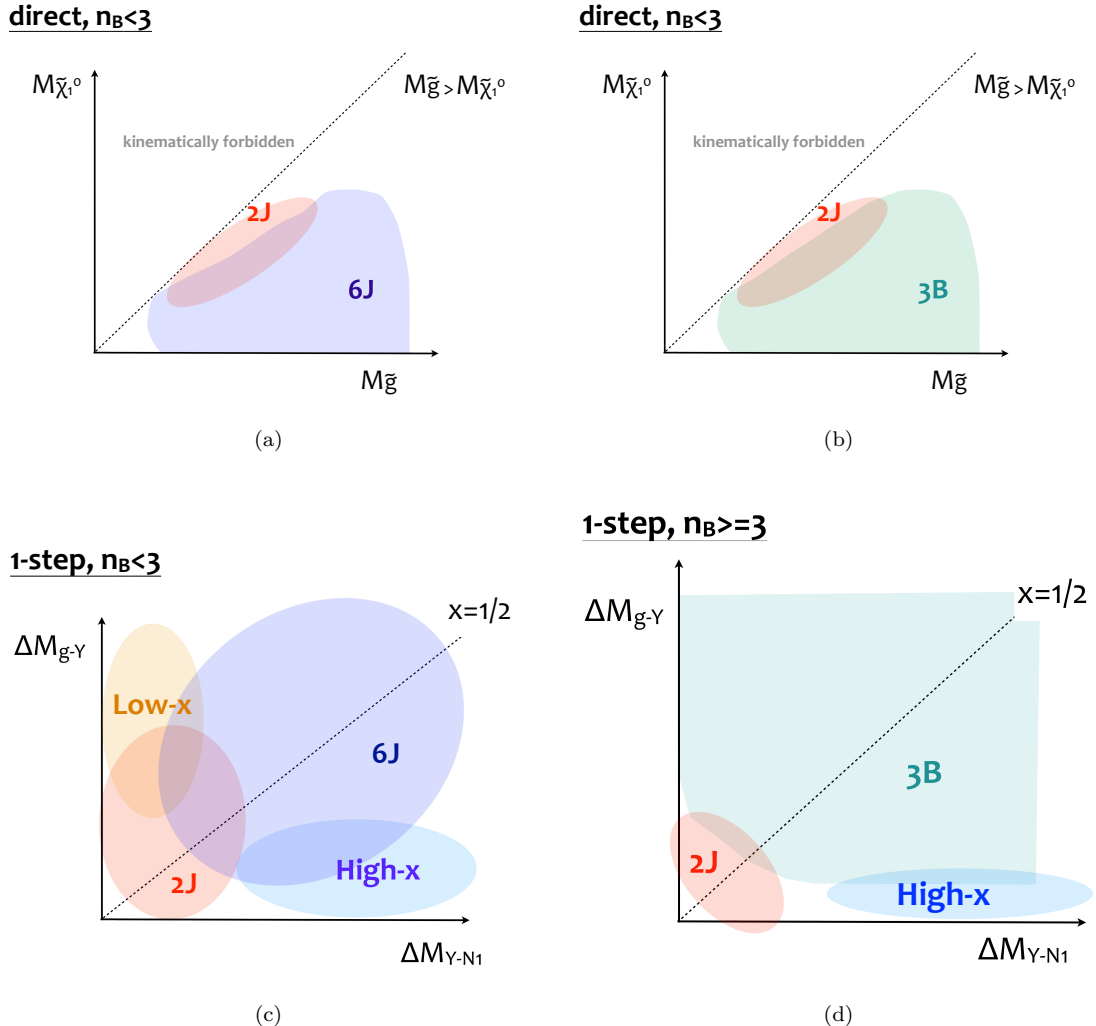


Figure 8: Sensitivity coverage by each tower in the mass grids for different types of decay models. n_B denotes the number of b-quarks in the final state at tree-level as defined in Sec. 1.5.3. M_Y is the mass of intermediate EW gaugino.

Finally, the towers further experience the binning in terms of $m_{\text{eff}} := E_T^{\text{miss}} + \sum_i p_T(j_i)$ to accommodate different absolute scale of mass splitting. The “2J/6J” and “3B” tower are segmented into 3 and 2 bins respectively while “Low-x” and “High-x” are single-binned as their low m_{eff} bins have too much overlap with “2J” and “6J” in phase space which does not provide unique sensitivity. The bin widths of m_{eff} are set to be 400GeV – 500GeV driven by the width of m_{eff} distribution for signals that the lower m_{eff} bins typically target ($\Delta m(\tilde{g}, \tilde{\chi}_1^0) = 1\text{TeV} \sim 1.5\text{TeV}$). The “3B” tower enjoys an exceptionally wider bin width with 750GeV, compromising with limited statistics in corresponding control regions.

To conclude, the signal regions end up in 5 tower-structured bins as schematized as Fig. 1, where 3×2 bins in $m_{\text{eff}} \times (\text{BV}/\text{BT})$ reside in the tower ”**2J**” and ”**6J**”, 1×2 bins in ”**Low-x**” and ”**High-x**”, and 2 m_{eff} bins in ”**3B**”. Since all the SRs bins in the towers ”2J/6J/3B” or ”Low-x/High-x/3B” are statistically independent, they can be straightforwardly combined in a simultaneous fit.

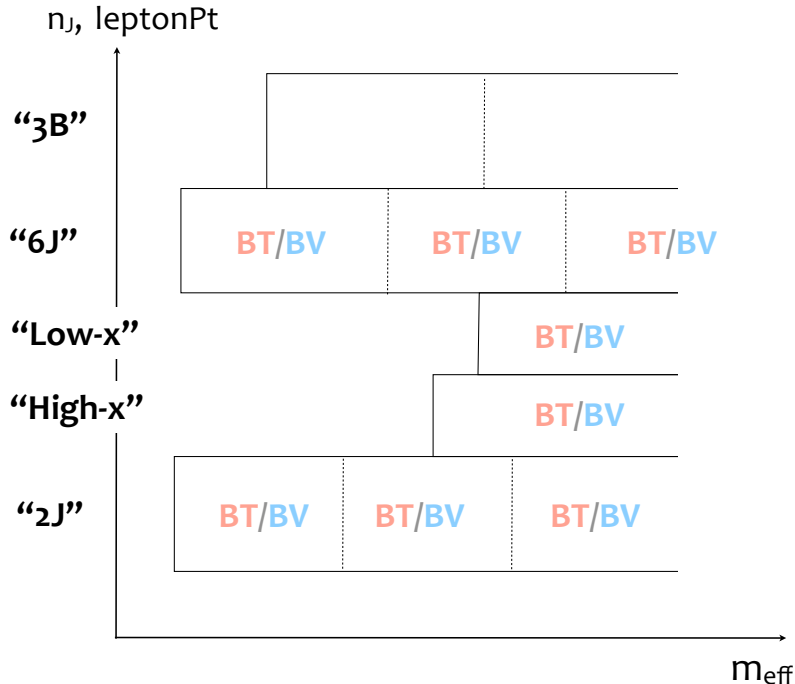


Figure 9: Tower structure and the m_{eff} binning of signal regions.

5.3.2 Discriminating variables

Kinamtical variables used for background rejection as well as defining control regions are overviewed. The distrubtions of signal overlayed with backgrounds at the preselection region are presented in Fig. ??, Fig. ?? and Fig. ??, where $m_{\text{eff}} > 1500\text{GeV}$ and $n_B(p_T > 30\text{GeV}) \geq 3$, $m_T > 125\text{GeV}$ are additionally applied for Fig. ?? and Fig. ?? respectively.

n_J Jet multiplicity often shows the great discriminating power since the standard model processes suffer a sharpe cut-off, however one should mind that the optimum cut is significantly dependent on the gluino decay mode, and also that the aggressive cut will enhance the contribution from higher order effect, putting the modeling at the risk of large theoretical uncertainty. Therefore, it is kept to a moderated use as means of background rejection.

E_T^{miss} Signal events typically has large E_T^{miss} reflecting the presence of hard additional undetected LSP, including when $\text{dm}(g, N1)$ is compressed where MET via ISRs is nevertheless required for the trigger sake, and also the case with small- x where the intermediately EW gauginos gets boosted.

m_{eff} m_{eff} is the variable best reflecting the magnitude of absolute mass splitting $\Delta m(\tilde{g}, \tilde{\chi}_1^0)$, providing the best separation against backgrounds. Meanwhile it is also noticeable that the magnitude of m_{eff} is almost uniquely determined by $\Delta m(\tilde{g}, \tilde{\chi}_1^0)$, regardless of the relative mass splitting and gluino decays, therefore the optimal cut in m_{eff} is highly universal.

$m_T(\mathbf{p}_T(\ell), E_T^{\text{miss}})$ Invariant mass of E_T^{miss} and the lepton with the z-momentum set to 0. Analogous to ordinary invariant mass peaking at the mass of the parent particle, the end point of m_T represents the parent mass when they share the same origin. Since SM 1-lepton process is always with a leptonically decaying W-boson without additional hard missing particles, the bulk component experiences a sharpe cut-off in m_T around $m_W = 81.4\text{GeV}$, therefore the cut above m_W is tremendously effective.

$E_T^{\text{miss}}/m_{\text{eff}}$ A variables to separate backgrounds from signals that are targeted by 2J and High-x where jet activity is relatively low with respect to the magnitude of MET required.

Aplanarity A variable characterizing the 3-dimensionality of an event in terms of the final state particles, defined as the thertial eigenvalue of the normalised jet momentum tensor:

$$S^{\alpha\beta} := \frac{\sum_i p_i^\alpha p_i^\beta}{\sum_i |\mathbf{p}_i|^2}, \quad (5)$$

$$P^{-1}SP = \begin{pmatrix} \lambda_1 & & \\ & \lambda_2 & \\ & & \lambda_3 \end{pmatrix}, \quad \lambda_1 > \lambda_2 > \lambda_3. \quad (6)$$

$$\text{Aplanarity} := \frac{3}{2} \times \lambda_3. \quad (7)$$

Aplanarity ranges from $0 < A < 1/2$. Events with jets distributed in the common plain lead to $A = 0$ and $A = 0.5$ corresponds to an isotropically distributed event shape.

$\mathbf{n}_J/\mathbf{p}_T(\ell_1)$ (... to be added)

$\min_{i=1-4} \Delta\phi(j_i, E_T^{\text{miss}})$ A variable intended to reject $t\bar{t}$ events with the system kicked by ISRs/FSRs.

Topness One of the most important background in 1-lepton analysis is di-leptonic $t\bar{t}$ events with a hadronically decaying tau lepton or a lepton that fails the baseline requirement. To reject those events, a χ^2 -based di-leptonic $t\bar{t}$ tagger “topness” has been designed in context of scalar-top search since Run1 [1]. The χ^2 function is defined as:

$$\begin{aligned} S(p_W^x, p_W^y, p_W^z, p_\nu^z) \\ = \chi^2(m_{t,1}^2) + \chi^2(m_{t,2}^2) + \chi^2(m_{W,1}^2) + \chi^2(\hat{s}(t\bar{t})) \\ + \frac{(m_t^2 - (p_{b,1} + p_\ell + p_\nu)^2)^2}{a_t^4} \\ = \frac{(m_t^2 - (p_{b,2} + p_W)^2)^2}{a_t^4} \\ + \frac{(m_W^2 - (p_\ell + p_\nu)^2)^2}{a_W^4} \\ + \frac{(4m_t^2 - (p_\ell + p_\nu + p_{b,1} + p_{b,2} + p_W)^2)^2}{a_{t\bar{t}}^4}, \end{aligned} \quad (8)$$

assuming an event topology as shown Fig. 1 where one of the lepton are totally undetected and the momentum does fully contribute to MET.

It consists of four gaussian constraints imposing the mass constraint of top-quark and W-boson, and the center-of-mass for the $t\bar{t}$ system being close to its minimum threshold ($2m_t$). The width parameters are set to $(a_t, a_W, a_{t\bar{t}}) = (15, 5, 1000)\text{GeV}$, accounting for the Breit-Wigner widths of top-quark and W-boson as well as the tail of $\hat{s}(t\bar{t})$ distribution. Although there are three missing particles in the topology, the number of unknown degree of freedom can be reduced into 4 by combining the missing lepton (ℓ_2) and the paired neutrino (ν') into a single onshell W-boson and imposing the vectoral sum of transverse momenta of missing particles being equal to E_T^{miss} . Topness is then defined as the minimum χ^2 when scanning over the four DOFs parametrized by p_W and p_ν^z :

$$\text{Topness} := \min_{p_W^x, p_W^y, p_W^z, p_\nu^z} \ln[S]. \quad (9)$$

Events in the topology assumed are supposed to have solutions $(p_W^x, p_W^y, p_W^z, p_\nu^z)$ that satisfy the four constraints at the same time while scanning, however it is not necessarily the case for the other type of events. Fig. 10 shows typical separation between di-leptonic $t\bar{t}$ and signals. Although di-leptonic $t\bar{t}$ does have a fraction of unfortunate events on the pile of higher values due to the fact that the energy of missing leptons or tau leptons does not entirely contribute to MET, the majority resides on the left pile while signals typically populate more in the opposite one. The biggest bottleneck is however, the discrimination power gets drastically worse when one of the b-jets are untagged, since it suffers from the ambiguity in associating the b-quarks and the light flavor jets in the events. Therefore this variable is used only for the “3B” category in this analysis.

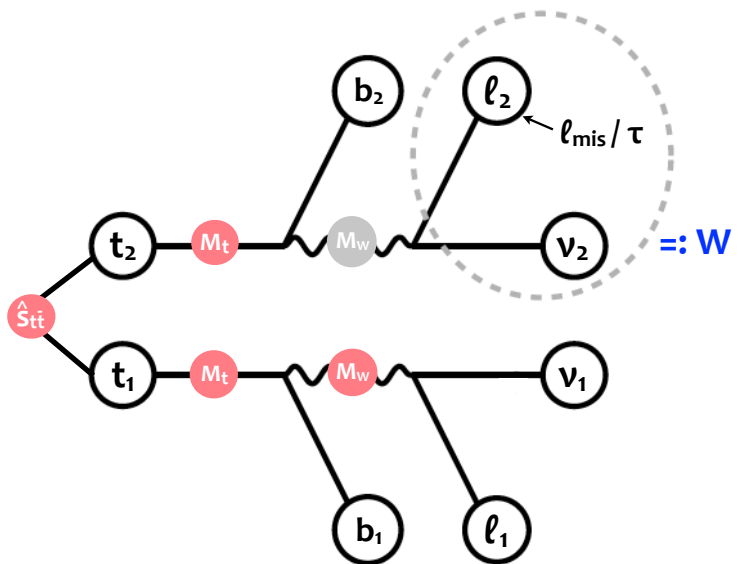


Figure 10: Di-leptonic $t\bar{t}$ topology assumed in the topness calculation.

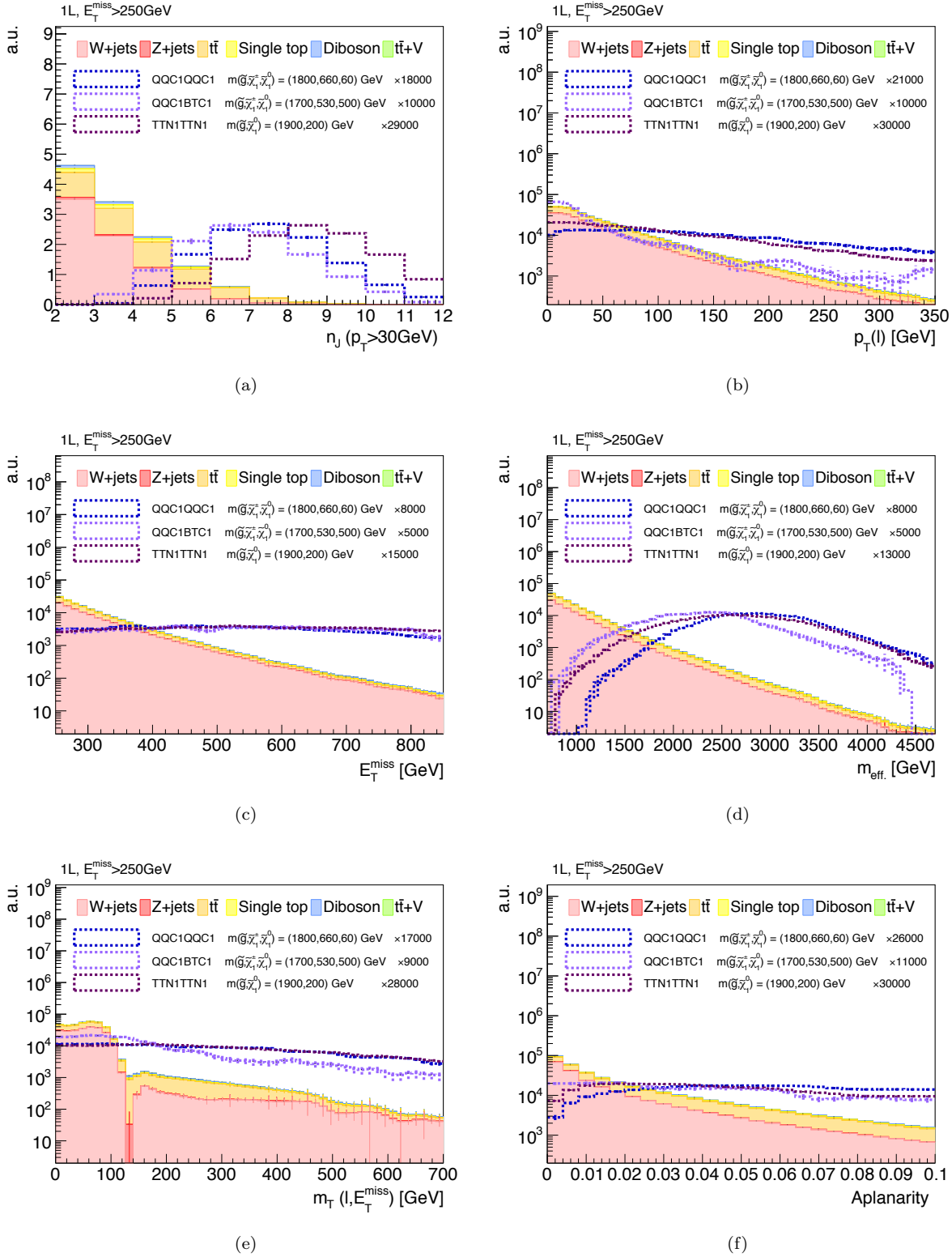


Figure 11:

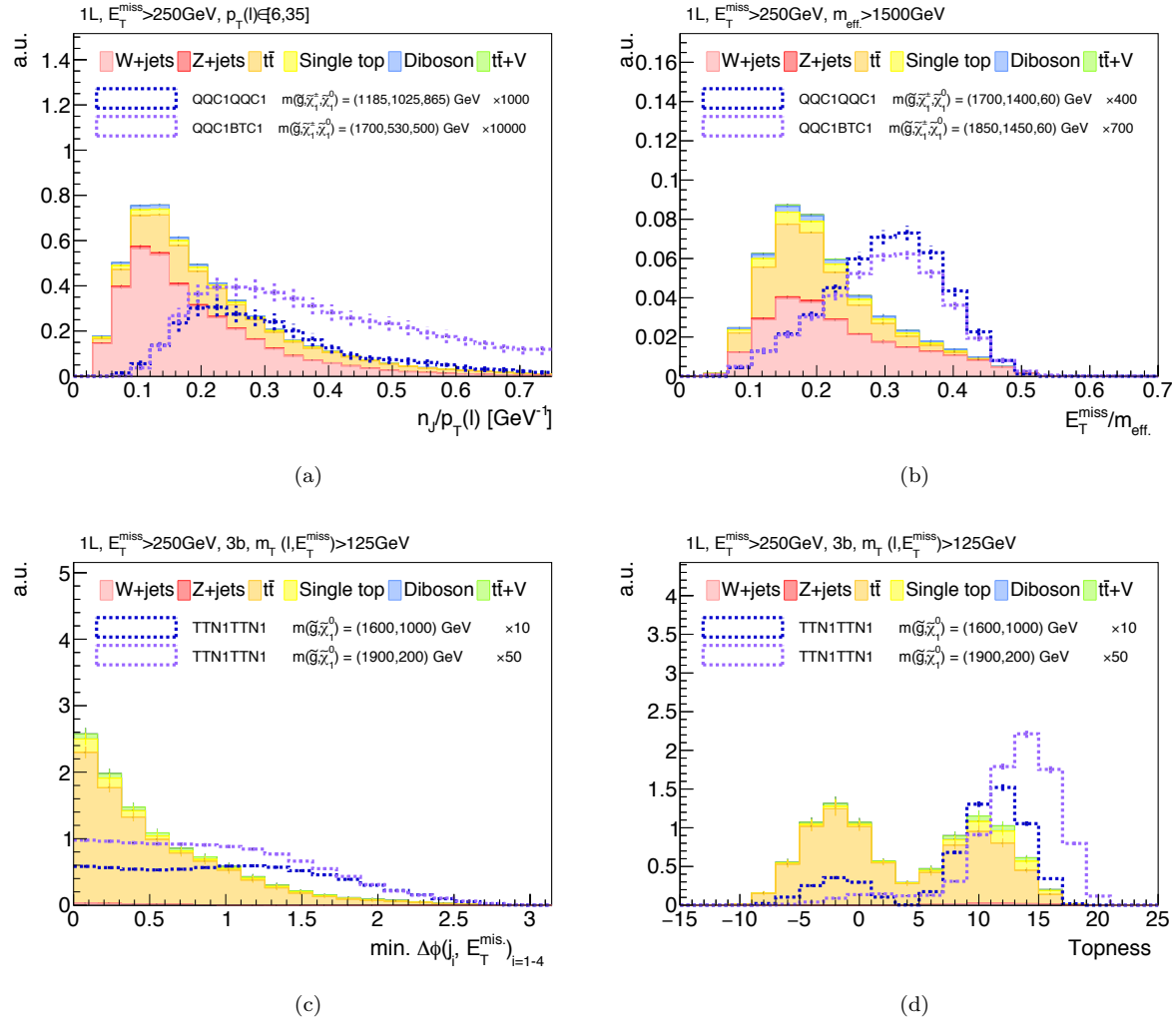


Figure 12:

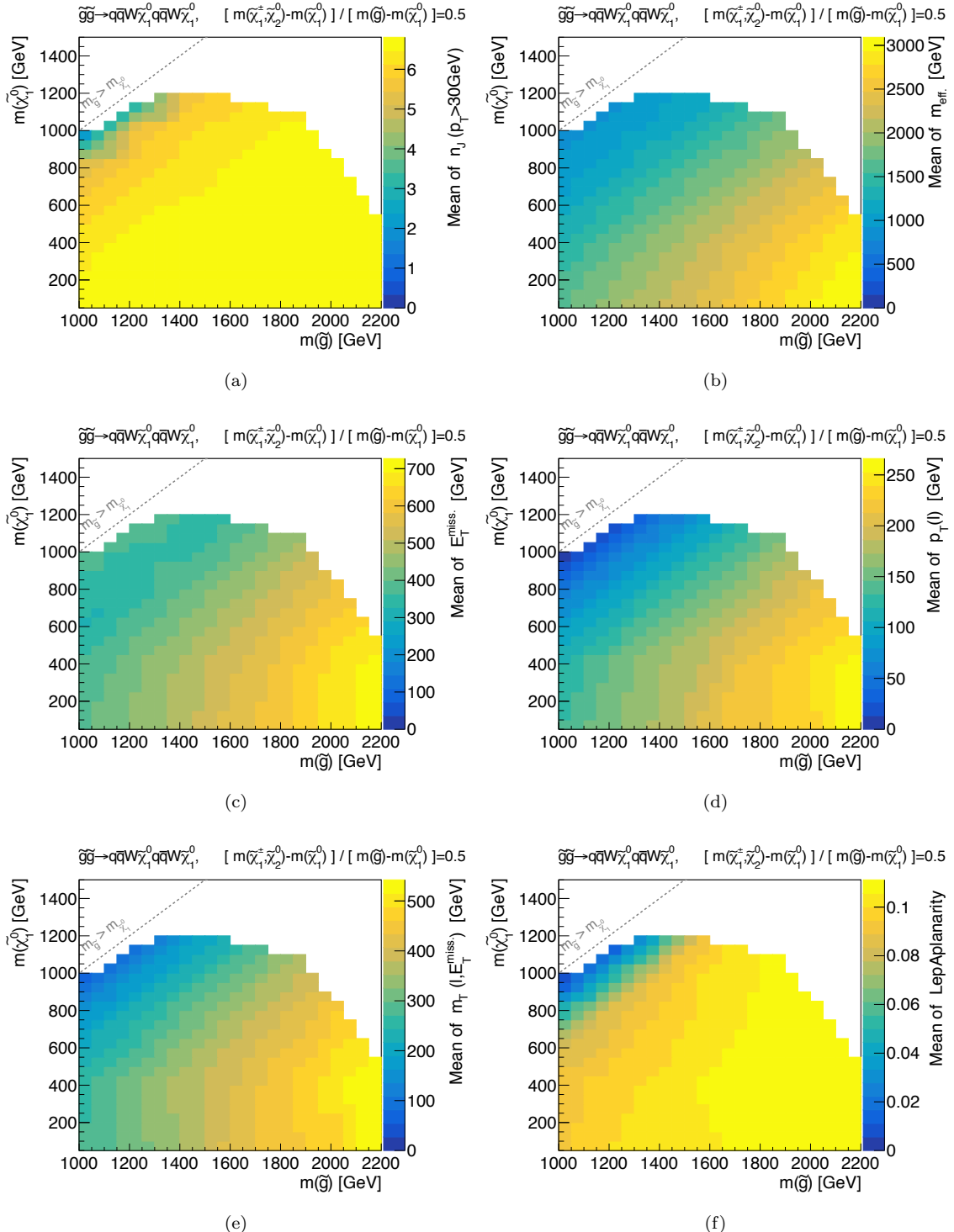


Figure 13: Mean of (a) jet-multiplicity ($p_T > 30$ GeV) (b) m_{eff} (c) E_T^{miss} (d) $p_T(\ell)$ (e) m_T (f) aplanarity, for the QQC1QQC1 $x = 1/2$ grid, after the pre-selection.

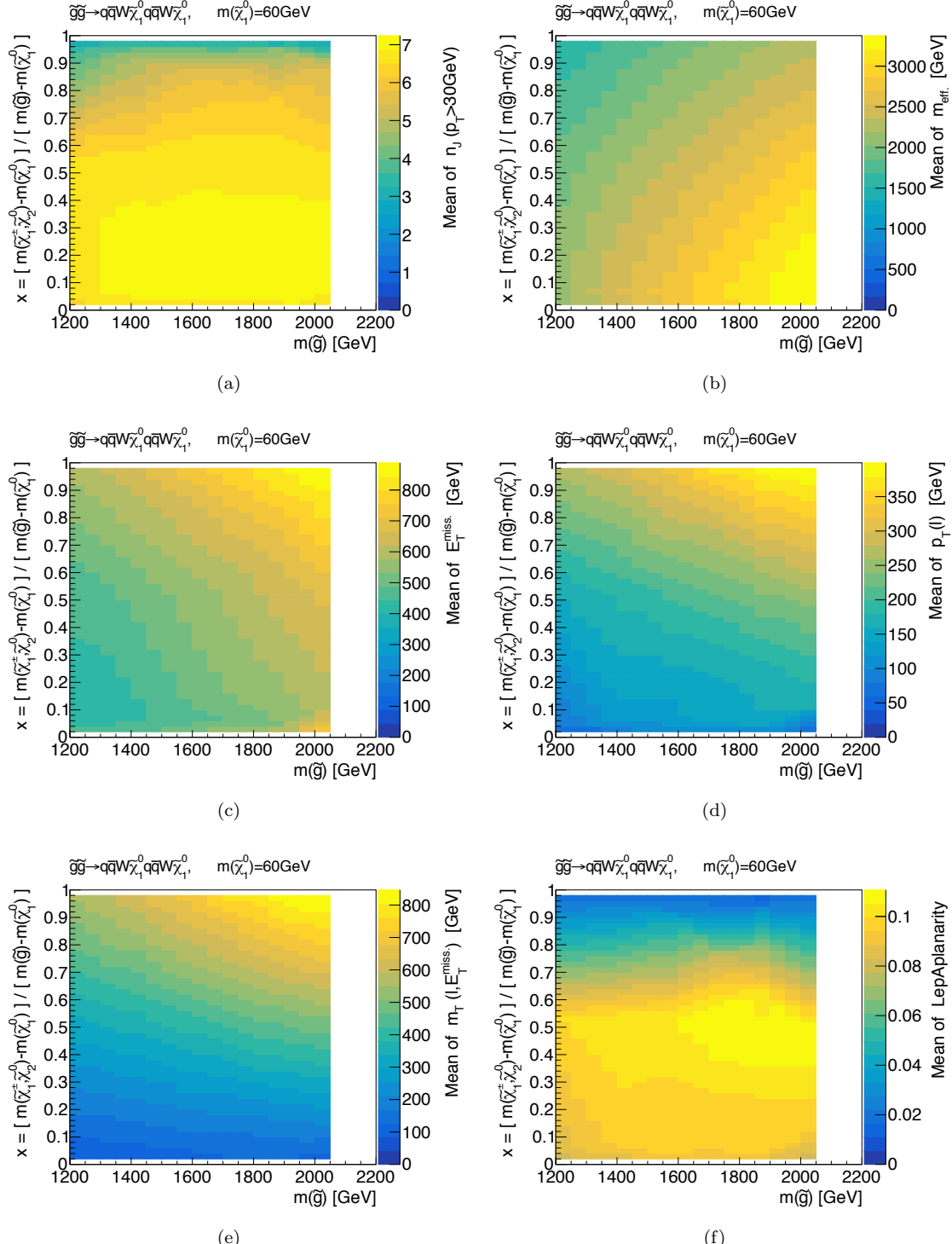


Figure 14: Mean of (a) jet-multiplicity ($p_T > 30\text{GeV}$) (b) m_{eff} (c) $E_T^{\text{miss.}}$ (d) $p_T(\ell)$ (e) m_T (f) aplanarity, for the QQC1QQC1 $m(\tilde{\chi}_1^0) = 60\text{GeV}$ grid, after the pre-selection.

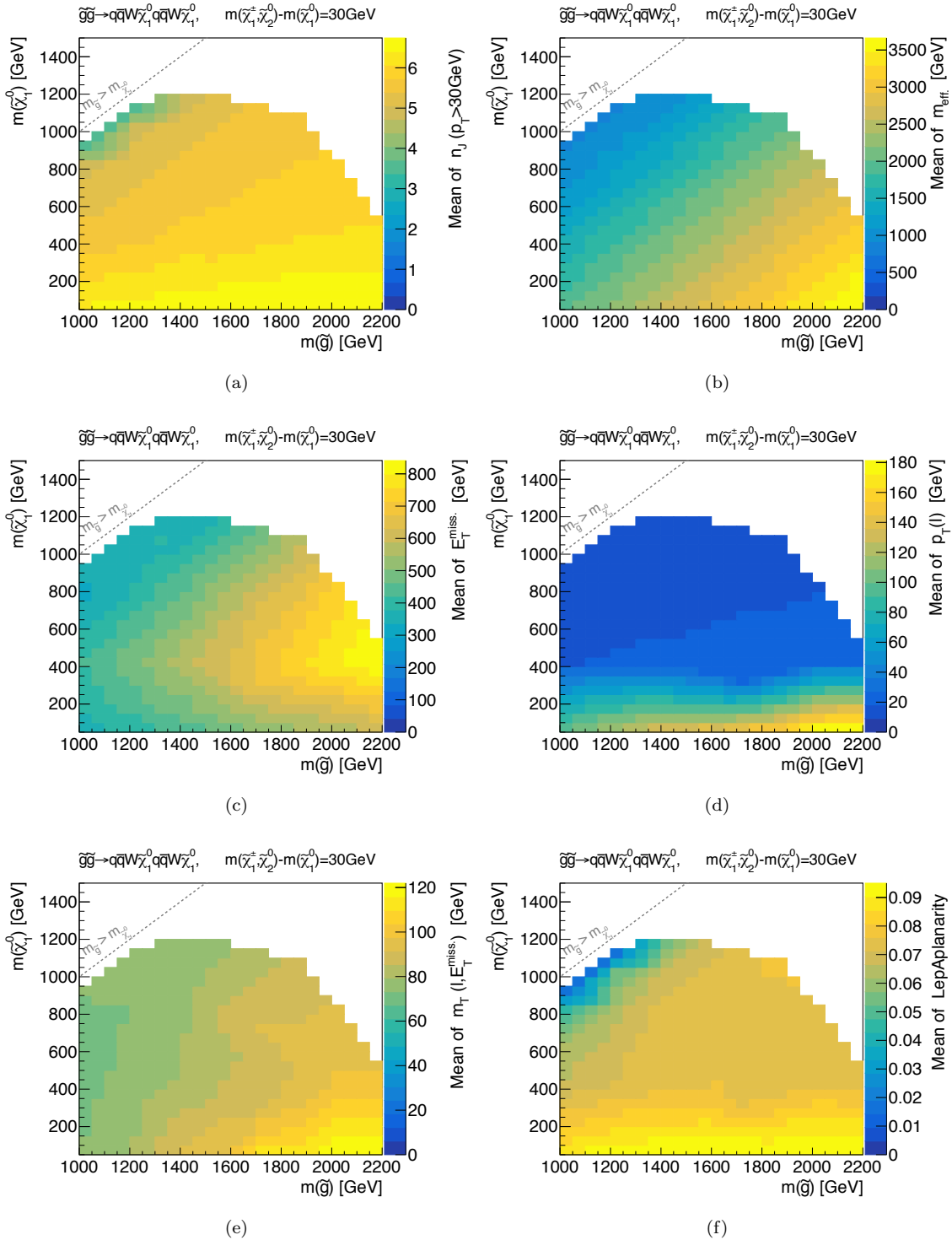


Figure 15: Mean of (a) jet-multiplicity ($p_T > 30$ GeV) (b) m_{eff} (c) E_T^{miss} (d) $p_T(\ell)$ (e) m_T (f) aplanarity, for the QQC1QQC1 $\Delta M = 30$ GeV grid, after the pre-selection.

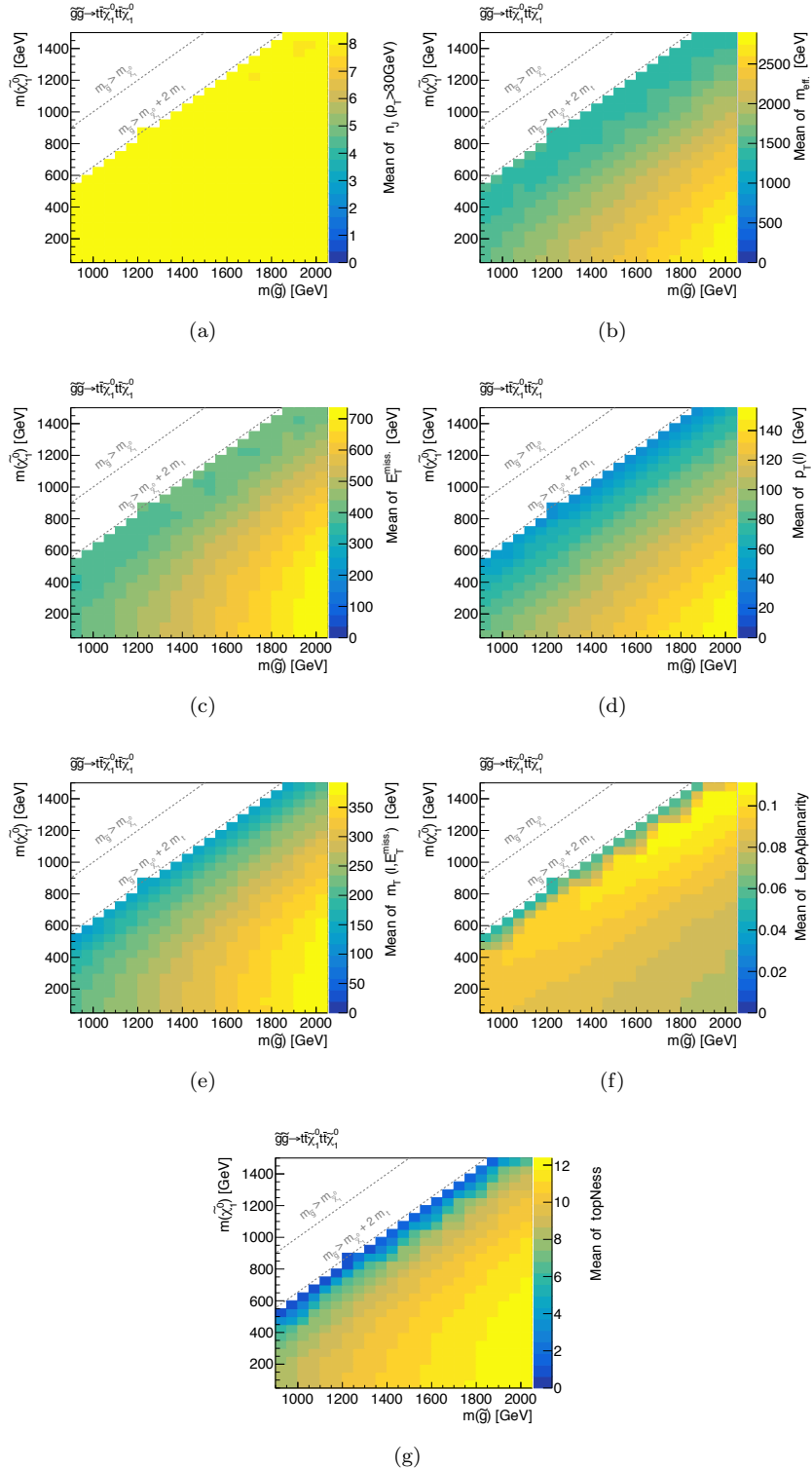


Figure 16: Mean of (a) jet-multiplicity ($p_T > 30$ GeV) (b) m_{eff} (c) E_T^{miss} (d) $p_T(\ell)$ (e) m_T (f) aplanarity, (g) topNess, for the TTN1TTN1 grid, after the pre-selection.

5.3.3 Cut Optimization

After deciding the m_{eff} binning, the cuts on the other kinematic variables are subsequently optimized. The first iteration is done by a coarse grid scan of cuts

(describe the algorithm of the optimization)

Defined signal regions are listed in Tab. 8 - 12, together with the control regions (CR) and validation regions (VR) associated with the SR tower.

Table 8: Definition of signal/control/validation regions (SR/CR/VR) for tower "2J"

	SR	WR/TR	VR E_T^{miss}	VR apl.	VR QCD	VR DB
$n_{\ell,\text{base.}}$	1	1	1	1	1	2
$n_{\ell,\text{sig.}}$	1	1	1	1	0	2
$p_T(\ell)$			[6, 35]			-
$n_J (p_T > 30 \text{ GeV})$			≥ 2			≥ 1
$n_B (p_T > 30 \text{ GeV})$	0/[1,2]	0/[1,2]	-	-	-	0
E_T^{miss}	> 430	[250, 430]	[250, 430]	> 430	> 430	> 250
m_T	> 100	[30, 100]	> 100	[30, 100]	> 100	-
m_{eff}			[1100/1500/1900)			
$E_T^{\text{miss}}/m_{\text{eff}}$	> 0.25	> 0.15	> 0.1	> 0.2	> 0.25	-
$n_J/p_T(\ell)$		> 0.2	> 0.15		> 0.2	-
Topness	> 4	-	-	> 4	> 4	

Table 9: Definition of signal/control/validation regions (SR/CR/VR) for tower ”**6J**”

	SR	WR/TR	VR m_T	VR apl.	VR QCD	VR DB
$n_{\ell,\text{base.}}$	1	1	1	1	1	2
$n_{\ell,\text{sig.}}$	1	1	1	1	0	2
$p_T(\ell)$				> 35		
$n_J (p_T > 30\text{GeV})$				≥ 6		≥ 5
$n_B (p_T > 30\text{GeV})$	$0/[1,2]$	$0/[1,2]$	-	-	-	0
E_T^{miss}	> 350	> 300	> 250	> 350	> 350	> 250
m_T	> 175	$[40, 125]$	$[125, 400]$	$[40, 125]$	> 125	-
m_{eff}				$[1100/1600/2100]$		
Aplanarity	> 0.06	< 0.06	< 0.04	> 0.06	> 0.06	< 0.06
Topness	> 4	-	-	> 4	> 4	

 Table 10: Definition of signal/control/validation regions (SR/CR/VR) for tower ”**Lowx**”

	SR	WR/TR	VR m_T	VR apl.	VR QCD	VR DB
$n_{\ell,\text{base.}}$	1	1	1	1	1	2
$n_{\ell,\text{sig.}}$	1	1	1	1	0	2
$p_T(\ell)$				$[6, 35]$		-
$n_J (p_T > 30\text{GeV})$				≥ 4		≥ 3
$n_B (p_T > 30\text{GeV})$	$0/[1,2]$	$0/[1,2]$	-	-	-	0
$p_T(j_4)$				> 80		-
E_T^{miss}	> 350	> 300	> 300	> 350	> 350	> 250
m_T	> 100	$[30, 100]$	$[100, 450]$	$[30, 100]$	> 100	-
m_{eff}				> 1900		
Aplanarity	> 0.02	< 0.02	< 0.02	> 0.02	> 0.02	< 0.04
Topness	> 4	-	-	> 4	> 4	

Table 11: Definition of signal/control/validation regions (SR/CR/VR) for tower "Highx"

	SR	WR/TR	VR m_T	VR apl.	VR QCD	VR DB
$n_{\ell,\text{base.}}$	1	1	1	1	1	2
$n_{\ell,\text{sig.}}$	1	1	1	1	0	2
$p_T(\ell)$				> 35		
$n_J (p_T > 30\text{GeV})$				≥ 4		≥ 3
$n_B (p_T > 30\text{GeV})$	$0/[1,2]$	$0/[1,2]$	-	-	-	0
E_T^{miss}	> 300	> 300	> 300	> 300	> 300	> 250
m_T	> 300	$[30, 125]$	$[125, 600]$	$[30, 125]$	> 450	-
m_{eff}				> 2000		
$E_T^{\text{miss}}/m_{\text{eff}}$	> 0.25	> 0.2	> 0.15	> 0.25	> 0.25	> 0.2
Aplanarity	> 0.01	< 0.01	-	> 0.01	> 0.01	< 0.02
Topness	> 4	-	-	> 4	> 4	

Table 12: Definition of signal/control/validation regions (SR/CR/VR) for tower "3B"

	SR	TR	VR m_T	VR apl.	VR QCD
$n_{\ell,\text{base.}}$	1	1	1	1	1
$n_{\ell,\text{sig.}}$	1	1	1	1	0
$p_T(\ell)$				> 15	
$n_J (p_T > 30\text{GeV})$				≥ 7	
$n_B (p_T > 30\text{GeV})$				≥ 3	
E_T^{miss}	> 300	> 250	> 250	> 250	> 300
$m_T(p_T(\ell), E_T^{\text{miss}})$	> 175	$[30, 125]$	$[125, 450]$	$[30, 125]$	> 175
m_{eff}				$[1000/1750)$	
Aplanarity	> 0.01	-	-	> 0.01	> 0.01
$\min_{i=1-4} \Delta\phi(j_i, E_T^{\text{miss}})$	> 0.45	-	-	> 0.3	> 0.45
Topness	> 6	-	-	> 6	> 6

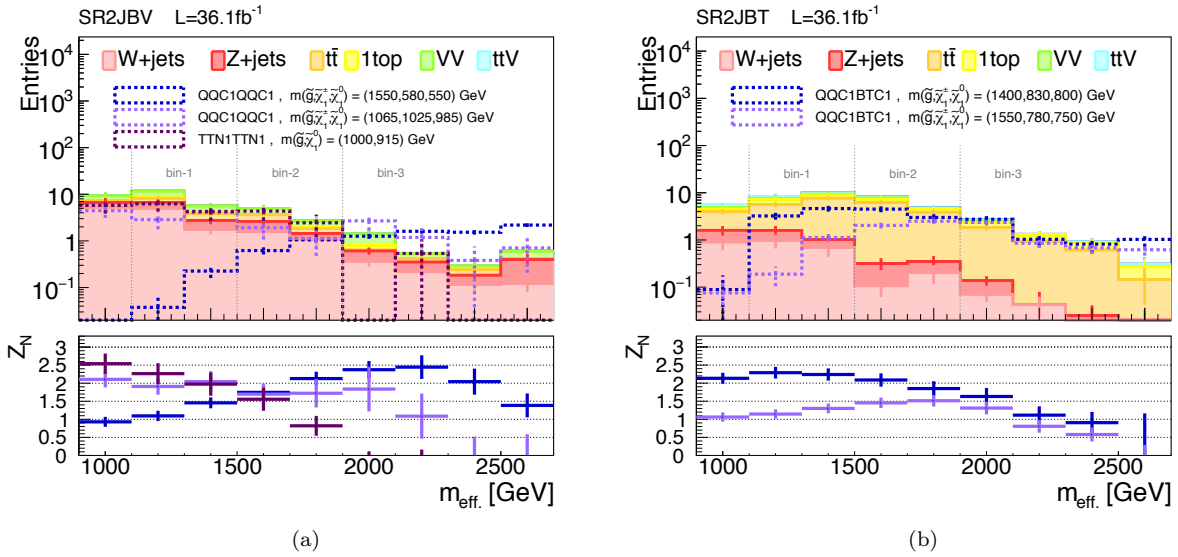


Figure 17:

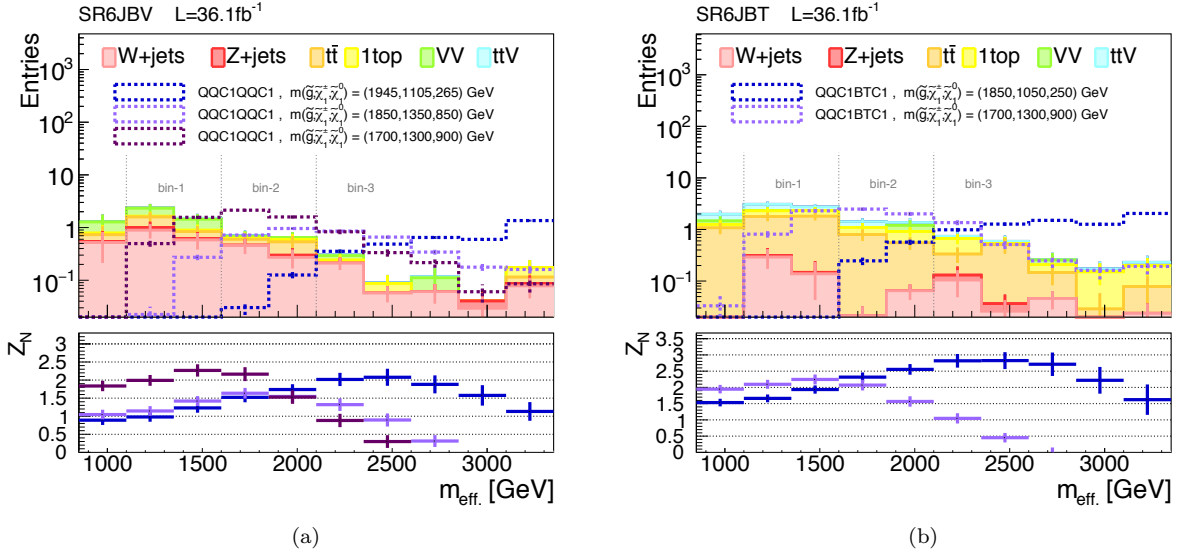


Figure 18:

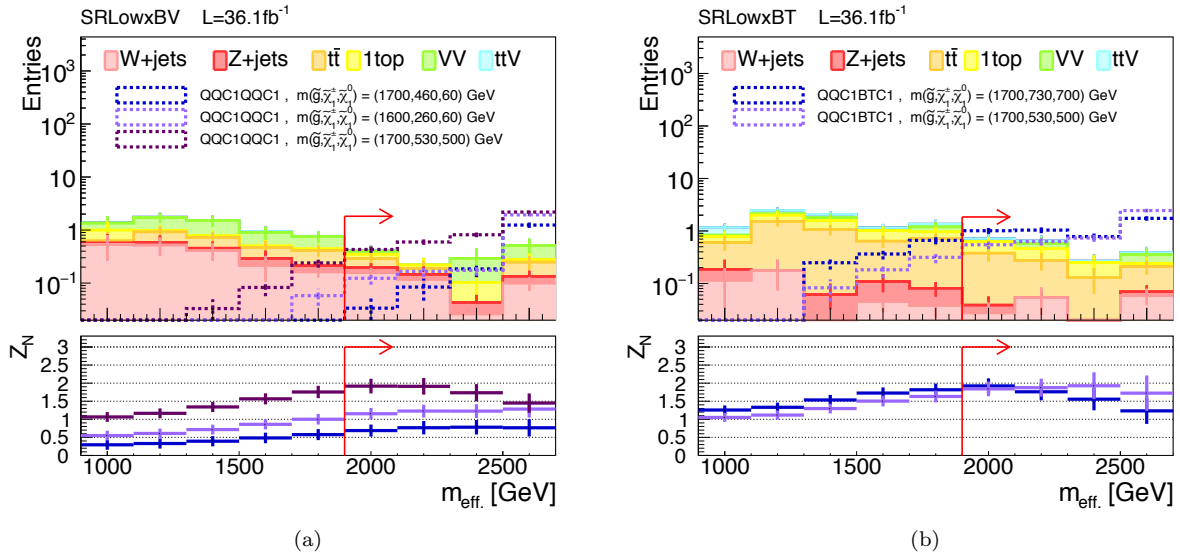


Figure 19:

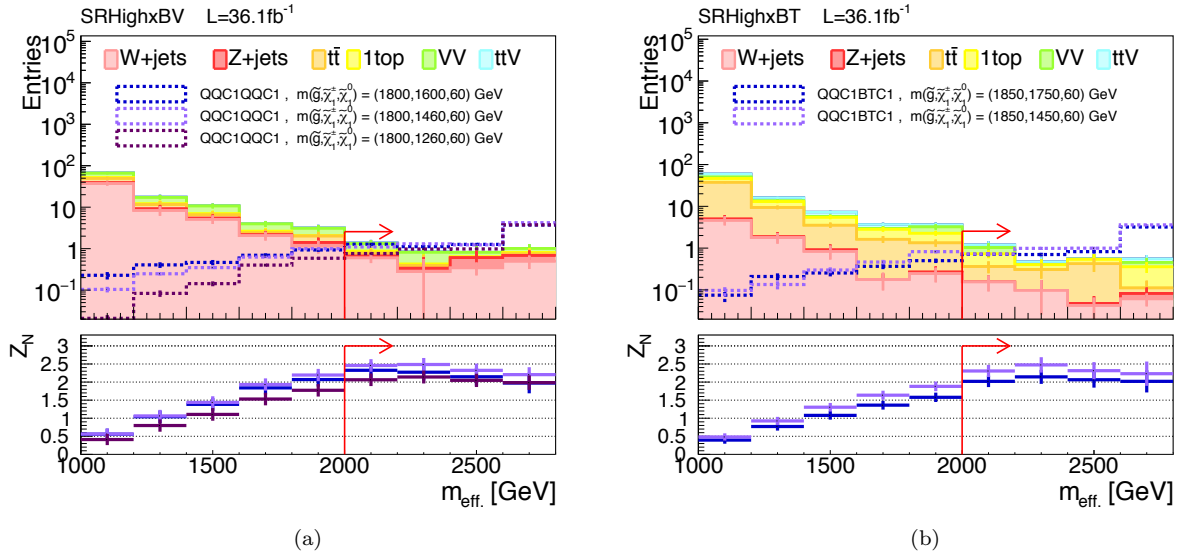
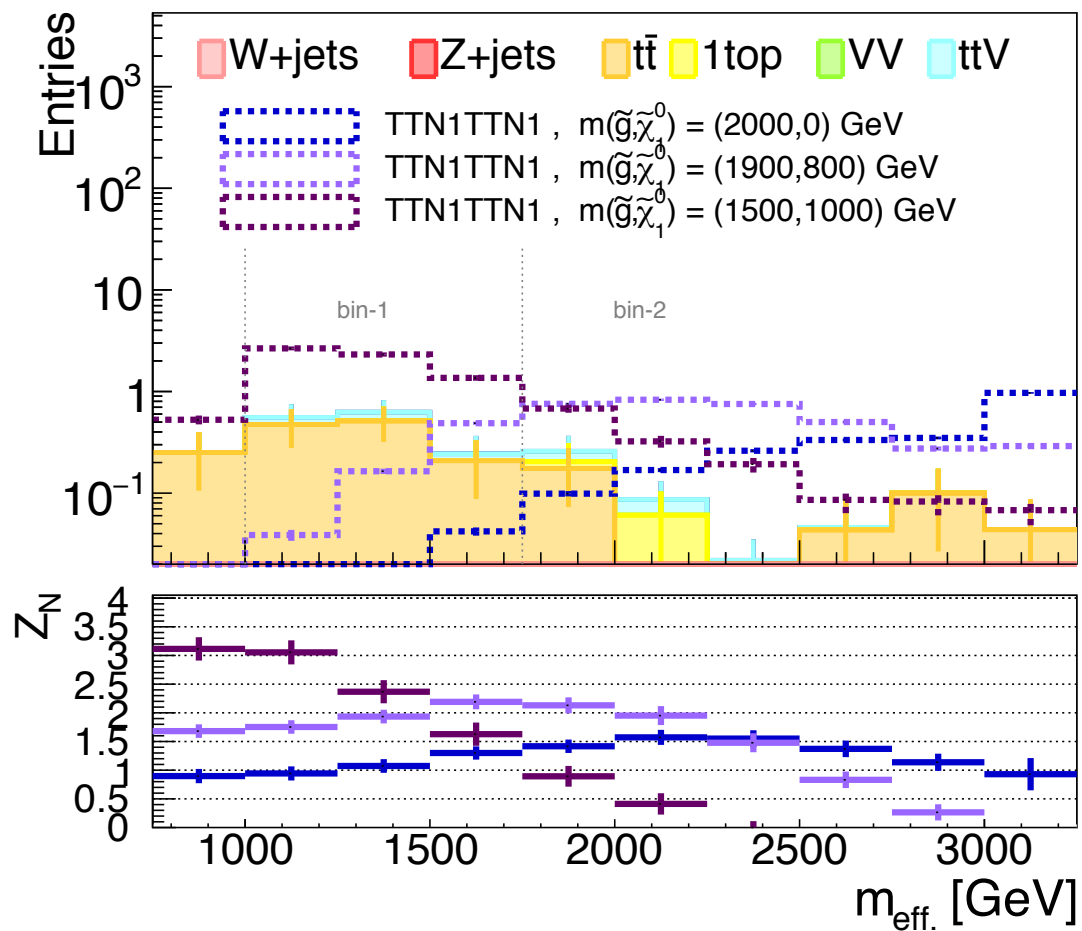


Figure 20:

SR3B L=36.1fb⁻¹



(a)

Figure 21:

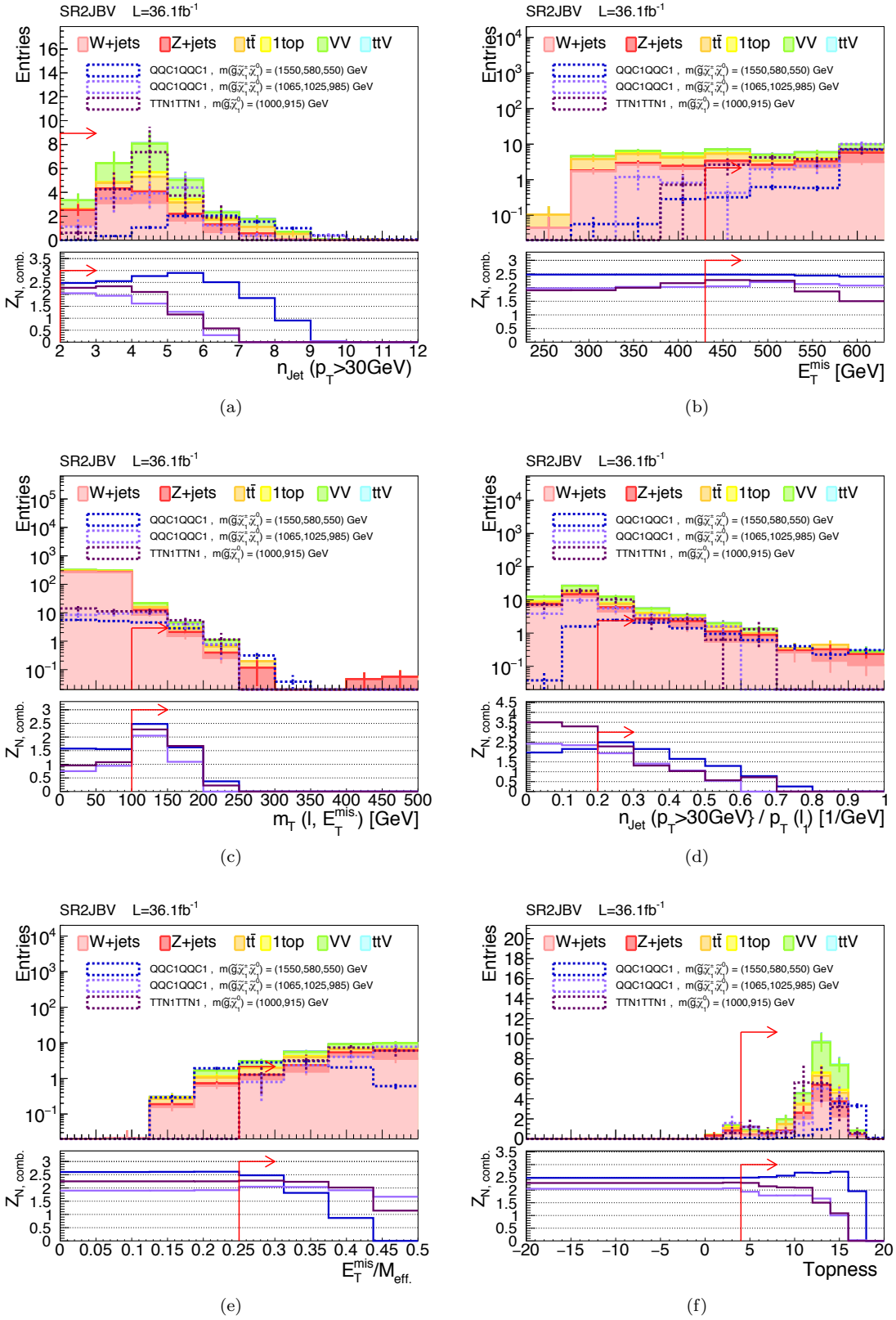


Figure 22:

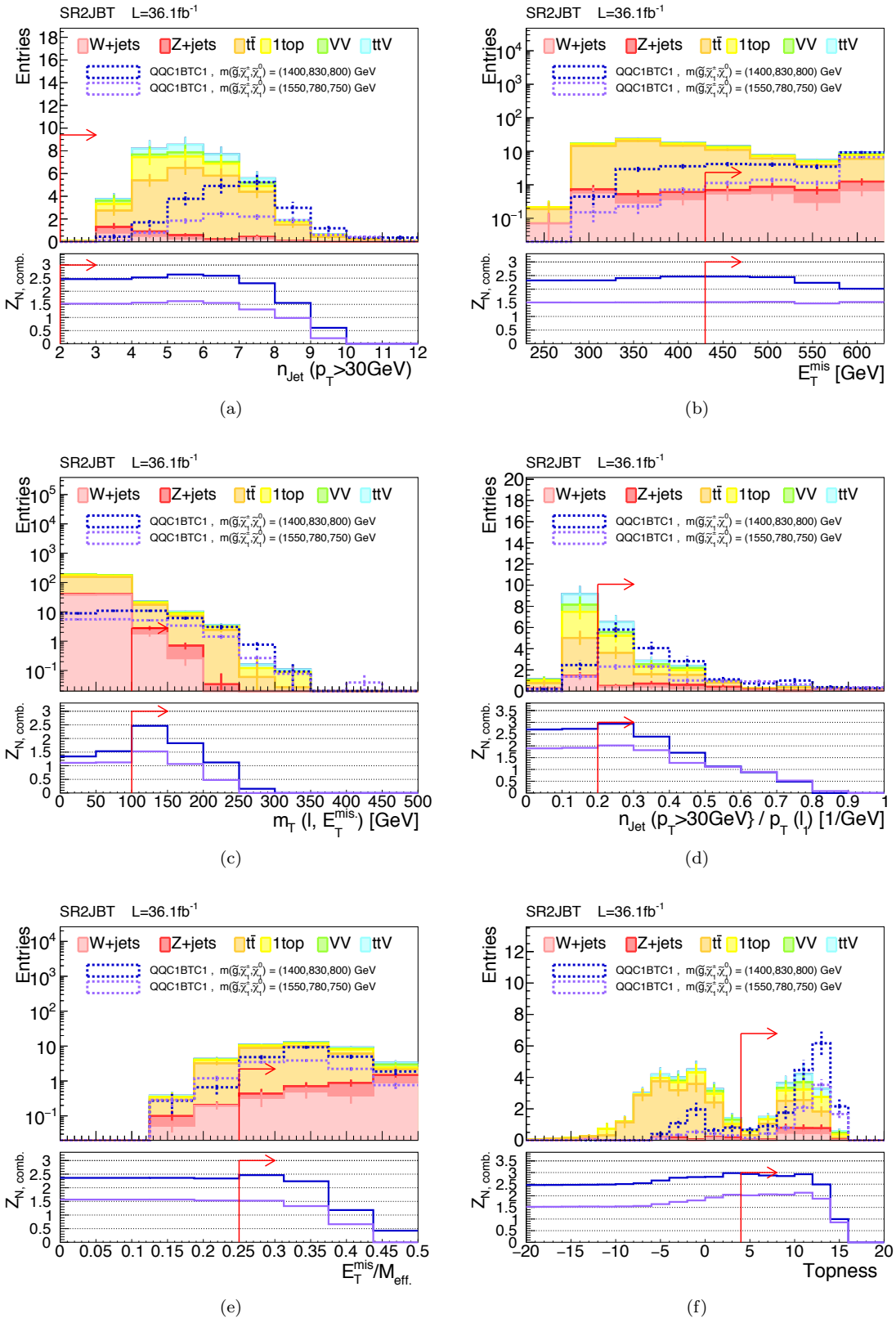


Figure 23:

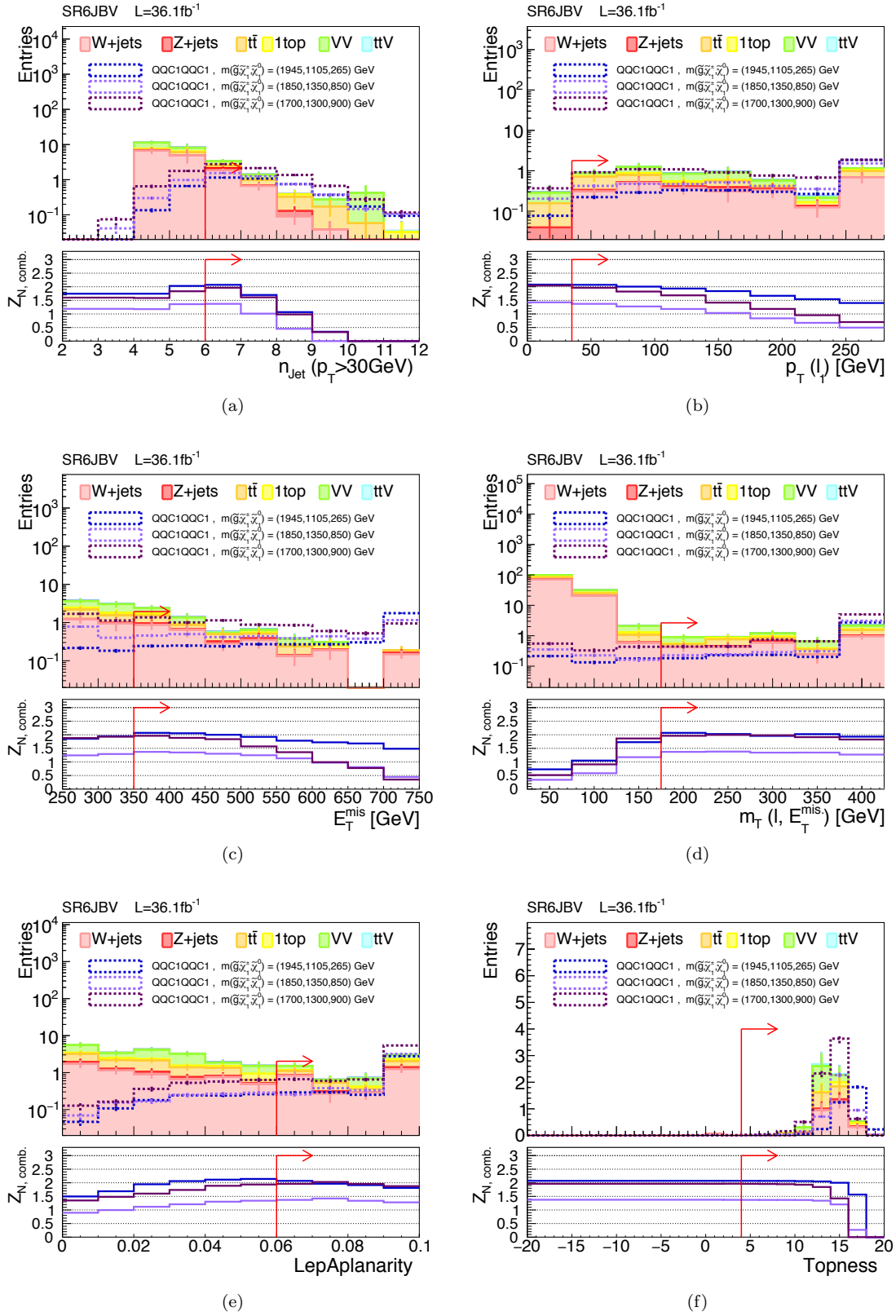


Figure 24:

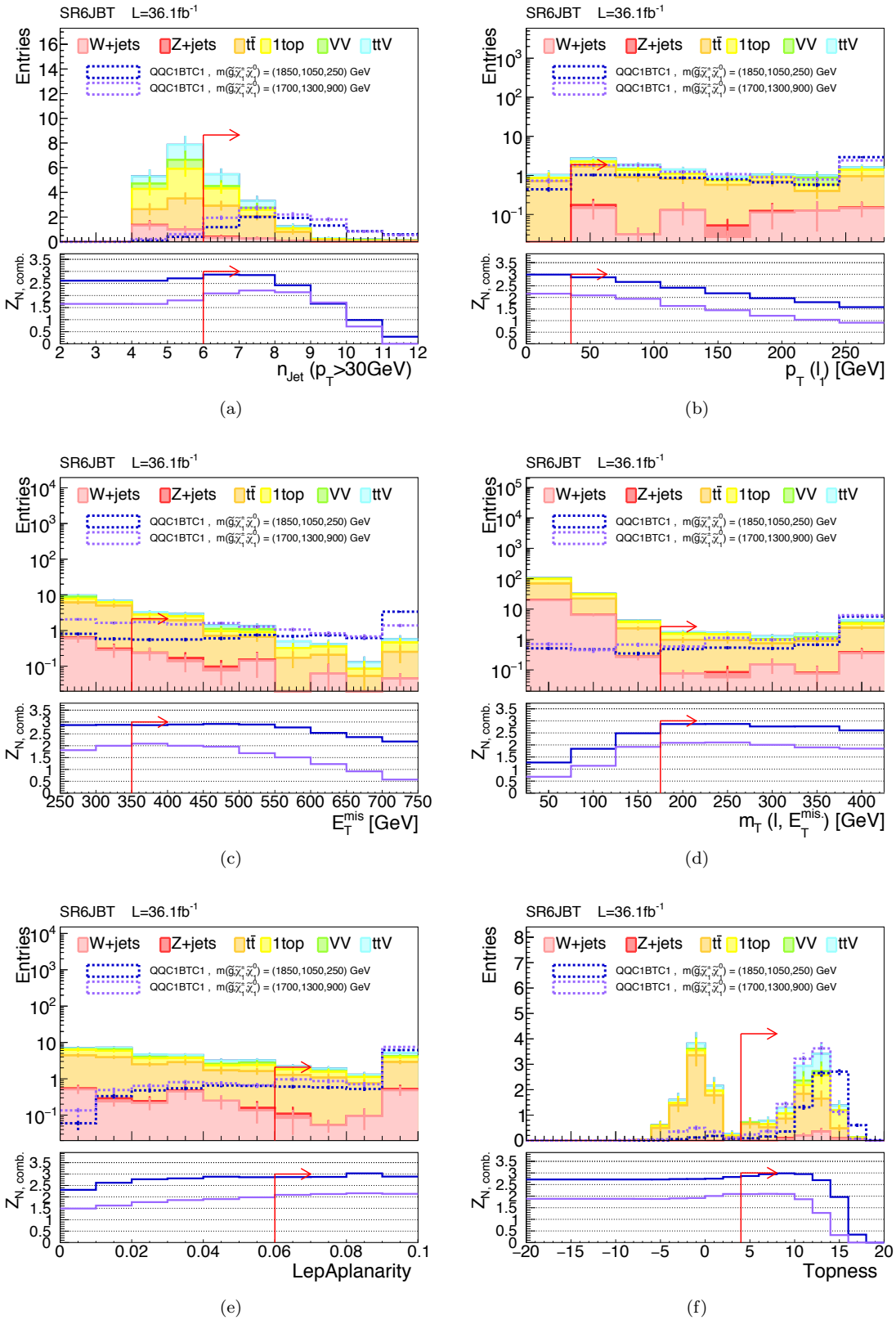


Figure 25:

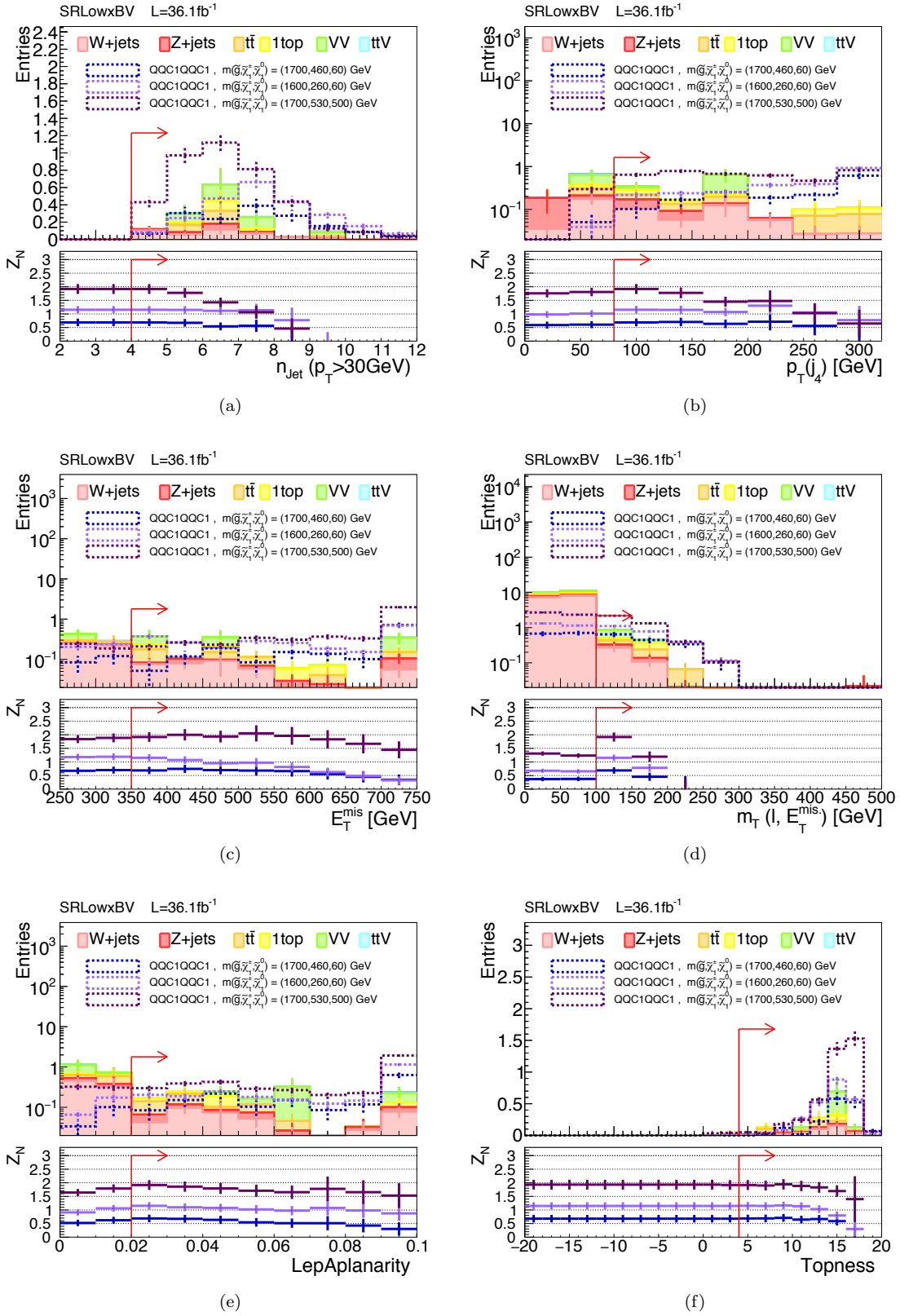


Figure 26:

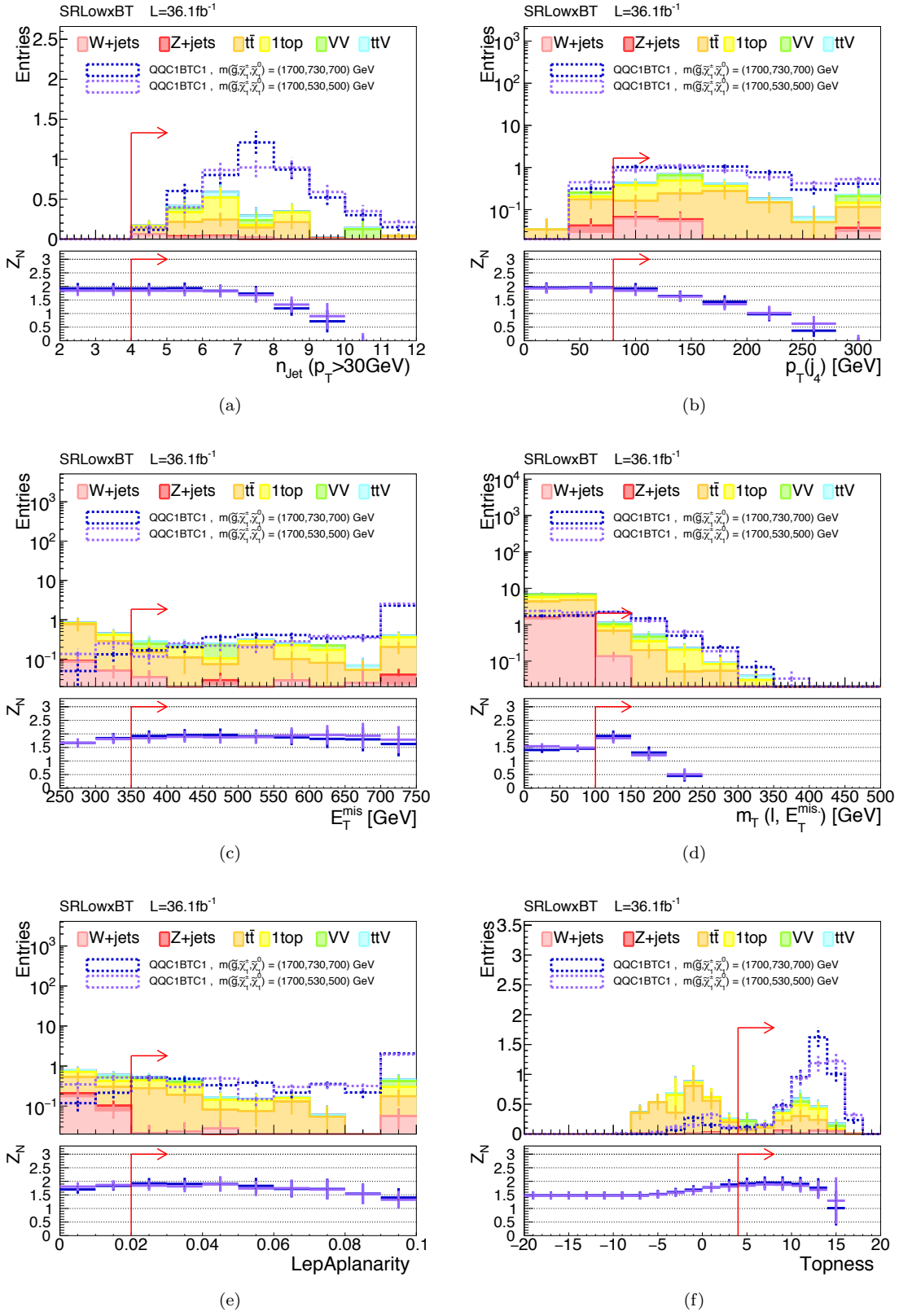


Figure 27:

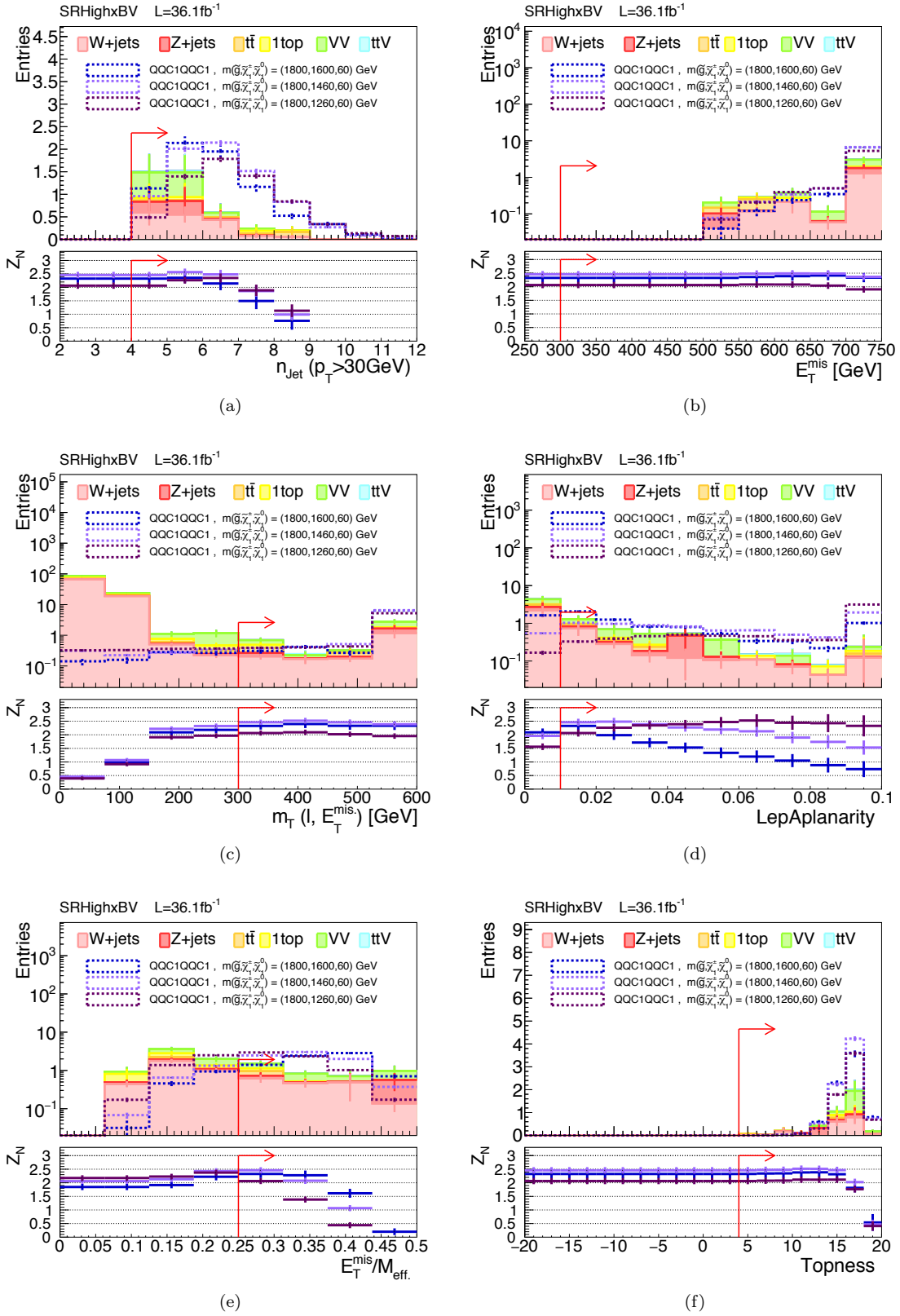


Figure 28:

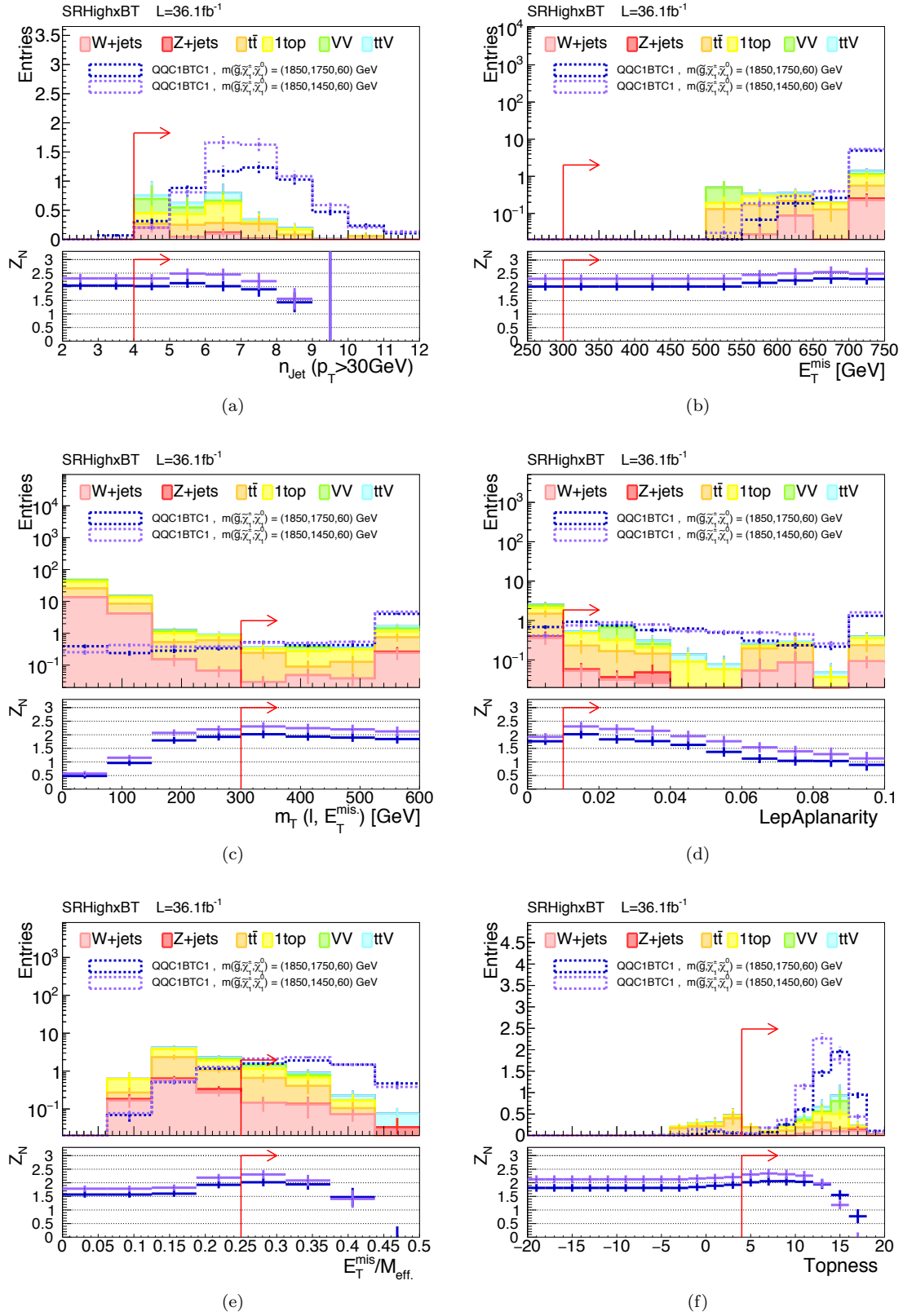


Figure 29:

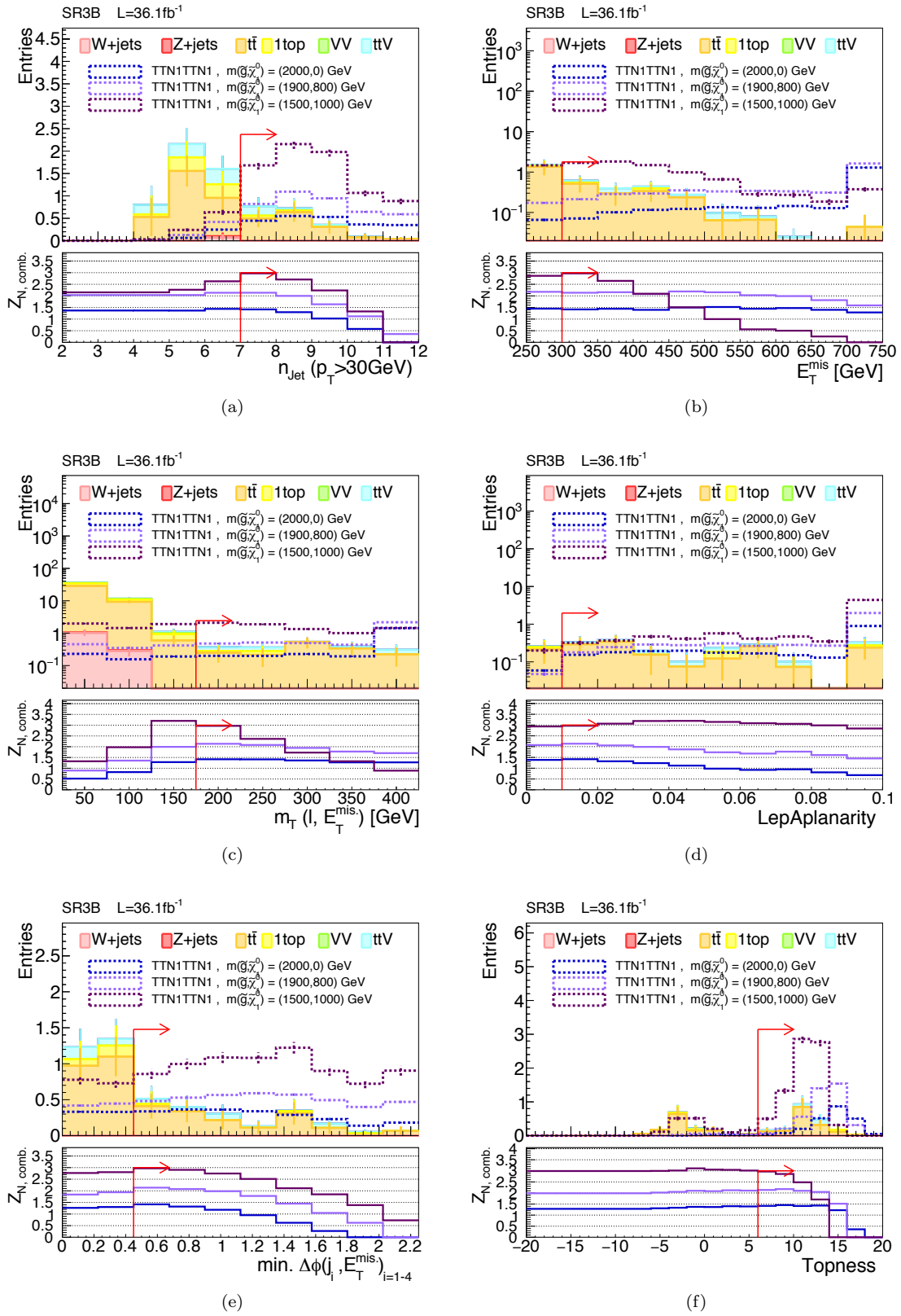


Figure 30:

5.3.4 Expected Sensitivity

Expected excluded limits driven by the combined and individual signal regions are shown in Fig. 32 and 31

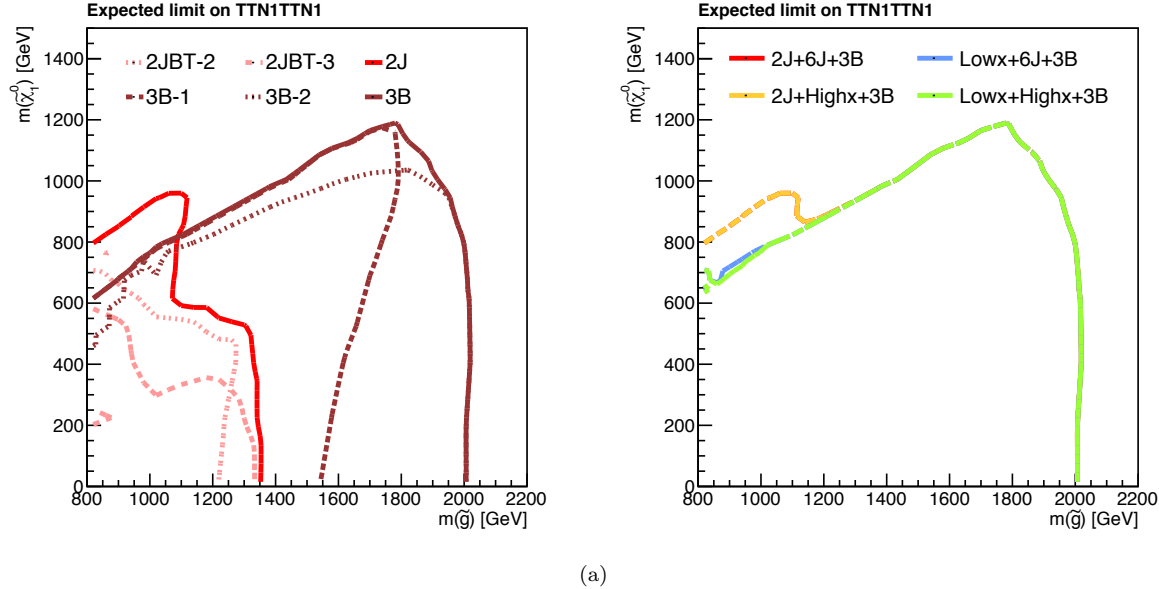
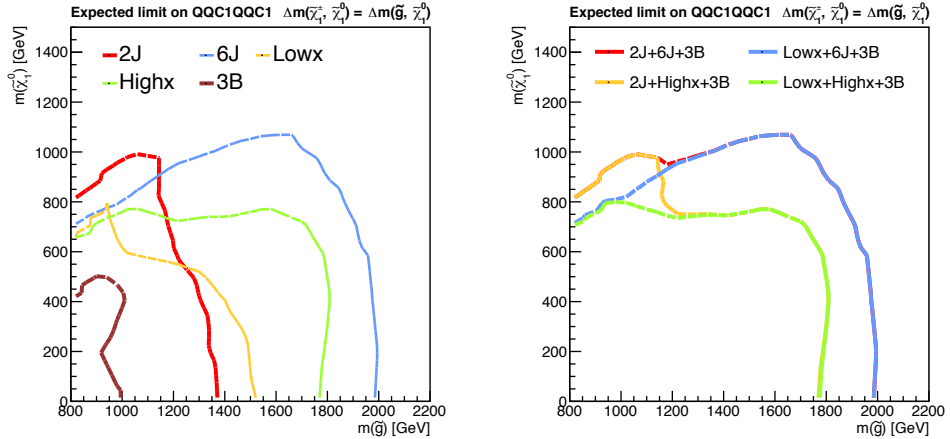
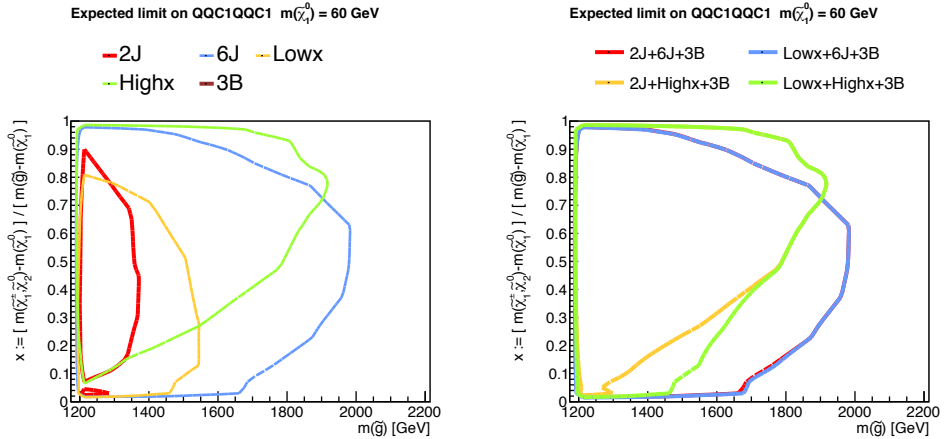


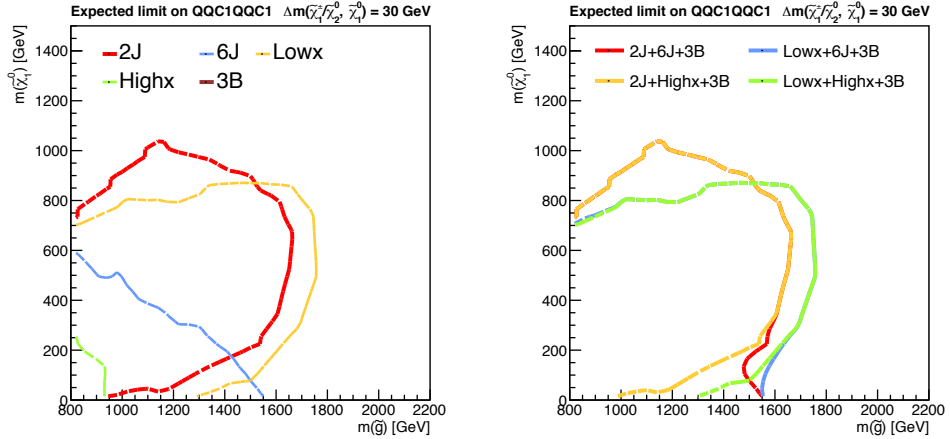
Figure 31: Expected exlusion (95%CL) for the benchmark model TTN1TTN1.



(a)

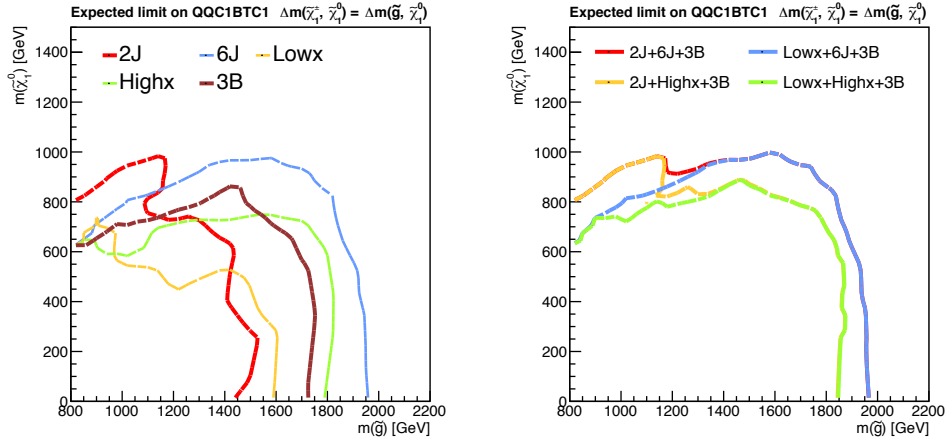


(b)

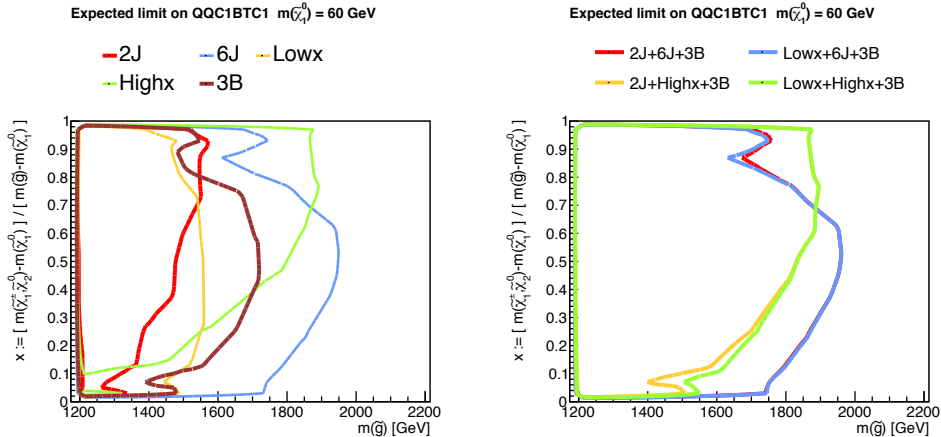


(c)

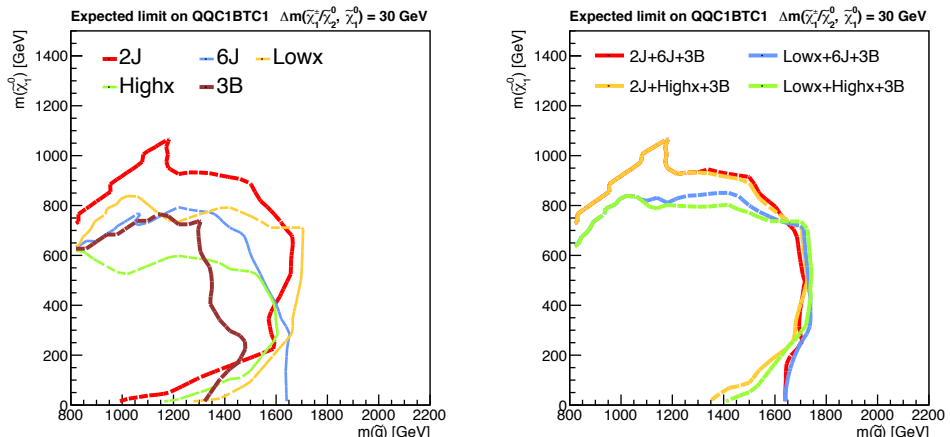
Figure 32: Projected expected exclusion (95%CL) for the benchmark model QQC1QQC1 onto the (a) $x = 1/2$ (b) $m_{\tilde{\chi}_1^0} = 60 \text{ GeV}$ (c) $\Delta m(\tilde{\chi}_1^\pm, \tilde{\chi}_1^0) = 30 \text{ GeV}$ grid.



(a)



(b)



(c)

Figure 33: Projected expected exclusion (95%CL) for the benchmark model QQC1BTC1 onto the (a) $x = 1/2$ (b) $m_{\tilde{\chi}_1^0} = 60 \text{ GeV}$ (c) $\Delta m(\tilde{\chi}_1^\pm, \tilde{\chi}_1^0) = 30 \text{ GeV}$ grid.

6 Standard Model Background Estimation

This section presents the methods used for estimating backgrounds. After reviewing the breakdown in the signal regions and how they evade the event selection, two methods are introduced to estimate different background components, namely, **object replacement method** for estimating the di-leptonic components and **kinematical extrapolation method** for the rest.

6.1 Background Breakdown in the Signal Regions

The breakdown of physics processes in the signal regions are shown in Fig. 35. $W + \text{jets}$ and $t\bar{t}$ dominate over the b-tagged and b-vetoed regions respectively in general, while dibosons and single-top are sub-dominant. The **3B** towers are completely dominated by $t\bar{t}$, where 60 % of them are with heavy flavor jets via radiative gluon splitting ($t\bar{t} + cc/bb$) while the rest are with one light flavor jet or hadronocaying τ faking into b-tagged jet ($t\bar{t} + b_{\text{fake}}$).

Backgrounds also follow the classification below depending on the mechanism they pass the selection:

“**1L**”: Processes with exact 1 prompt lepton.

“**2L**”: Processes with 2 leptons including tau (“di-leptonic processes”)

“**0L**”: Processes with 0 real-lepton + 1 fake-lepton.

“**1L**” consists of processes with exactly one leptonically decaying W-boson such as $W + \text{jets}$ and semi-leptonically decaying top quark processes. This is by far the dominant component at 1-lepton preselection level, however is drastically suppressed after a harsh m_T cut since the they are largely truncated at m_W . After the m_T cut, the remnant events are typically either: 1) Drell-Yan process with virtual heavy intermediate W boson, or 2) events with badly measured MET leading to prolonged tail in m_T . The former contribution is usually larger although the latter becomes comparable with increasing jet activity.

On the other hand, the “**2L**” processes become relatively significant after the m_T cut, because the source of missing transverse momentum is multiple thus they have no reason to cut-off at m_W . The main physics processes are di-leptonic decaying $t\bar{t}$, Wt , WW etc. They fall into 1-lepton regions for mainly two regions:

” $\ell\ell_{\text{mis}}$.”

Events with two real light flavor leptons (e, μ) and one of them fails the “baseline” requirement (“missing lepton”).

” $\ell\tau_h$ ”

Events with a real light flavor lepton and a hadronically decaying tau lepton.

Missing leptons can be further categorized into four groups:

”**Out Acc.**”

Leptons going outside the acceptance of “baseline” requirement i.e. $p_T > 6(7)\text{GeV}, |\eta| < 2.5$ for electrons (muons).

”Mis. Reco.”

Leptons failing the reconstruction i.e a truth lepton that can not be associated with any of reconstructed electrons/muons in the xAOD container.

”Mis. ID”

Reconstructed leptons failing the electron/muon ID for the “baseline” requirement.

”Mis. OR”

Reconstructed leptons passing the ID for ”baseline” requirement but killed in overlap removal.

One nice thing about this **”2L”** components is that 2-lepton regions are available for control regions in the estimation. Since no signal regions are set there, exactly the same phase space with respect to SRs can be exploited. This is performed by the “object replacement method” as detailed in the following sub-section.

The third category **”0L”** involves events with a fake lepton, which is negligible except regions dealing with soft leptons (**”2J”** and **”Low-x”**). Dominant contribution is from $W \rightarrow \tau\nu$ and $Z \rightarrow \nu\nu$ which accompanies large MET by neutrinos, while multi-jet process can still be formidable due to the spectacularly high cross-section and the fact that current up-to-NNLO MC is not very reliable in describing the tail. A series of validation regions (VR-QCD) are set to confirm that the contribution is indeed negligible.

Fig.34 illustrate background breakdown in SRs based on this classification. While **”1L”** overwhelms in b-vetoed SRs, **”2L”** particularly $\ell\tau_h$ dominates the other regions.

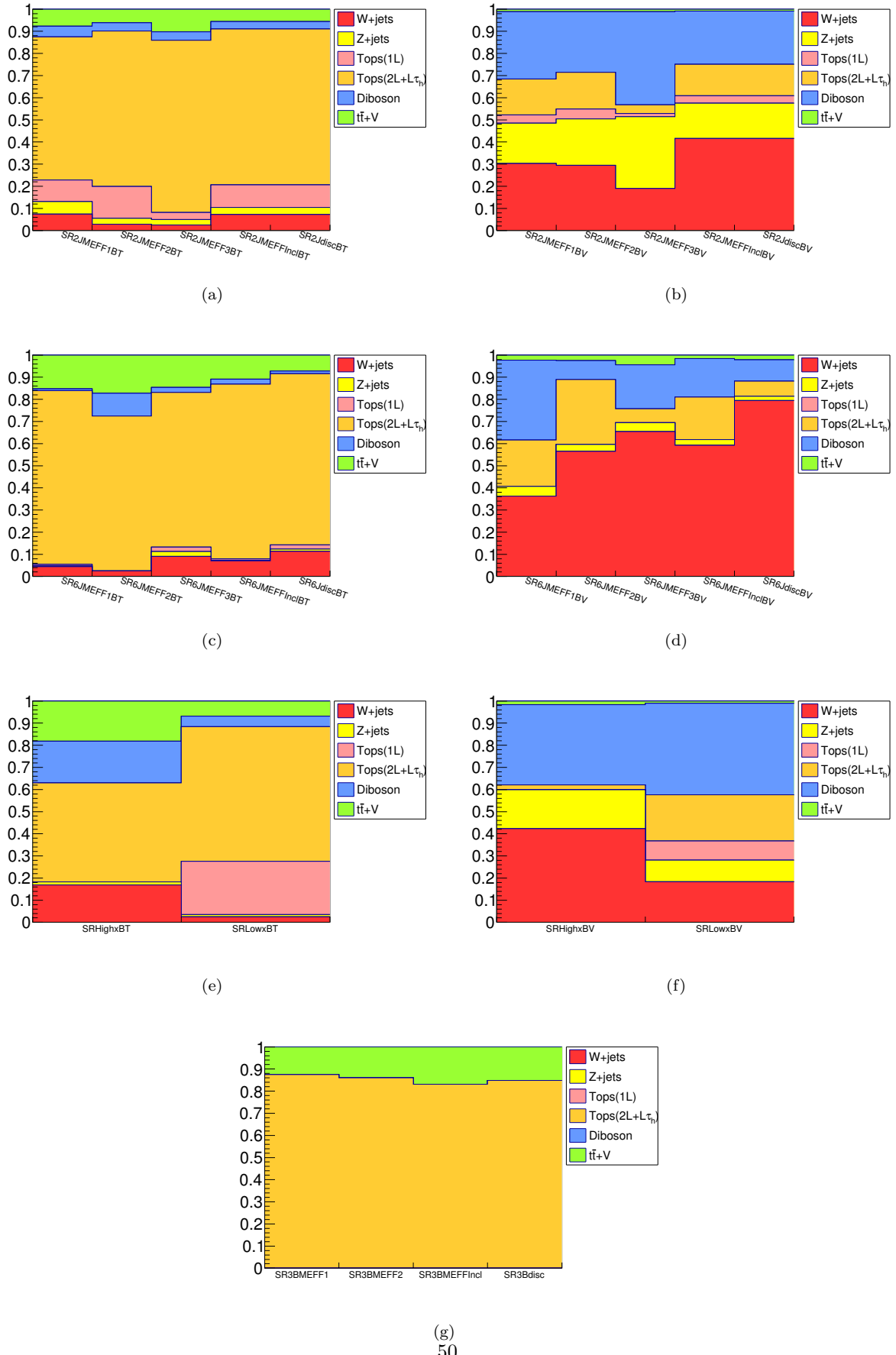


Figure 34: Background composition in (a) SR2JBT (b) SR2JBV (c) SR6JBT (d) SR6JBV (e) SR-Lowx/HighxBT (f) SRLowx/HighxBV (g) SR3B.

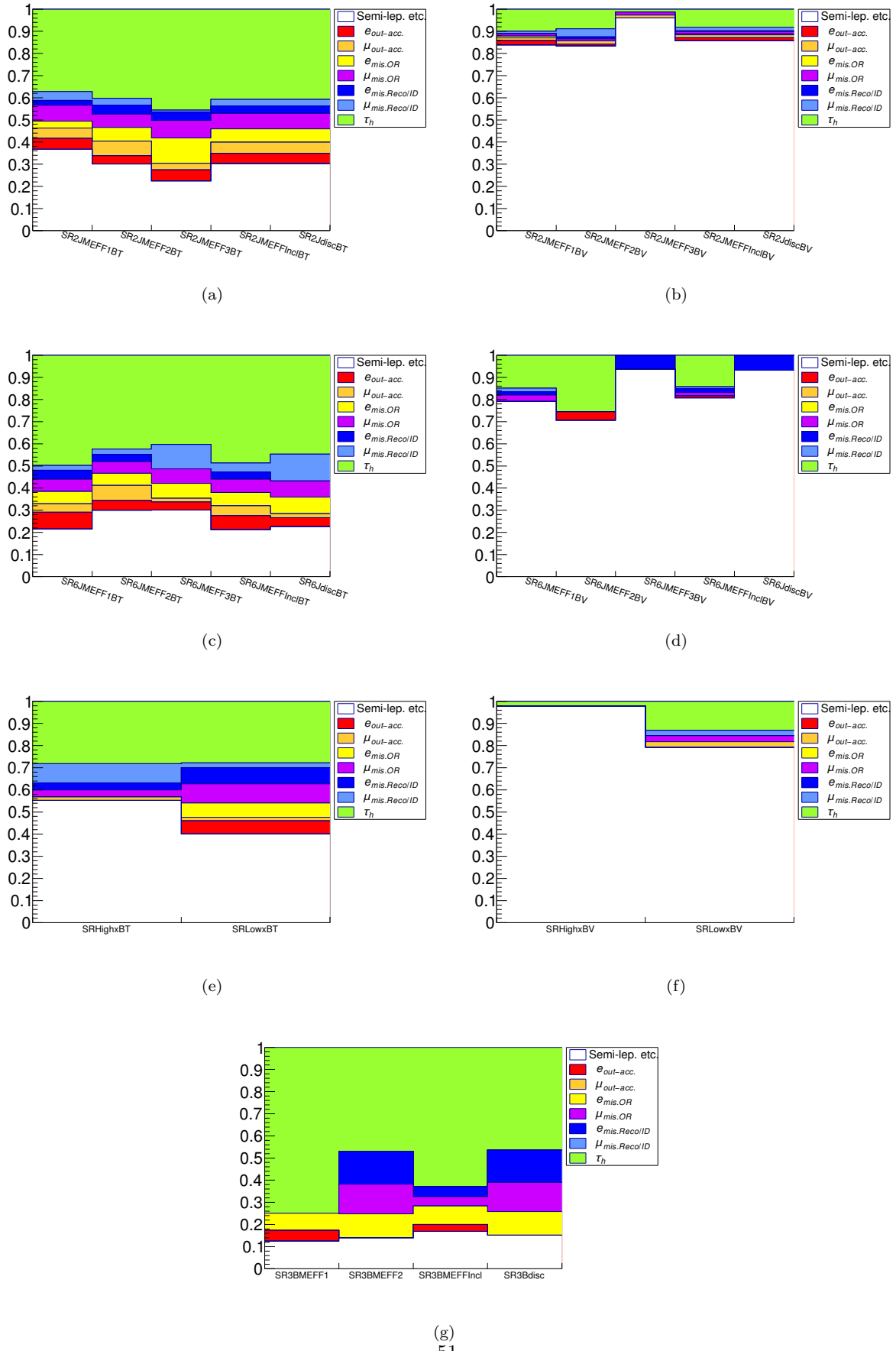


Figure 35: Background composition in (a) SR2JBT (b) SR2JBV (c) SR6JBT (d) SR6JBV (e) SR-Lowx/HighxBT (f) SRLowx/HighxBV (g) SR3B.

6.2 MC vs Data Comparison and the MC mis-modeling

The reliability of MC on dominant background processes ($W + \text{jets}$ and $t\bar{t}$) is examined in pre-selection regions defined in Tab.???. Each pre-selection region is intended to be dominated by the process being tested.

Table 13: Definition of pre-selection regions and corresponding tested physics processes. MET trigger requirement, event cleaning described Sec. 1, $n_J \geq 2$ and $E_T^{\text{miss}} > 250$ are applied as common selection.

Region name	$n_{\ell, \text{base.}}$	$n_{\ell, \text{sig.}}$	$p_T(\ell_1) [\text{GeV}]$	$nBJet$	Tested processes
1L (hardLep/softLep)	1	1	$> 35 / [7(6), 35]$ for $e (\mu)$	-	$W + \text{jets}, t\bar{t}$
1LBT (hardLep/softLep)	1	1	$> 35 / [7(6), 35]$ for $e (\mu)$	[1, 2]	$t\bar{t}$
1LBV (hardLep/softLep)	1	1	$> 35 / [7(6), 35]$ for $e (\mu)$	0	$W + \text{jets}$
1L3B	1	1	> 15	≥ 3	$t\bar{t} + cc/bb, t\bar{t} + b_{\text{fake}}$
2LBT	2	2	-	[1, 2]	$t\bar{t}$

6.2.1 $W + \text{jets}$

Fig. 1 show the kinematic distribution of the 1-lepton b-vetoed pre-selection region (1LBV) where $W + \text{jets}$ is enriched. While the bulk phase space is well-described by MC, there are a striking tendency of overestimation in the tail. Discrepancy is mainly found in distributions of n_J and variables that are scaled with respect to transverse momenta of outgoing particles such as jet transverse momentum or m_{eff} etc.

Given that the jets here are all from ISR/FSR, the mis-modeling implies the issues in high-order effects that are not fully attributed by MC. In fact, the mis-modeling is found to be well-characterized by jet multiplicity which is naively the order number of the high-order effects. For instance, a linear reweighting in n_J :

$$y_W = 1 - 0.07 \times n_J \quad (10)$$

turns to resolve not only the slope in n_J , but also the other discrepancies as well. Fig. 1 are the data-MC comparison after the reweighting. While this tendency is largely phase space independent, the optimum reweighting function (10) is not necessarily universal. For this reason, this reweighting is not seriously taken as correction, instead used for emulating the mis-modeling when validating the data-driven background estimation methods later.

In contrast, variables that do not scale with transverse momenta of outgoing particles, such as m_T or Aplanarity, keep relatively well-modeled up to the tails. This statement seems more or less valid under tighter selections in m_{eff} etc. as shown in Fig. 1. These variables are promising to use in extrapolation from control regions to signal regions.

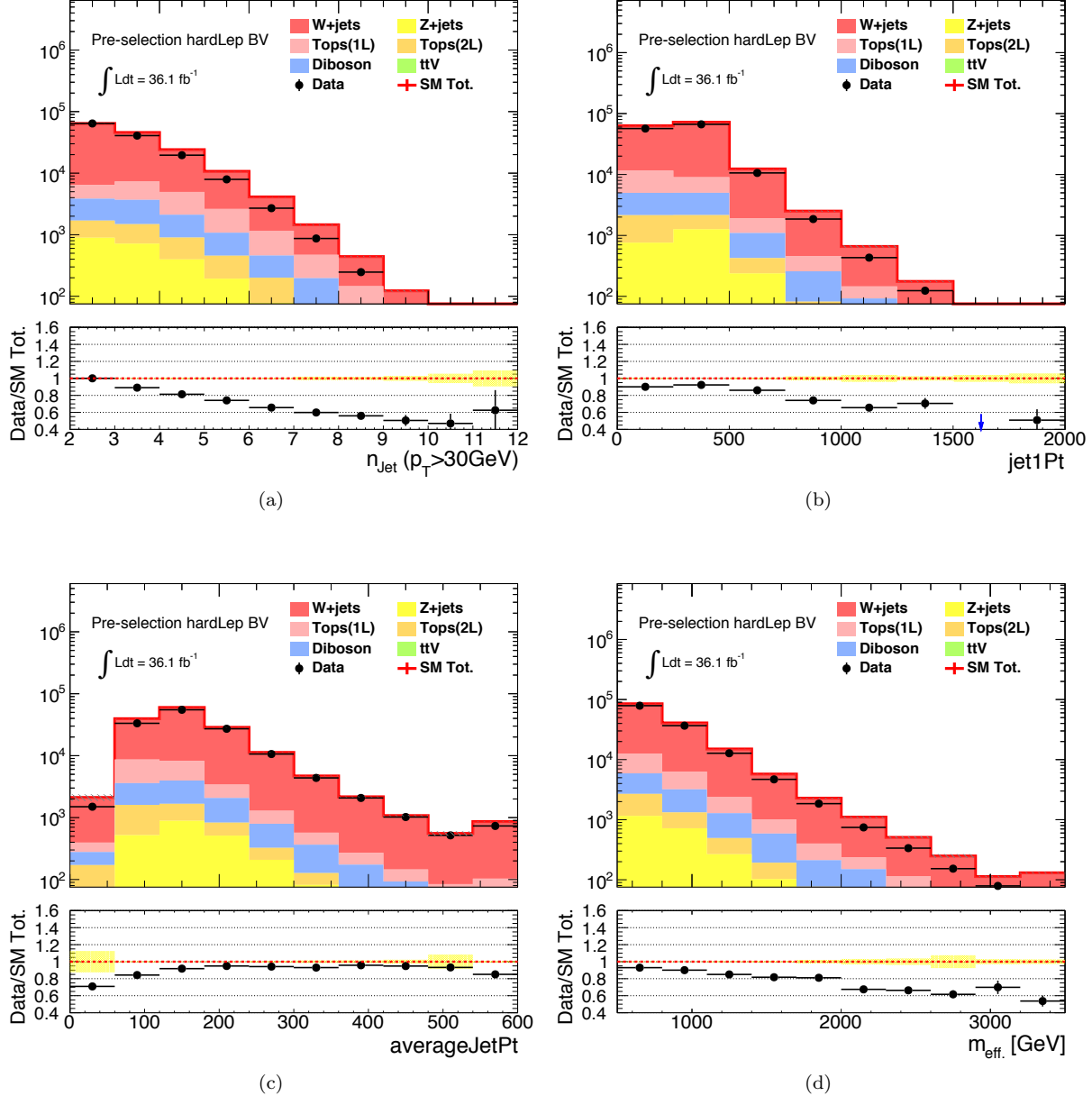


Figure 36: Kinematical distribution of (a) Jet multiplicity ($p_T > 30\text{GeV}$) (b) leading-jet pt (c) average jet pt ($p_T > 30\text{GeV}$) (d) m_{eff} in the hard lepton b-vetoed pre-selection region.

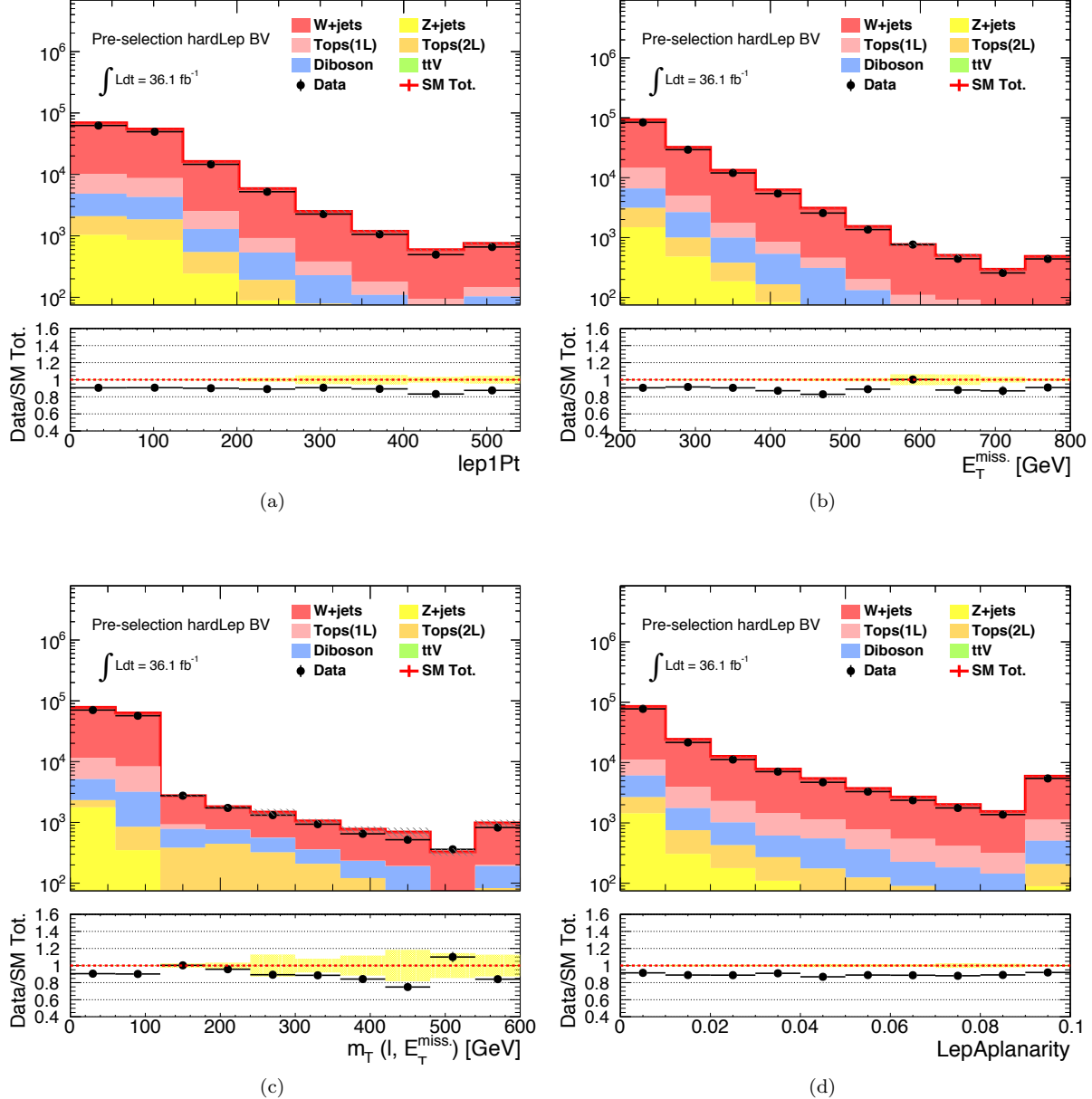


Figure 37: Kinematical distribution of (a) leading-lepton pt (b) E_T^{miss} (c) m_T (d) Aplanarity in the hard lepton b-vetoed pre-selection region.

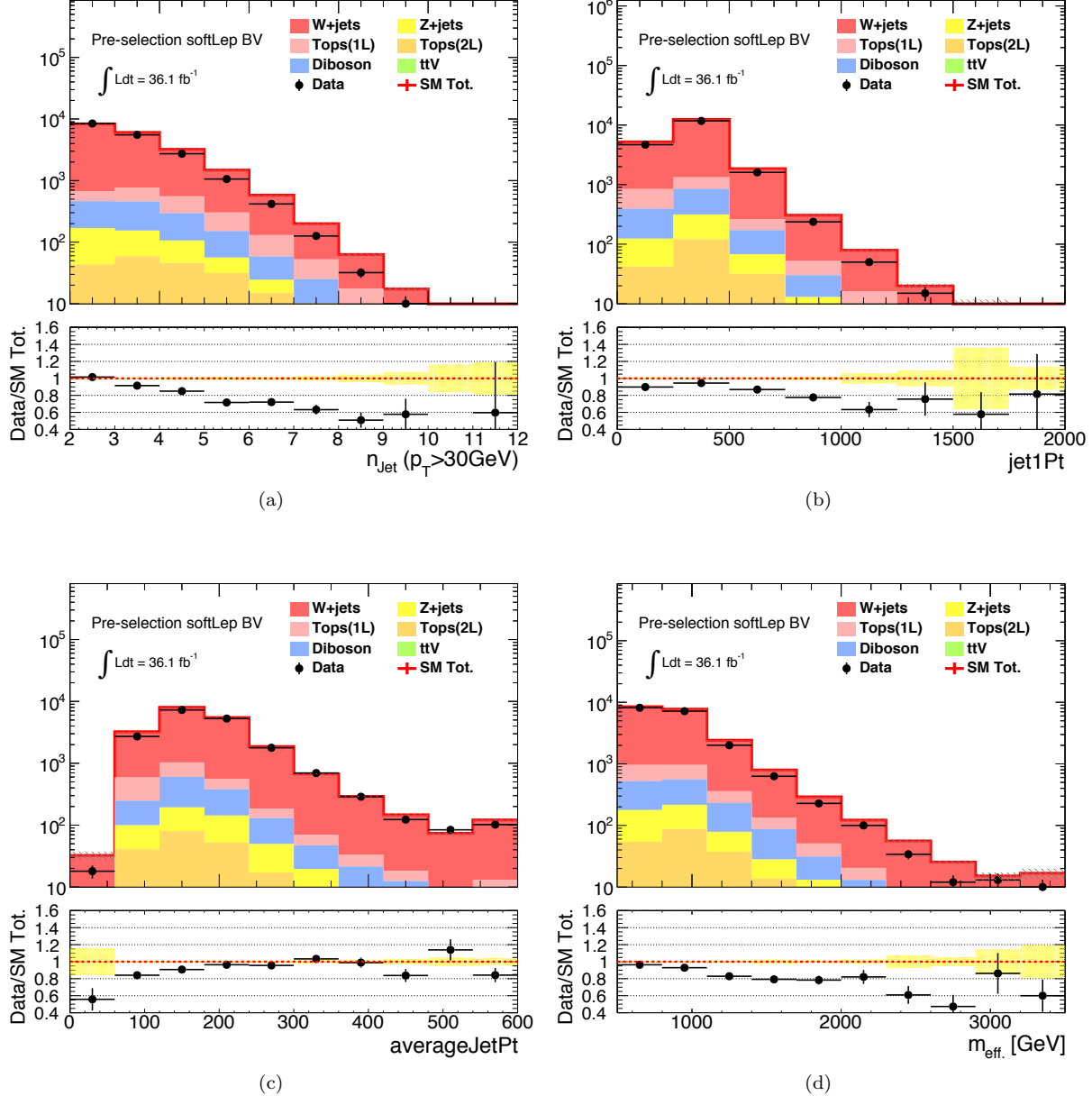


Figure 38: Kinematical distribution of (a) Jet multiplicity ($p_T > 30\text{GeV}$) (b) leading-jet pt (c) average jet pt ($p_T > 30\text{GeV}$) (d) m_{eff} in the soft lepton b-vetoed pre-selection region.

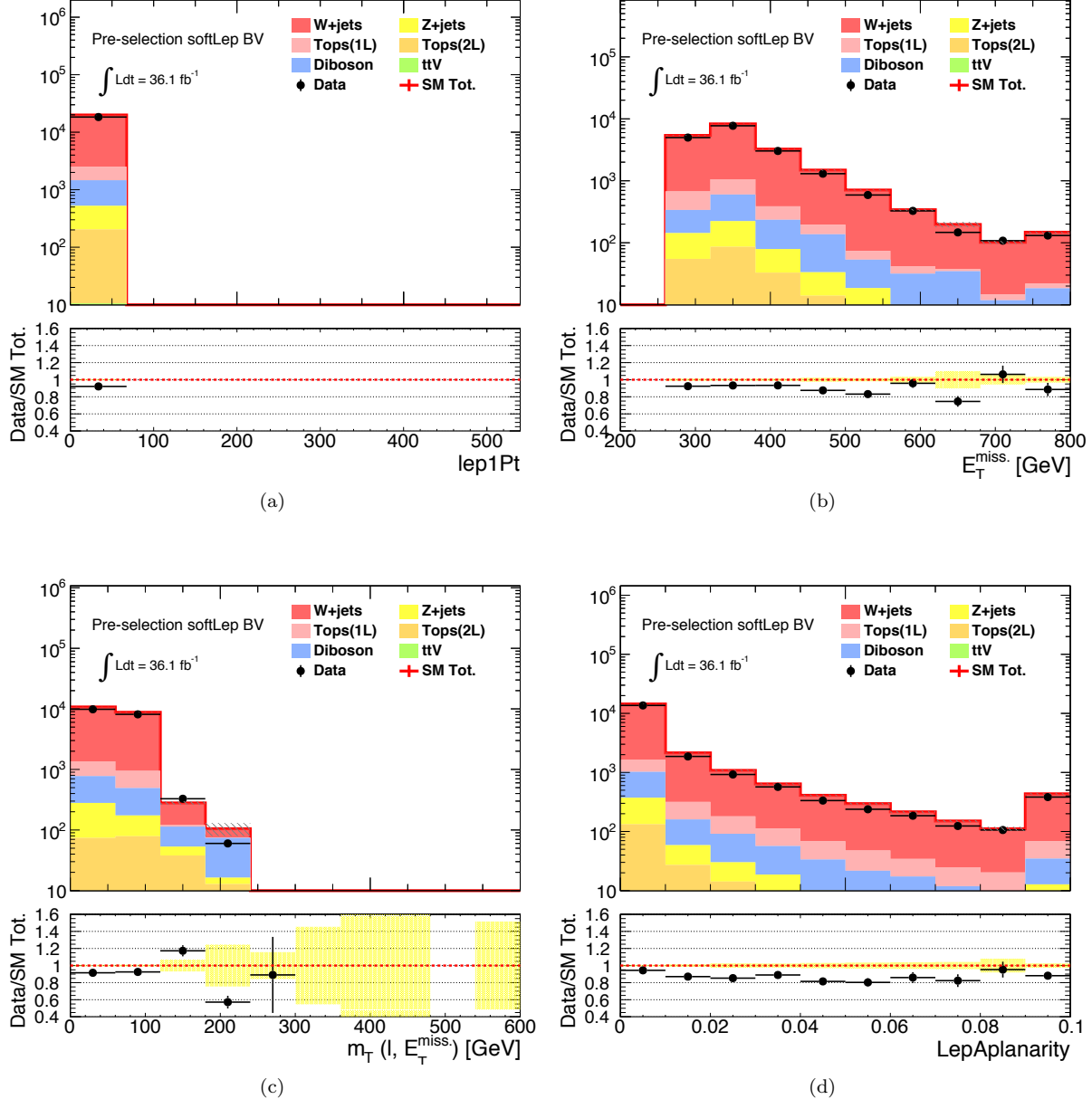


Figure 39: Kinematical distribution of (a) leading-lepton pt (b) E_T^{miss} (c) m_T (d) Aplanarity in the soft lepton b-vetoed pre-selection region.

6.2.2 Tops

Fig. 1 are the kinematic distribution of the 1-lepton b-tagged pre-selection region (1LBT) dominated by $t\bar{t}$. Similar to $W + \text{jets}$, a tendency that MC is overshooting with increasing jet activities is observed. Although $t\bar{t}$ does have 2-4 jets in its tree-level decay, contribution from additional jets becomes drastically significant in regions with high jet p_T or m_{eff} . Therefore The cause of mis-modeling is widely discussed and many explanatory effects have been proposed including QCD-NNLO [1], EW-NLO [2] and the effect of top mass width [3] and so on.

In contrast to the case in $W + \text{jets}$, $t\bar{t}$ seems to be affected by the mis-modeling in hard radiation $p_T(t\bar{t})$ is found to characterize the mis-modeling the best.

A reweighting function:

$$y_W = 1.0 - 0.064 \times p_T(t\bar{t})$$

is obtained by

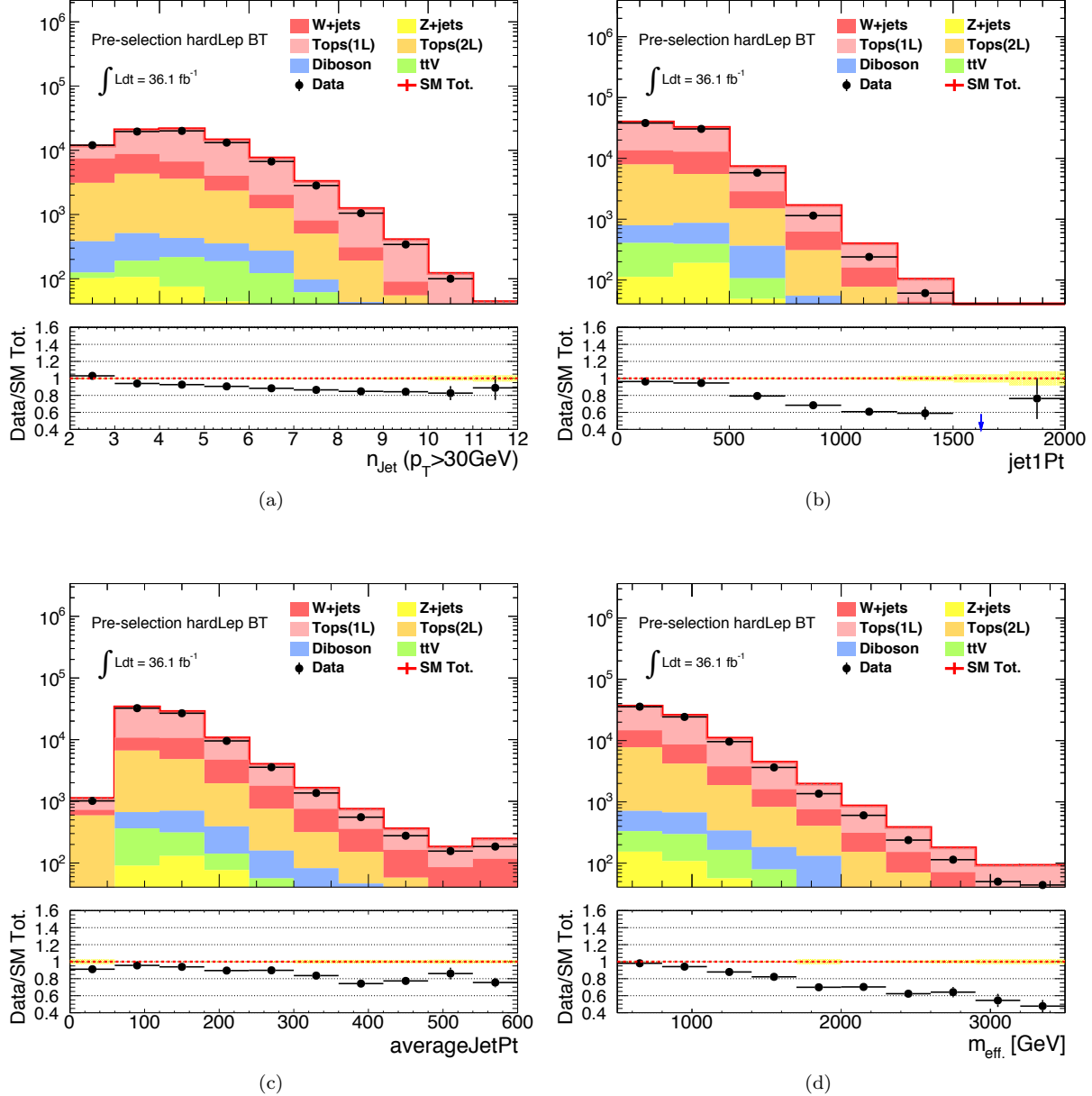


Figure 40: Kinematical distribution of (a) Jet multiplicity ($p_T > 30\text{ GeV}$) (b) leading-jet p_T (c) average jet p_T ($p_T > 30\text{ GeV}$) (d) m_{eff} in the hard lepton b-tagged pre-selection region.

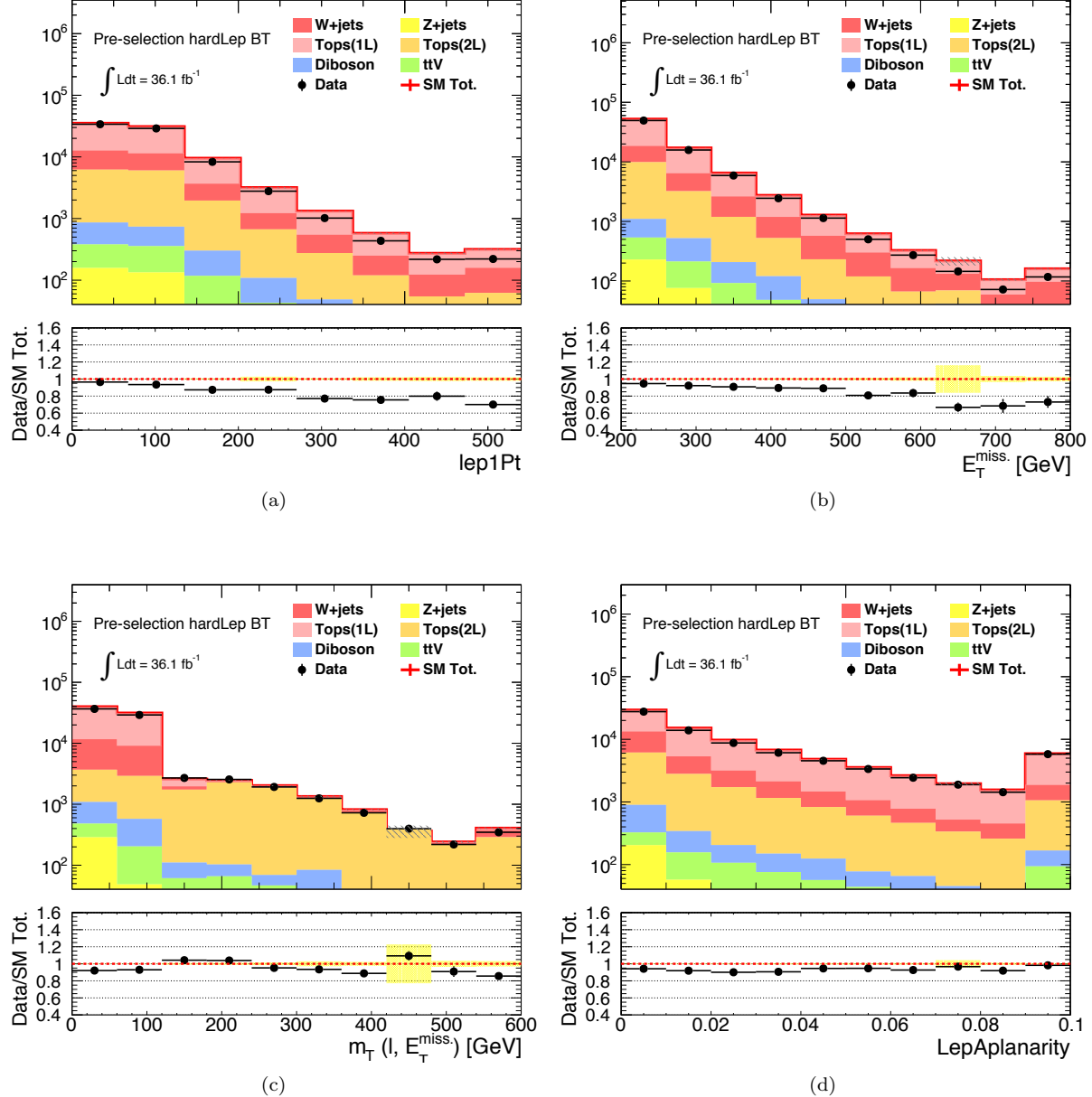


Figure 41: Kinematical distribution of (a) leading-lepton p_T (b) E_T^{miss} (c) m_T (d) Aplanarity in the hard lepton b-tagged pre-selection region.

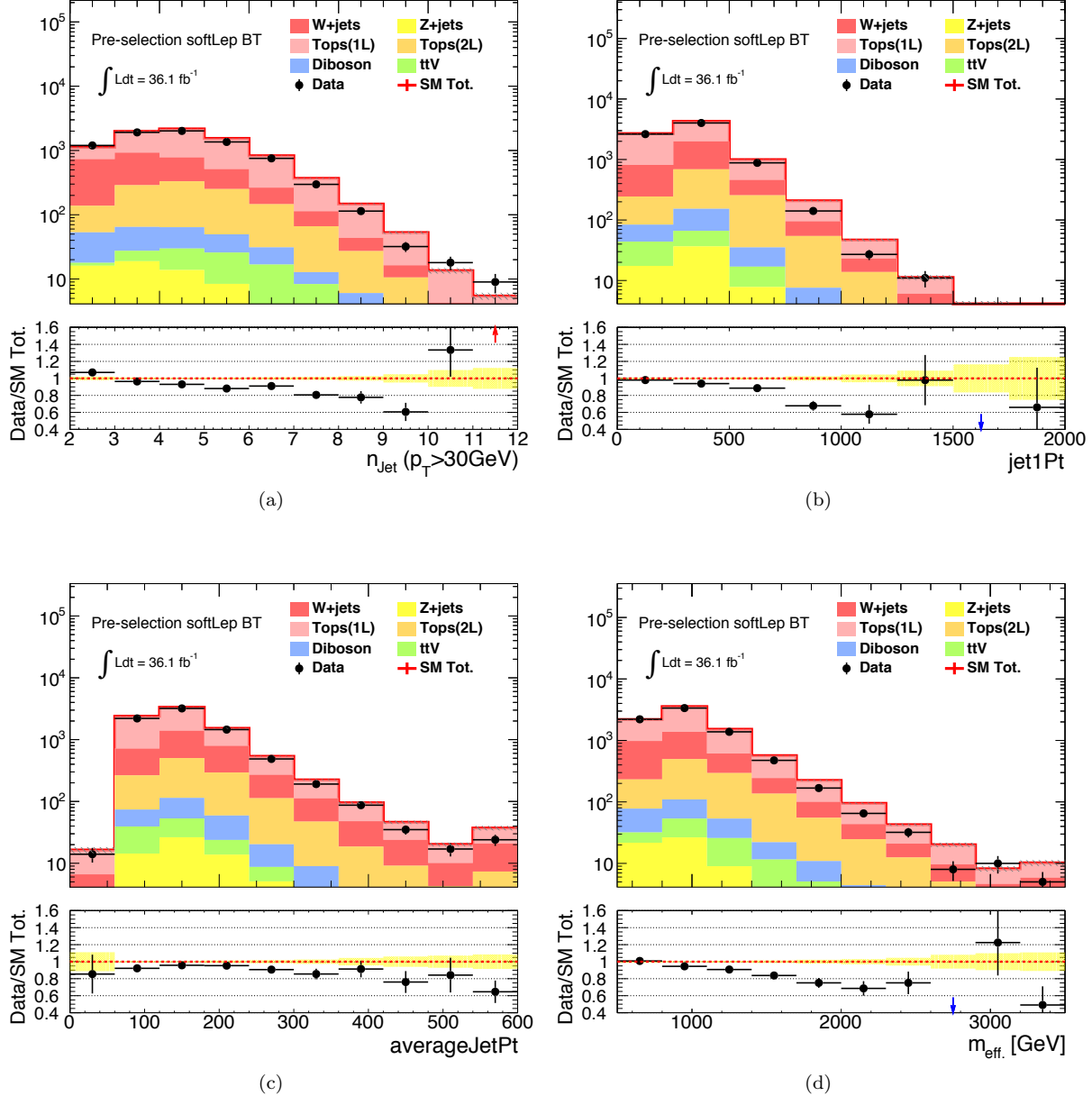


Figure 42: Kinematical distribution of (a) Jet multiplicity ($p_T > 30\text{GeV}$) (b) leading-jet pt (c) average jet pt ($p_T > 30\text{GeV}$) (d) m_{eff} in the soft lepton b-tagged pre-selection region.

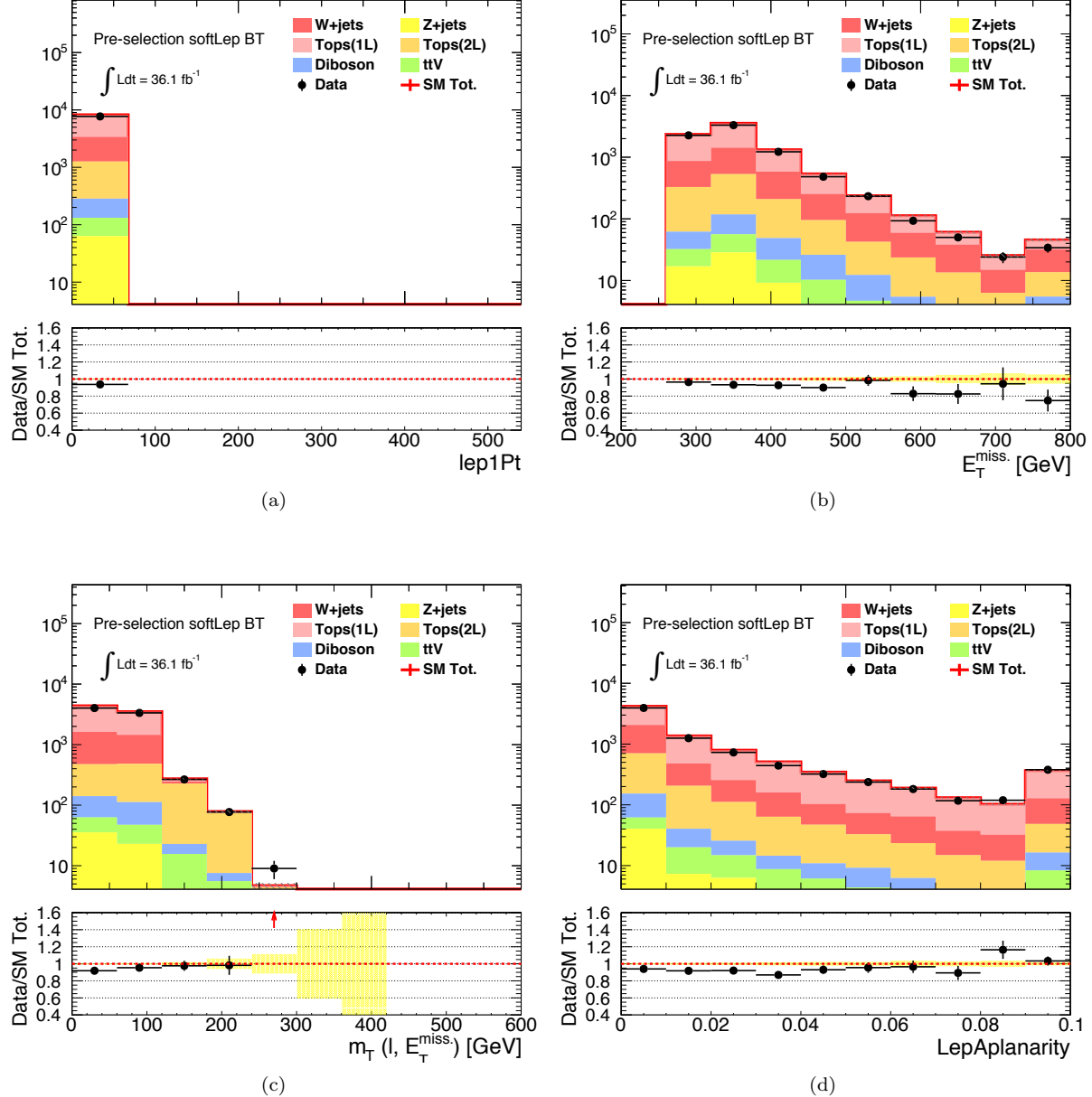


Figure 43: Kinematical distribution of (a) leading-lepton pt (b) E_T^{miss} (c) m_T (d) Aplanarity in the soft lepton b-tagged pre-selection region.

Di-leptonic pre-selection region is also available for testing the $t\bar{t}$ modeling. The reweighting function is still perfectly valid indicating the issue is in the hard process description rather than instrumental affairs.

3b preselection Modeling of $tt + cc/bb$ and $t\bar{t} + b_{fake}$ are exclusively examined using a region with 3 or more b-jets (1L3B). While the shapes seem to be affected by the same type of mis-modeling as observed in inclusive $t\bar{t}$ selection above, the normalization is also underestimated by about 20%.

many sources and effects conflicts hard to nail down the effects the discuss the reliability of MC due to the scarce data statistics

fortunately 3B SRs are dominated by di-leptonic components, they can be estimated by a full-data driven object replacement method,

the dependence on MC can be minimized.

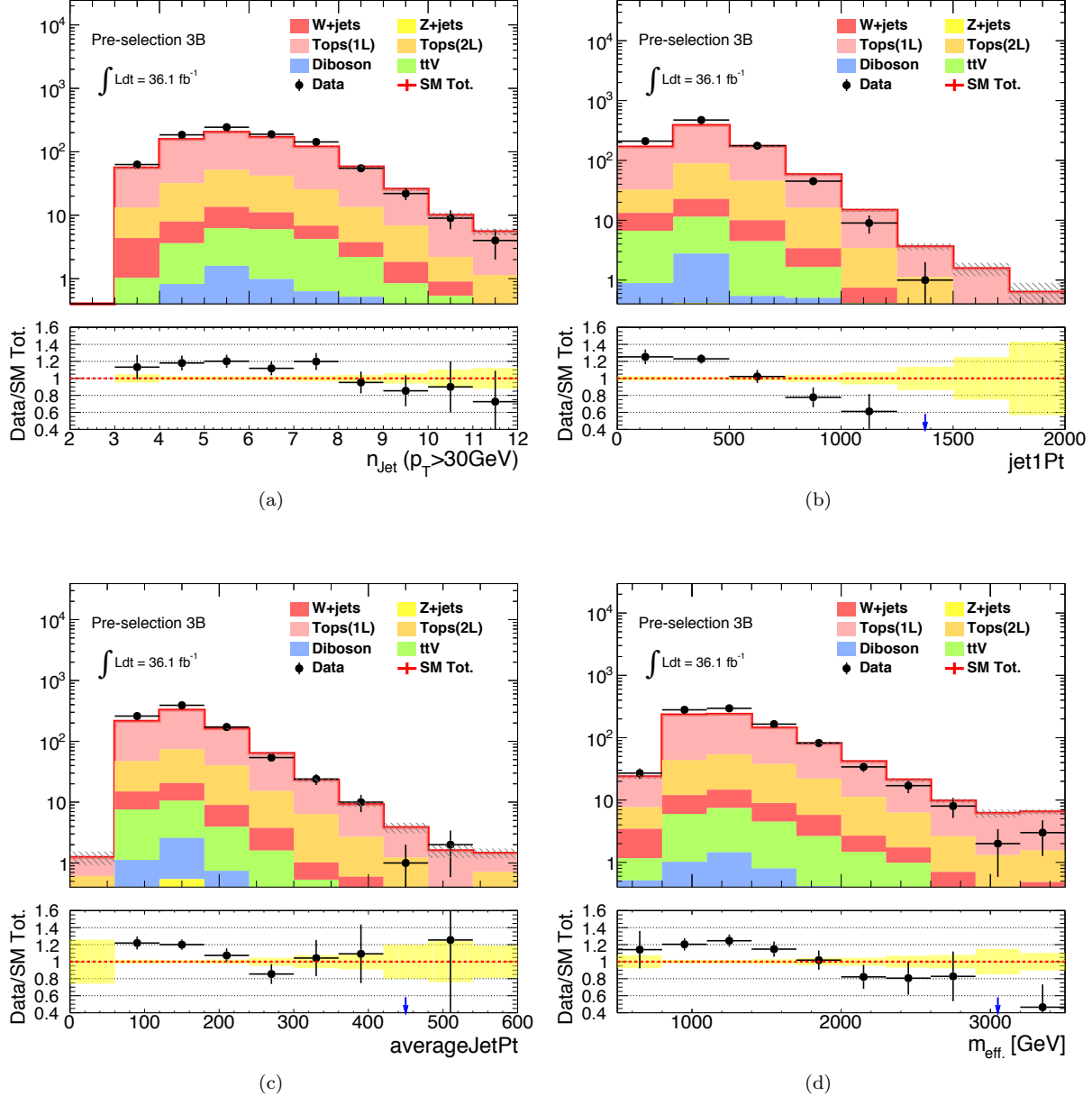


Figure 44: Kinematical distribution of (a) Jet multiplicity ($p_T > 30 \text{ GeV}$) (b) leading-jet pt (c) average jet pt ($p_T > 30 \text{ GeV}$) (d) m_{eff} in the 3b-tagged pre-selection region.

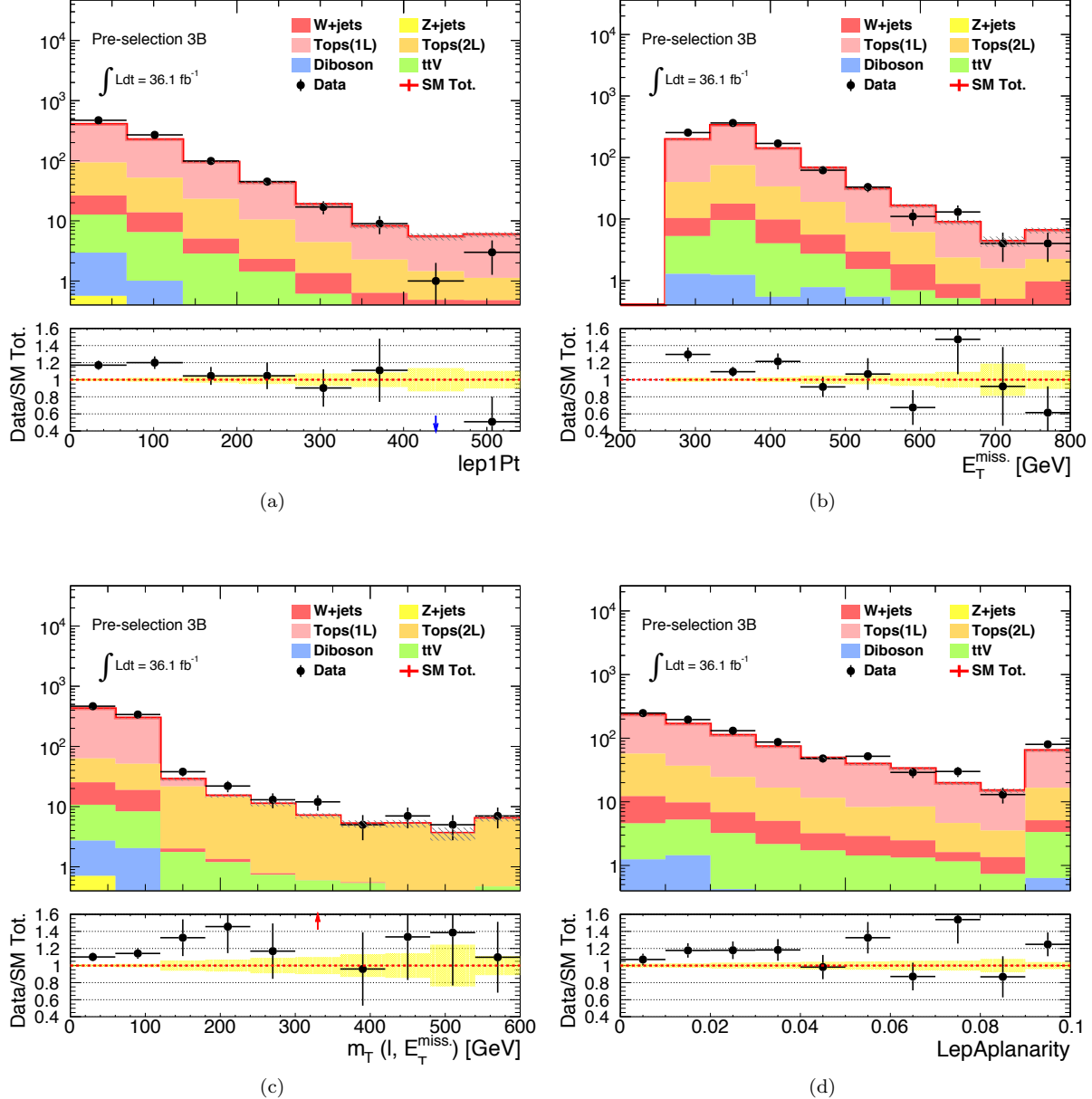


Figure 45: Kinematical distribution of (a) leading-lepton pt (b) E_T^{miss} (c) m_T (d) Aplanarity in the 3b-tagged pre-selection region.

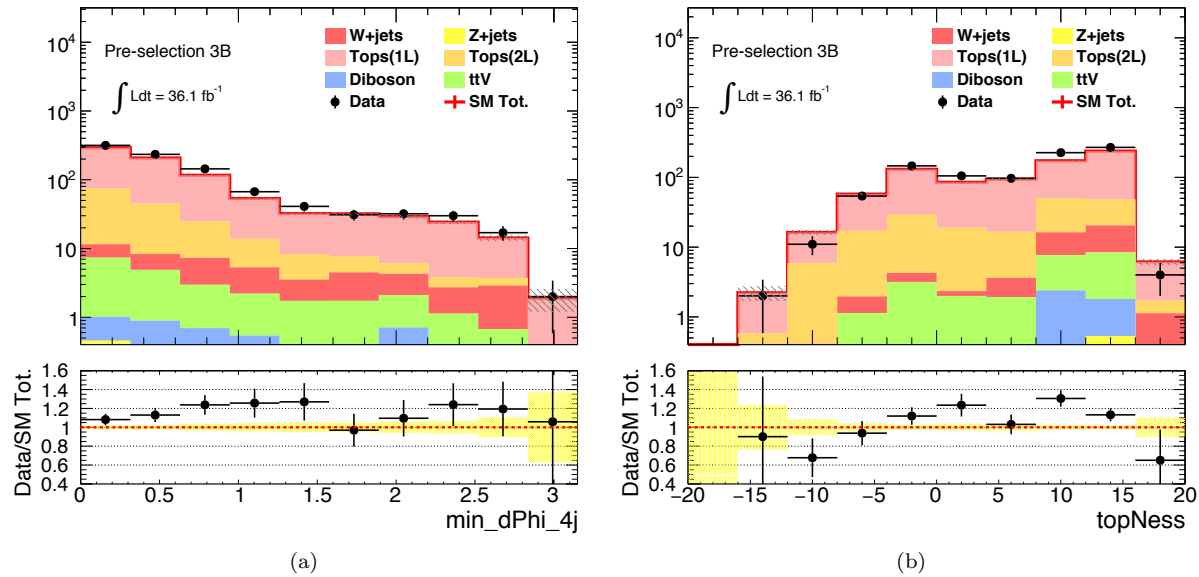


Figure 46: Kinematical distribution of (a) $\min_{i=1-4} \Delta\phi(j_i, E_T^{\text{miss}})$ (b) Topness in the 3b-tagged pre-selection region.

6.3 The Kinematical Extrapolation Method

6.3.1 Definition of Control Regions and Validation Regions

One of the solution to this MC mis-modeling is to apply correction. The simplest way is to define “control region” (CR) and normalize the MC to the data there. The key assumption is that both CR and SR suffer from the same mis-modeling, so that the normalization factor measured in CR is applicable to SR as well. Therefore, the most important requirement in CR definition is having the similar phase space with respect to corresponding SR.

The easiest realization of CR is to revert the SR cuts in kinematical variables that are well-modeled by MC. m_T and Aplanarity are chosen as the baseline extrapolation variables in this analysis. One exception is the “2J” tower where Aplanarity is not used in SR cuts. E_T^{miss} is used instead as the modeling is still acceptable, thank to the fact that the ISR/FSR contribution is relatively low in those regions. We never touch the cuts in n_J ($p_T > 30\text{GeV}$) and m_{eff} .

Minor modifications are needed following several considerations; CR statistics are sufficient. Selections is loosened in some of the CRs. E_T^{miss} is relatively ok rather than jet pts since it is the vectoral sum of them thus the impact on its absolute scale is canceled to some extent.; low- m_T regions should be cut out to avoid potential contribution from QCD multi-jets. The resultant CRs are summarized in Tab. 1 for respective towers.

The normalization is applied only on $W + \text{jets}$, $t\bar{t}$ and single-top while raw MC prediction is quoted for diboson and the other minor backgrounds. $t\bar{t}$ and single-top shares the normalization factors as their relative breakdown is similar in CRs and SRs.

Validation regions are aimed to confirm the validity of the background estimation procedure by comparing with the data, located in between the CRs and SRs as defined in Tab. 1. VRa and VRb respectively validates the extrapolation in m_T and Aplanarity (E_T^{miss} for “2J”). The relations with CRs and SRs are visualized in Fig. 1. VRs-QCD are the regions to confirm the negligible contribution from “QCD” components in SRs. The detail is found in Sec. 6.5.

6.3.2 Result of Background-only Fit

Normalization factors are determined by a simultaneous fit on the b-vetoed and b-tagged slice of a CR, allowing the normalization factor and all the theoretical and experimental nuisance parameters to flow. The detail on the statistical procedure is described in Sec. 1. The fitting procedure is performed independently in each SR bins.

Obtained normalization factors are displayed in Fig. ??.

6.3.3 Evaluation on the Non-closure

A potential concern over the kinematical extrapolation method is that it still fully relies on MC in the extrapolation. Although the MC modeling of chosen extrapolation variables are confirmed in various regions, it is not trivial when the exact selection of SRs are applied, particularly in a situation where the cause of MC mis-modeling is not fully understood.

The extrapolation error is evaluated quantitatively by generating an artificial mis-modeling and test the response of the extrapolation. Fig. 1 are the cases where n_J ($p_T > 30\text{GeV}$) and m_{eff}

For more realistic emulation of mis-modeling, reweighting based on Eq. 1 and 1 are used for $W + \text{jets}$ and $t\bar{t}$ respectively. Fig. 1 shows the results.

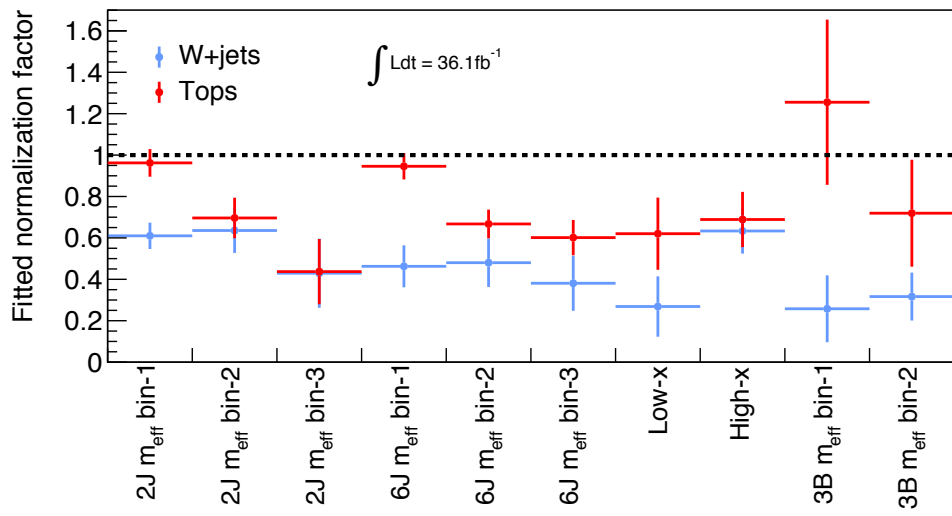


Figure 47: Summary of fitted normalization factors.

Observed non-closure is generally small, staying within 15% (10%) for $W + \text{jets}$ ($t\bar{t}$) in the most messimistic case. This non-closure is quoted as systematics error associated with the method in the fit.

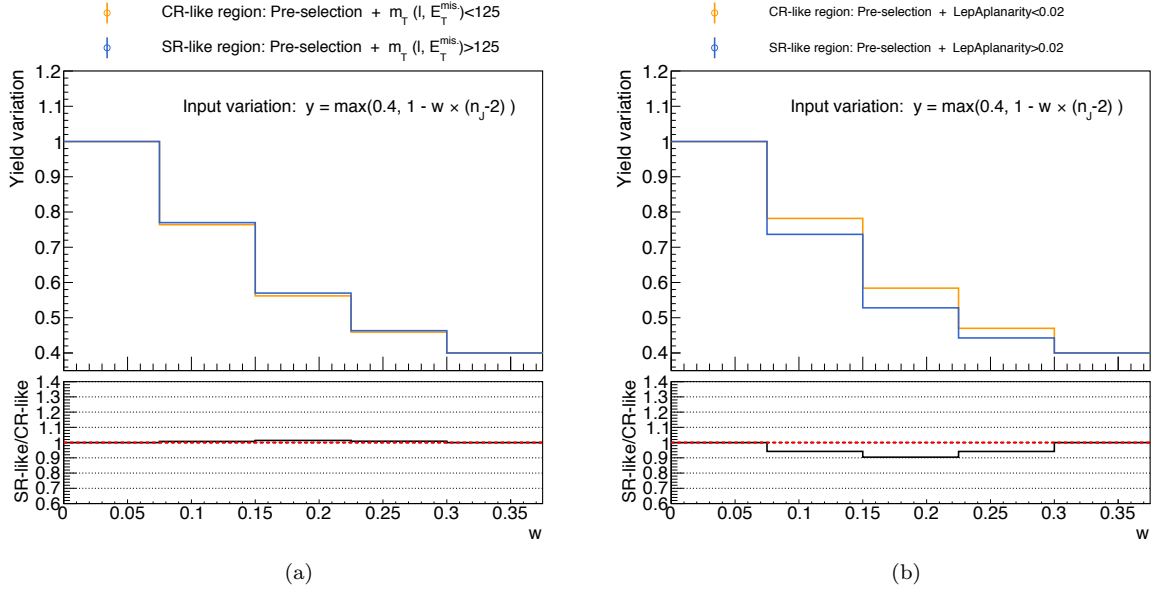


Figure 48: Closure error for $W + \text{jets}$ process by the extrapolation using (a) m_T (b) Aplanarity as function of the magnitude of injected linear mis-modelling on n_J ($p_T > 30\text{GeV}$): $y_{t\bar{t}} = 1.0 - x \times n_J$ ($p_T > 30\text{GeV}$)). All evaluated by MC.

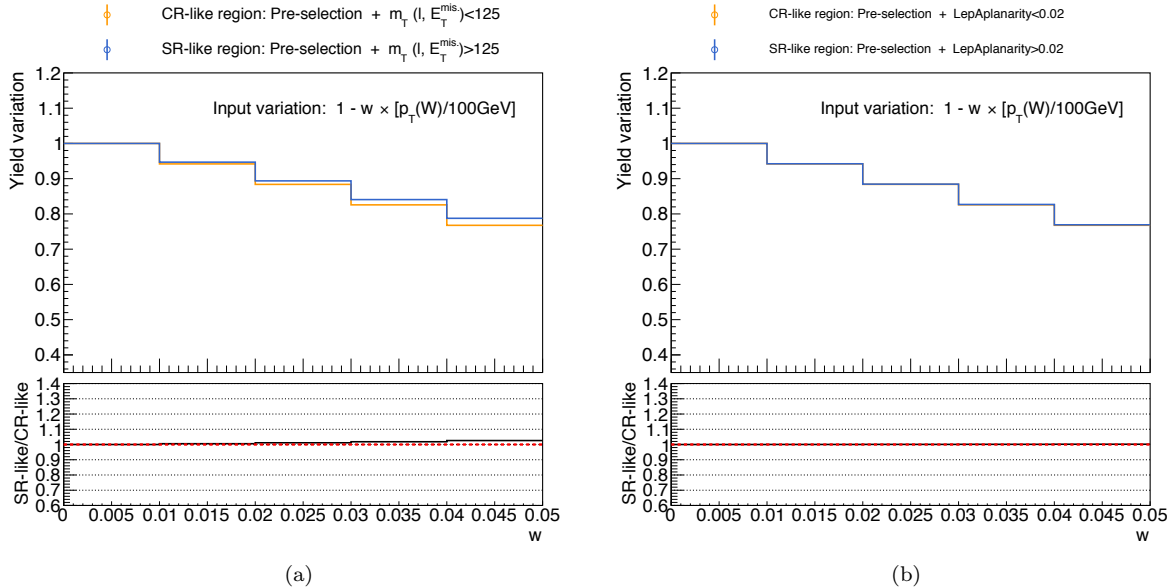


Figure 49: Closure error for $W + \text{jets}$ process by the extrapolation using (a) m_T (b) Aplanarity as function of the magnitude of injected linear mis-modelling on n_J ($p_T > 30\text{GeV}$): $y_{t\bar{t}} = 1.0 - x \times n_J$ ($p_T > 30\text{GeV}$)). All evaluated by MC.

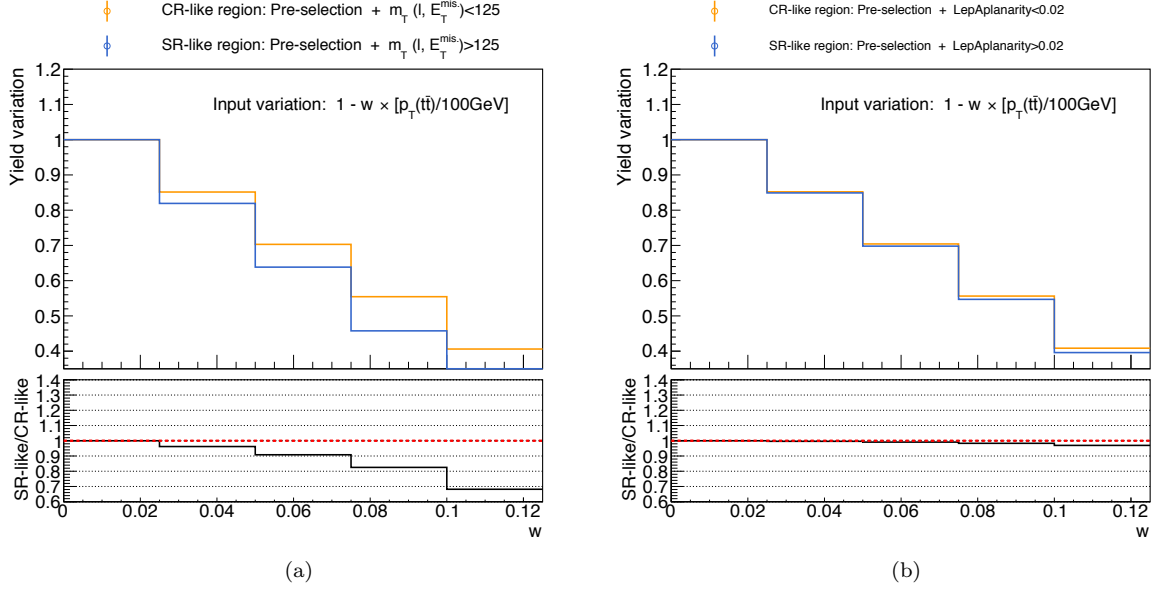


Figure 50: Closure error for $t\bar{t}$ process by the extrapolation using (a) m_T (b) Aplanarity as function of the magnitude of injected linear mis-modelling on $p_T(t\bar{t})$: $y_{t\bar{t}} = 1.0 - x \times p_T(t\bar{t})$. All evaluated by MC.

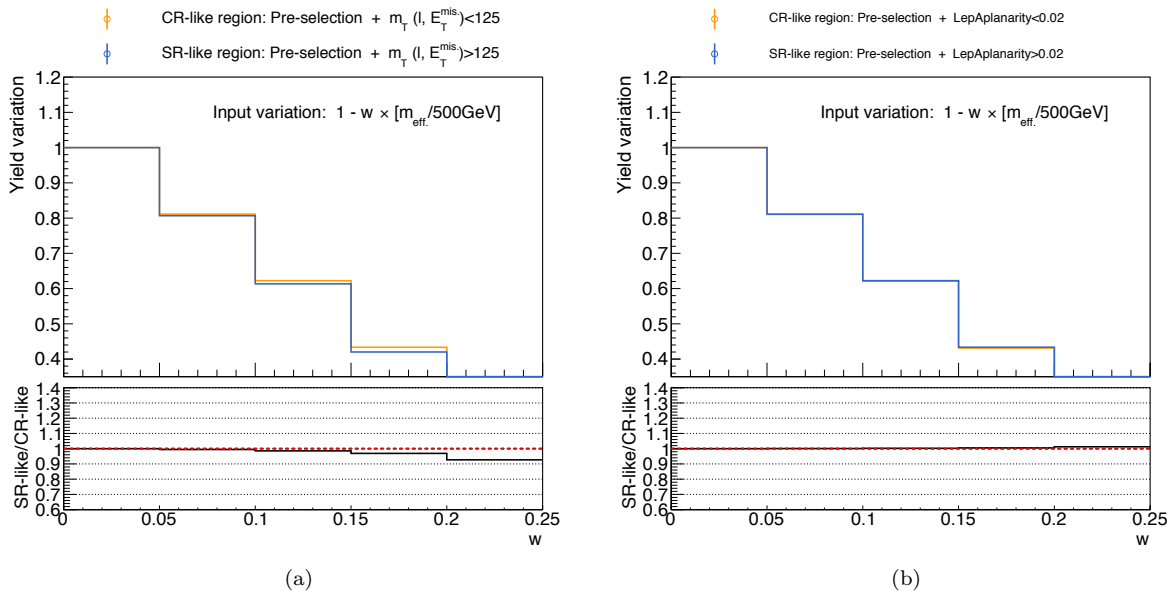


Figure 51: Closure error for $t\bar{t}$ process by the extrapolation using (a) m_T (b) Aplanarity as function of the magnitude of injected linear mis-modelling on $m_{\text{eff.}}^{\text{Inc}}$: $y_{t\bar{t}} = 1.0 - x \times m_{\text{eff.}}$. All evaluated by MC.

6.4 The Object Replacement Method

Although m_T seems to be a robust variable for extrapolation,

Kinematical extrapolation is not necessarily robust in estimating the di-leptonic component since the

Use of di-leptonic control regions is naturally motivated to control “2L” backgrounds.

The object replacement method is an integrated method consisting of:

- ”missing lepton replacement” to estimate part of $\ell\ell_{\text{mis}}$ events (“Mis. Reco.” and ”Mis. ID”),
- ”tau replacement” to estimate $\ell\tau_h$

using the extrapolation from a control region with exactly 2 baseline leptons (2LCR). It replaces one of the lepton of data events in 2LCR into a virtual missing lepton or a simulated hadronic tau decay so that they emulate the kinematics of the signal regions.

The underlying assumptions are that **1) kinematics of hard processes does not depend on object selection** and that **2) MC is well-modeling about object response and tau decays**. As the usage of MC is only limited in area related to objects, kinematics of the hard process can be fully taken from data. This is the most notable advantage for this method that the risk of introducing unknown uncertainty will be drastically reduced compared with the nominal method in which extrapolation is done with kinematics. While philosophically this method can provide more accurate prediction than the nominal method, it suffers from several practical drawbacks:

- The range of application is rather limited. Components such as semileptonic processes ($W+jets$ etc.) or some of the missing lepton events (“Out Acc.” and ”Mis. OR”) are not supported by this method.
- Uncertainty is typically comparable or larger than that of the nominal method under typical signal region selections due to limited CR statistics, although it can be improved just by adding data statistics.

6.4.1 Per-event Procedure

Fig 52 and 54 outline the basic procedure for missing lepton replacement and tau replacement, which is as follow:

1. Pick up a 2LCR event (“seed event”).
2. Replace a lepton of the seed event into a virtual missing lepton or a simulated hadronic decay of tau lepton, if the other lepton (“tag lepton”) satisfies the signal lepton requirement (and trigger matching). This replaced event is called ”sub-event”.
3. Recalculate the event-level kinematical variables (e.g. E_T^{miss} , m_{eff} etc.).
4. Assign a weight κ for each sub-event as the transfer factor from 2LCR to 1L regions.
5. Change the roles (tagged/replaced) between the two leptons and repeat 2-4. Generated sub-events are filled in a single “event-level histogram”.
6. (for tau replacement) Repeat 2-5 by 50 times in order to fully account for the kinematical pattern by tau decays which differs decay-be-decay.

7. Assign 100% error for each bin of the event-level histogram, accounting for all the sub-events are generated from the common seed event.
8. Loop over all seed event and sum up all the event-level histograms.

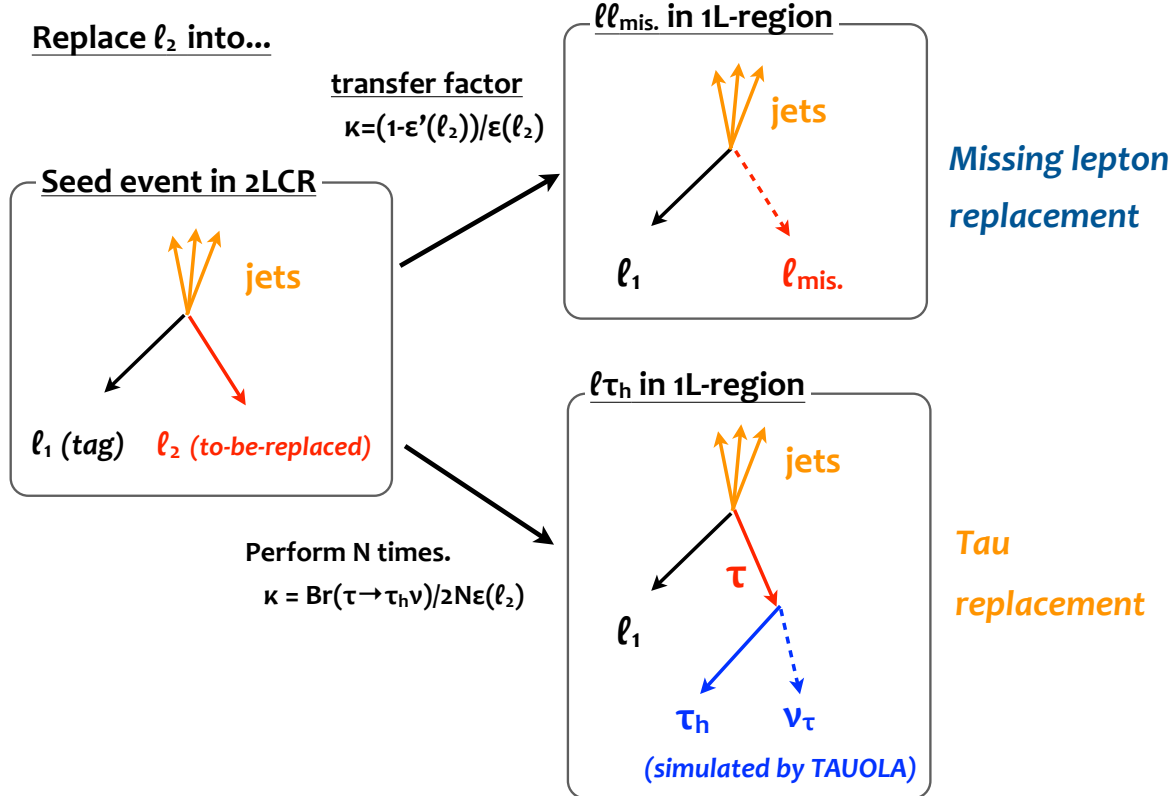


Figure 52: Schematic of the object replacement method.

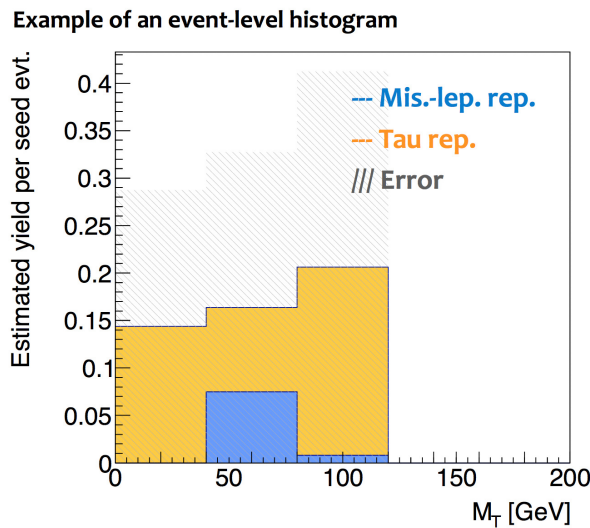


Figure 53: An example of event-level histogram. 100% uncertainty is assigned for each bin to account for the fact that all the entries are from the same seed. Final estimation is given by the sum of the event-level histograms over all seed events.

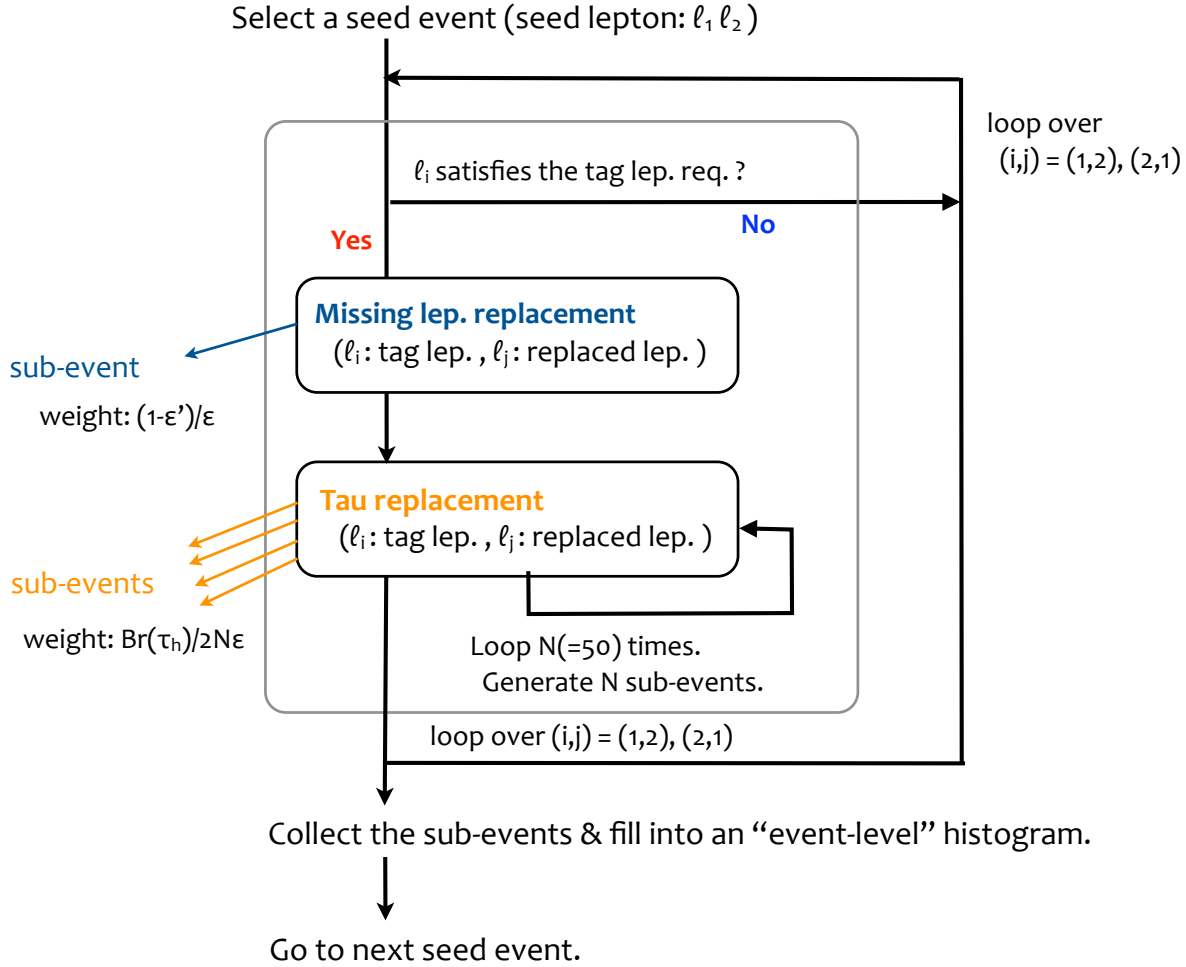


Figure 54: Flow chart of actions per seed event.

More detail and caveats about each step are as following:

Seed event selection and trigger

For seed event selection, looser kinematical selection is in general preferred to cover the full phase space to be estimated, within an acceptable level of contamination from irrelevant BGs (Z+jets, W+fakes etc.). In particular MET selection has to be loosened to at least around $E_T^{miss} > 100\text{GeV}$ to fully account for the hard lepton signal regions where typically MET is required above $200 \sim 250\text{GeV}$. The single-lepton trigger is used to trigger such seed events, and the inverse efficiency (fig. ??) is applied event-by-event to accommodate the different triggers in use with respect to the analysis. In contrast, seed events are triggered by the MET trigger in estimating soft lepton signal regions (“2J”) as the tag lepton is not sufficiently hard to fire the single-lepton trigger. Thanks to the fact that the MET requirement in 2J is much higher ($E_T^{miss} > 430\text{GeV}$), $E_T^{miss} > 200\text{GeV}$ for seed selection is still affordable. To summarize, 2LCR is defined by the OR of two orthogonal regions (2LCRa and 2LCRb) as tab.14.

Tag lepton requirement

As the tag lepton is equivalent to the lepton used in the analysis in 1L regions, it has to satisfy the signal

Table 14: Definition of 2LCR.

2LCRa	$n_\ell(\text{baseline}) = 2, n_\ell(\text{signal}) \geq 1$ $p_T(\ell_1) > 35\text{GeV}, \eta(\ell) < 2.5,$ At least one lepton fires the single-lepton trigger $\cancel{E}_T > 100\text{GeV}, n_J \geq 3$
-------	---

lepton requirement (as well as $p_T > 30\text{GeV}$ and the trigger matching in case of estimating hard lepton regions).

Treatment of virtual missing lepton

As electrons are reconstructed as jets as well in most cases, electrons failing reconstruction or ID will be recognized as jets in this analysis. Therefore in the missing lepton replacement, if there is at least one reconstructed jet overlapped with the electron to be replaced by $\Delta R < 0.4$, the electron will be replaced into the closest jet, otherwise into a missing particle inheriting the momentum of original electron. Missing muons will be usually not identified as any objects. However they are still counted in the MET track soft term in some occasion. Since the criteria are complicated and also keeps evolving all the time, we ignore it for the moment and simply treat all missing lepton as missing particles. The impact might not be negligible for missing muon estimation, but given the very high efficiency of muon reconstruction and ID, the impact on final estimation should be limited.

Simulation of tau decays

Tau decays are simulated by TAUOLA [?] assuming the taus are unpolarized. This assumption is incorrect given the parent W-bosons are left-handed, but the impact on the final result is studied (see below chapter) and found to be marginal. Branching for leptonic decay is set to zero to reduce the number of loops.

Given that the analysis is tau-agnostic, hadronic taus within p_T - η acceptance are reconstructed and recognized as full-calibrated anti-Kt4 jets once they pass the JVT cut. On the other hand, the output of TAUOLA is merely a 4-vector of truth level hadronic tau. Therefore following treatments are applied for the truth-level hadronic taus to emulate observables.

1. Apply the scale of anti-Kt4 jets for truth hadronic taus.

Due to the fact that the anti-Kt4 jet have larger cone and contain more underlying tracks inside, the measured energy will be systematically higher than the truth when a hadronic tau is measured as an anti-Kt4 jet. To emulate the effect, a scale is applied for truth hadronic taus output from TAUOLA.

2. Smear the p_T of hadronic tau.

To account for the resolution of measurement, a simple Gaussian smearing is applied for p_T of hadronic taus after correcting the scale.

These scale and resolution are derived from $t\bar{t}$ MC by comparing the p_T of truth hadronic taus and that of ΔR -matched reconstructed jet by $\Delta R < 0.2$, as a function of p_T and η of truth hadronic taus (fig.??, ??).

3. Emulate signal jet identification / b-tagging

Hadronic taus with $p_T > 30\text{GeV}$, $|\eta| < 2.8$ are selected as the signal jet candidates. Signal jets are then randomly identified from them, based on the efficiency of JVT cut. A random b-tagging is further performed on the signal jets, by assigning a random b-tagging score (MV2c10) following according to the profile. The JVT cut efficiency and profile of b-tagging score are obtained by $t\bar{t}$ MC using jets matched with truth hadronic taus by $\Delta R < 0.2$. JVT cut efficiency is parameterized as a function of p_T and η of signal jet candidates (fig.??), while the b-tagging score profile is separately derived by tau decay modes (fig.??).

Transfer factor

A weight κ is assigned on each sub-event to account for the different probability of occurrence between the seed event and the replaced sub-event. For instance in the missing lepton replacement, this corresponds to the efficiency ($\epsilon_{\text{baseline}}(\ell_{\text{rep.}})$) and inefficiency ($1 - \epsilon_{\text{Reco.+ID}}(\ell_{\text{rep.}})$) of offline lepton selection for the replaced lepton. The ratio

$$\kappa = \frac{1 - \epsilon_{\text{Reco.+ID}}(\ell_{\text{rep.}})}{\epsilon_{\text{baseline}}(\ell_{\text{rep.}})}$$

has to be applied to get the correct normalization of estimation.

As for the tau replacement, the transfer factor is

$$\kappa = \frac{\text{Br}(\tau \rightarrow \tau_h \nu)}{2N\epsilon_{\text{baseline}}(\ell_{\text{rep.}})}$$

, where N is number of iteration per replacement which is currently set to 50 (N merely defines the level of “smoothing” thus has no essential impact on the final result). The factor 2 reflects the fact that two channels ($e\ell$ and $\mu\ell$) are available as seeds.

 $1/\kappa$ roughly indicates the ratio of statistics between CR and SR. Given that the sub-events of missing lepton replacement and tau replacement originate from the common seed events, and that generally $\ell\tau_h$ populates much more than $\ell\ell_{\text{mis.}}$, the effective CR statistics is no more than 3 times as SR statistics. This factor of 3 gain in statistics is in fact not very sufficient as it immediately leads to $30\% \sim 50\%$ statistical error by itself in typical signal regions where only a few events are expected. Therefore CR statistic is always the biggest source of uncertainty in this method.

Lepton efficiency

Lepton efficiency used in transfer factor calculation is obtained by $t\bar{t}$ MC as a function of p_T and η of truth leptons (fig.??). The efficiency is defined as the fraction of truth leptons that are ΔR -matched with reconstructed lepton passing ID or signal lepton requirement by $\Delta R < 0.2$.

Event-level histogram and statistical treatment

 Multiple sub-events are generated by both missing lepton replacement and tau replacement from a single seed event, and filled into the same event-level histogram. To account for this full correlation, 100% error is assigned to each bin of the event-level histogram. The sum of event-level histograms over all seed events will be the desired distribution. Although the summation is not trivial since the bins of event-level histograms are not statistically independent each other, the effect of bin-to-bin correlation is supposed to be negligible considering that signal regions are single-binned or coarsely binned (much coarser than typical width of event-level histogram) in this analysis.

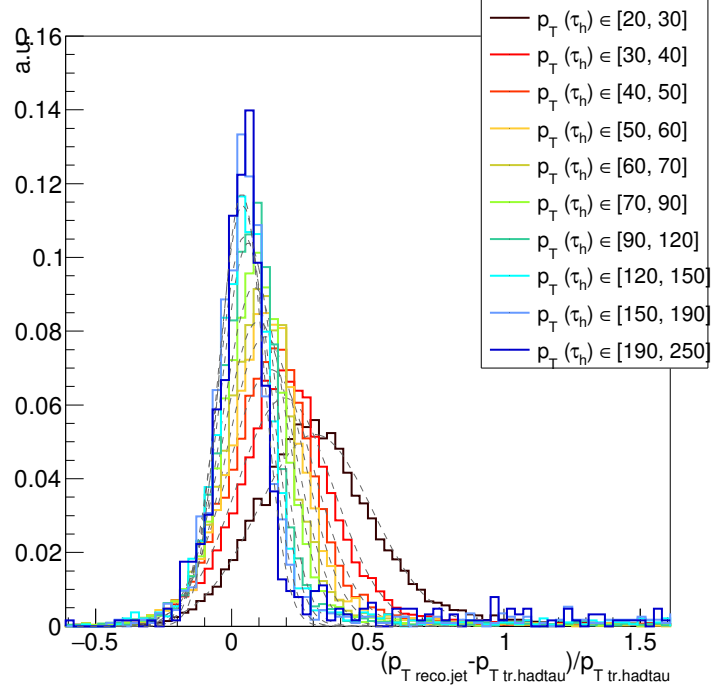


Figure 55:

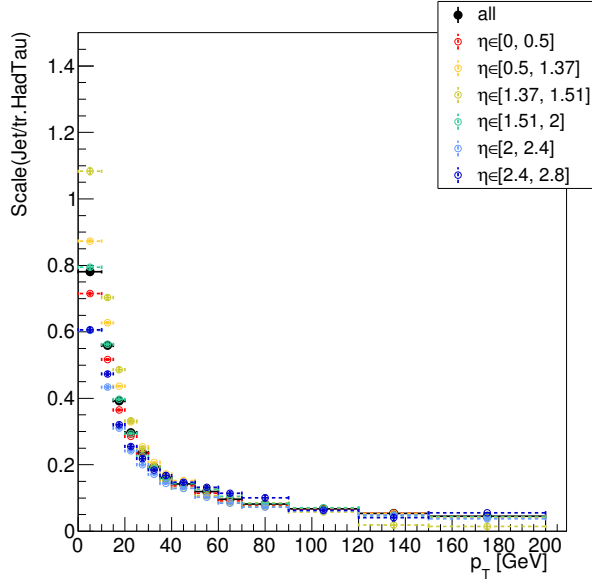


Figure 56: Scale of anti-Kt4 jets for truth hadronic taus, defined as the mean of reco. $p_T(\tau_h)/\text{truth } p_T(\tau_h) - 1$ distribution. Truth $p_T(\tau_h)$ is defined as the transverse component of $|\mathbf{p}(\tau) - \mathbf{p}(\nu_{tau})|$ while the reconstructed one is defined as the p_T of an anti-Kt4 jet ΔR -matched to it.

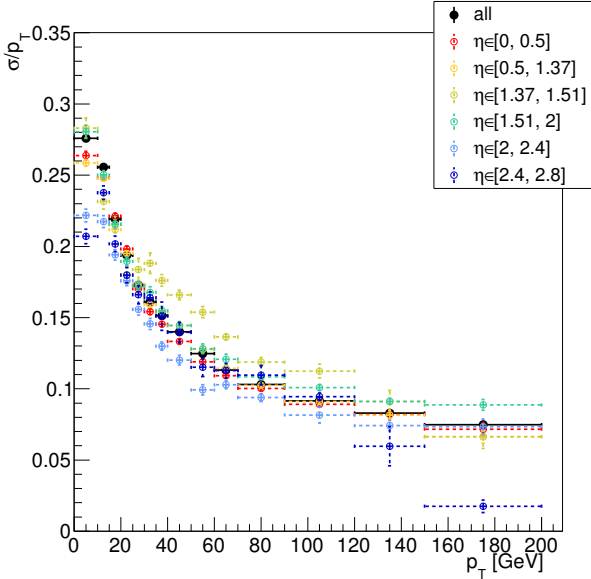


Figure 57: Resolution of hadronic tau, defined as the gaussian-fitted RMS of reco. $p_T(\tau_h)/\text{truth } p_T(\tau_h) - 1$ distribution. Reco. $p_T(\tau_h)$ is defined as the p_T of ΔR -matched anti-Kt4 jet.

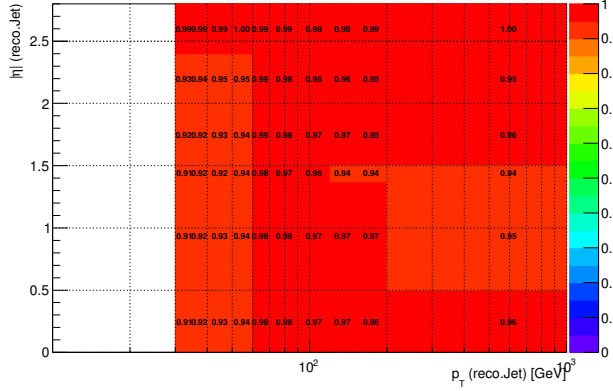


Figure 58: Fraction of signal jet candidates that pass the signal jet requirement, parametrized as function of p_T and η of reconstructed jets.

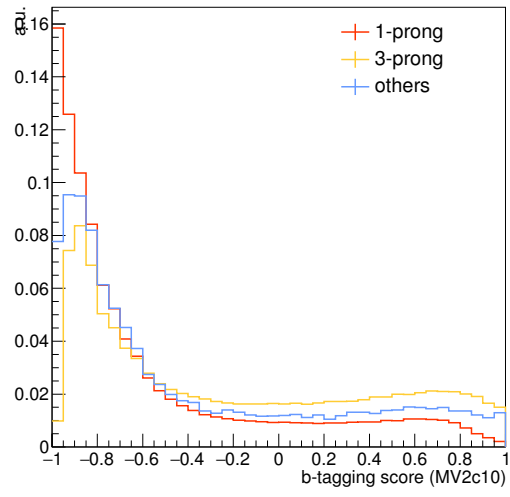


Figure 59: Profile of b-tagging score (MV2c10) for tau jets, calculated from ttbar MC.

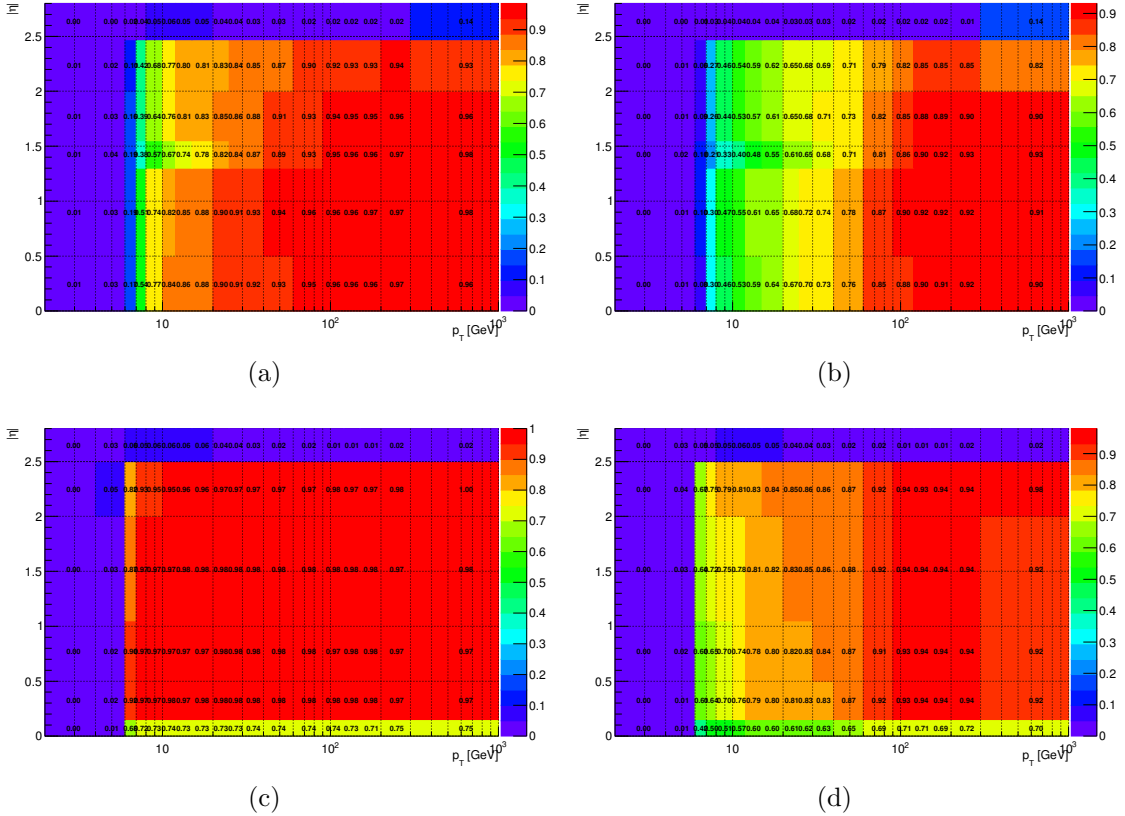


Figure 60: Off-line selection efficiency used in transfer factor calculation. (a) Efficiency of electrons passing reconstruction and ID. (b) Efficiency of electrons passing signal lepton requirement. (c) Efficiency of muons passing reconstruction and ID. (d) Efficiency of muons passing signal lepton requirement.

6.4.2 Closure Test using $t\bar{t}$ MC Samples

6.4.3 Closuer test with loose selection.

The methodologies are tested by comparing yields and distributions between the estimation by object replacement and the actual $\ell\ell_{\text{mis}}/\ell\tau_h$ events, in a region with exactly one baseline lepton (“Closure test”), using the Powheg+Pythia6 $t\bar{t}$ MC. The level of disagreement (non-closure) indicates the generic accuracy about this method, which will be quoted as systematics. Fig.61 ~ 63 show the result for the hard lepton regions and fig.64 ~ 66 are for the soft lepton regions. MET cut for the seed selection is removed for the hard lepton case in order to boost the statistics enought to test the shape. The other selections follow tab.14.

Closure is generally good. Non-closure is typically within 10% (5%), and never exceeds 30% (10%) significantly for the missing lepton replacement (the tau replacement). The closure of missing lepton replacement is generally worse than that of tau replacement, however it is not worrisome since the contribution of $\ell\ell_{\text{mis}}$ is typically $5 \sim 10$ times smaller than $\ell\tau_h$ in our signal regions.

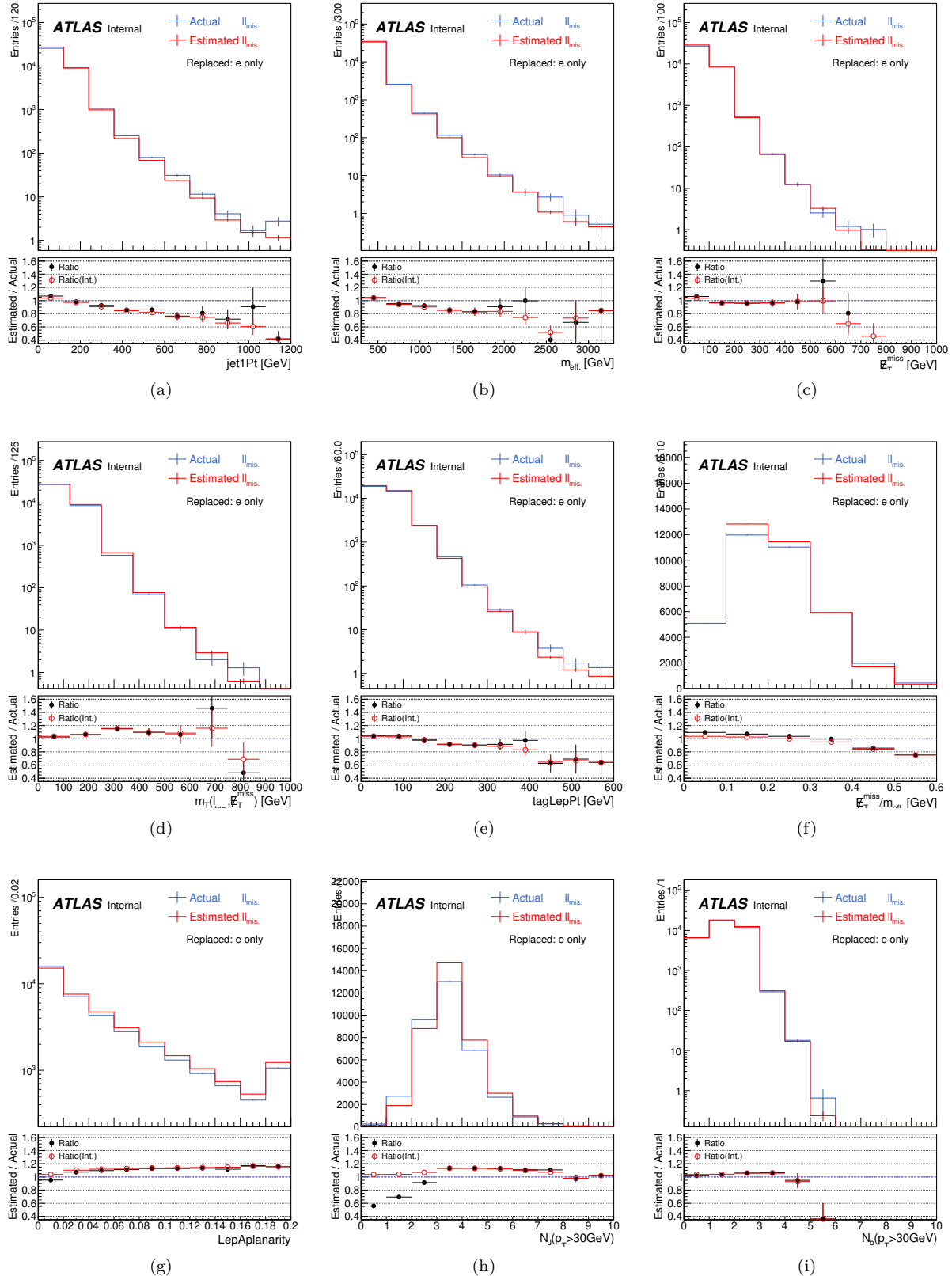


Figure 61: MC closure test for **missing lepton replacement** using di-leptonic $t\bar{t}$ sample (410009). Seed events are collected by the single-lepton trigger. $p_T > 35\text{ GeV}$ for the leading lepton is required. **Only electrons in the seed events are replaced.** All distribution are normalized with $\int L dt = 36.5 \text{ fb}^{-1}$.

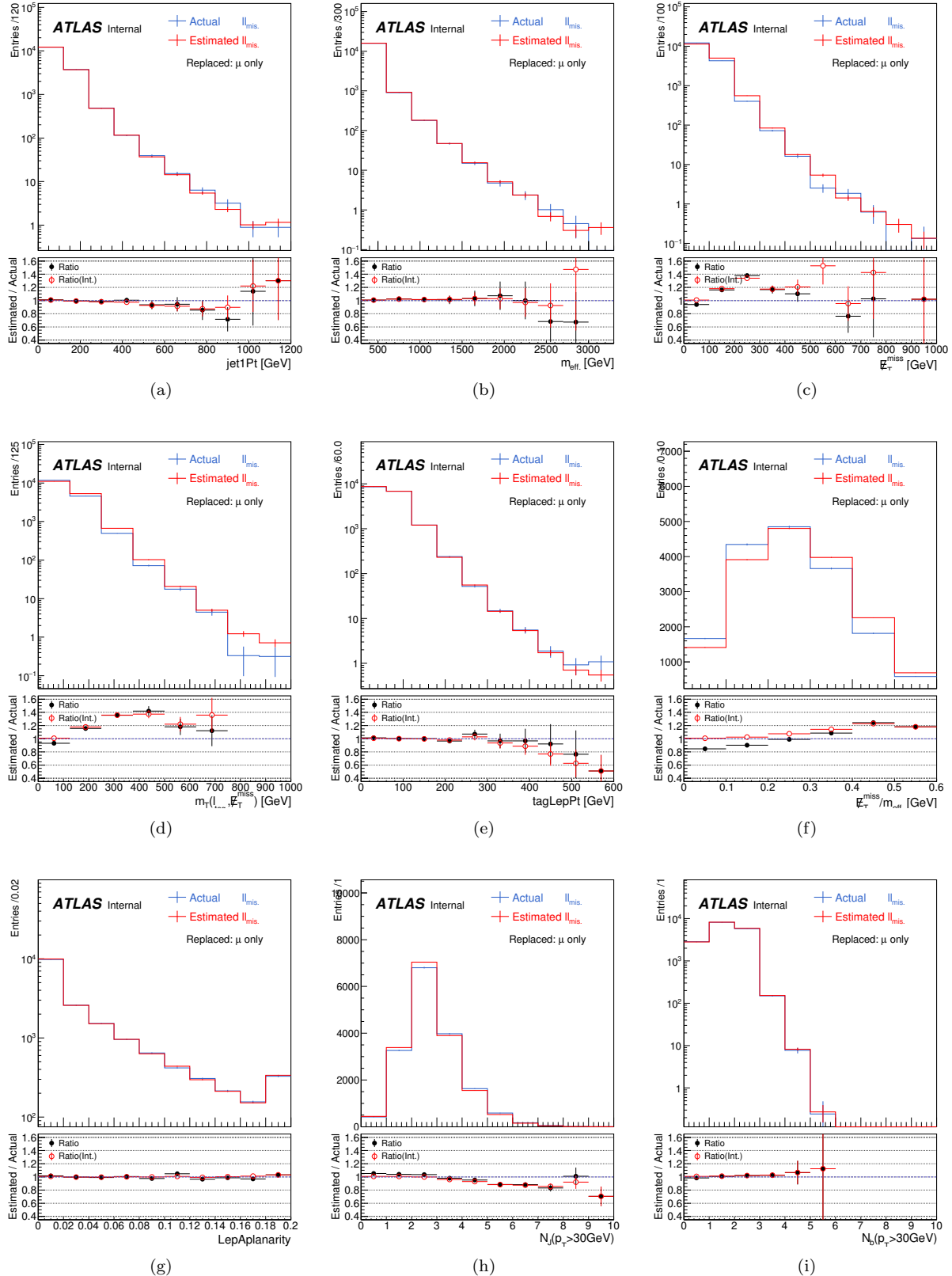


Figure 62: MC closure test for **missing lepton replacement** using di-leptonic $t\bar{t}$ sample (410009). Seed events are collected by the single-lepton trigger. $p_T > 35\text{GeV}$ for the leading lepton is required. **Only muon in the seed events are replaced.** All distribution are normalized with $\int Ldt = 36.5\text{fb}^{-1}$.

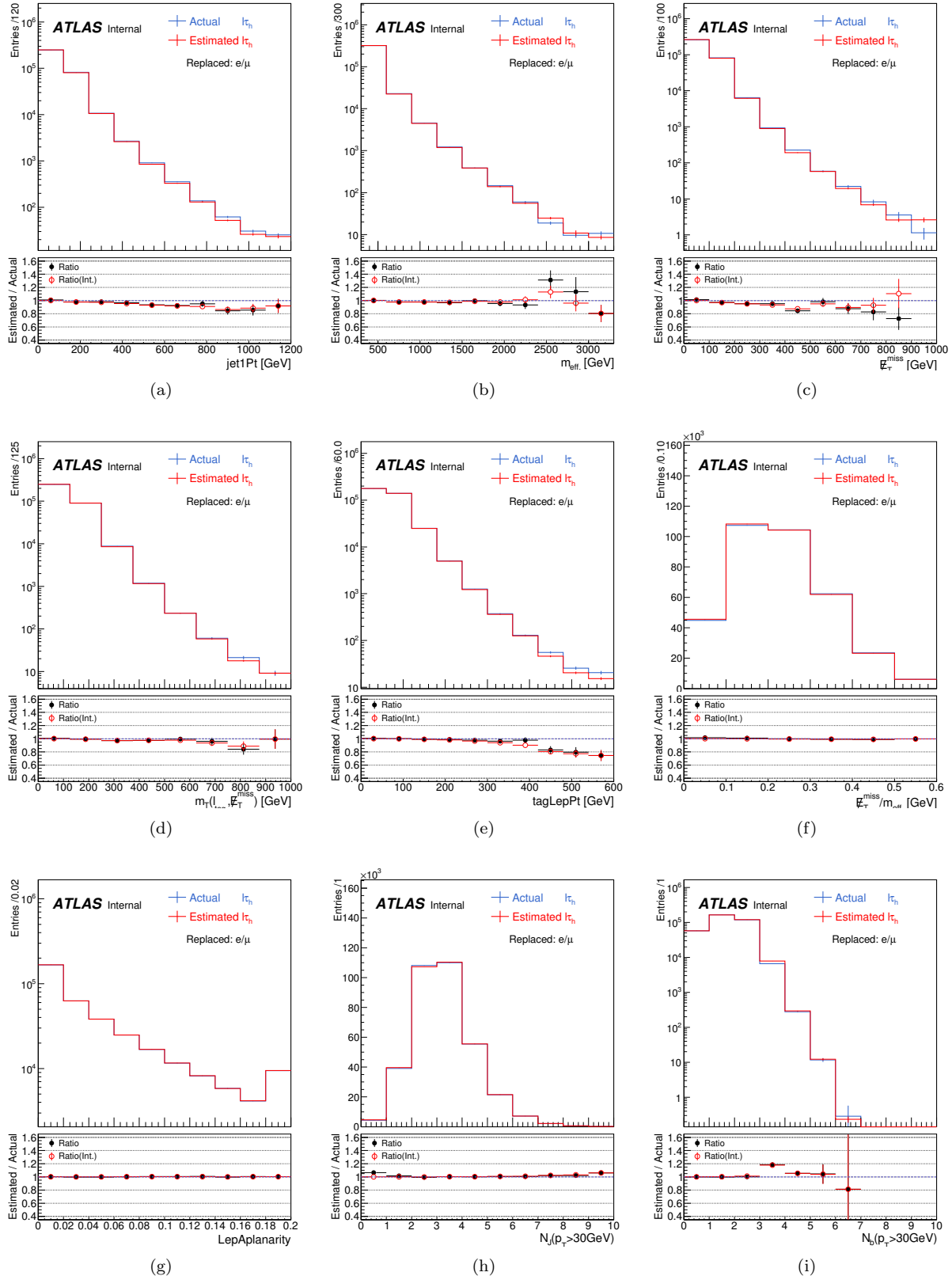


Figure 63: MC closure test for **tau replacement** using di-leptonic $t\bar{t}$ sample (410009). Seed events are collected by the single-lepton trigger. $p_T > 35\text{ GeV}$ for the leading lepton is required. **Both electrons and muons in the seed events are replaced.** All distribution are normalized with $\int L dt = 36.5\text{ fb}^{-1}$.

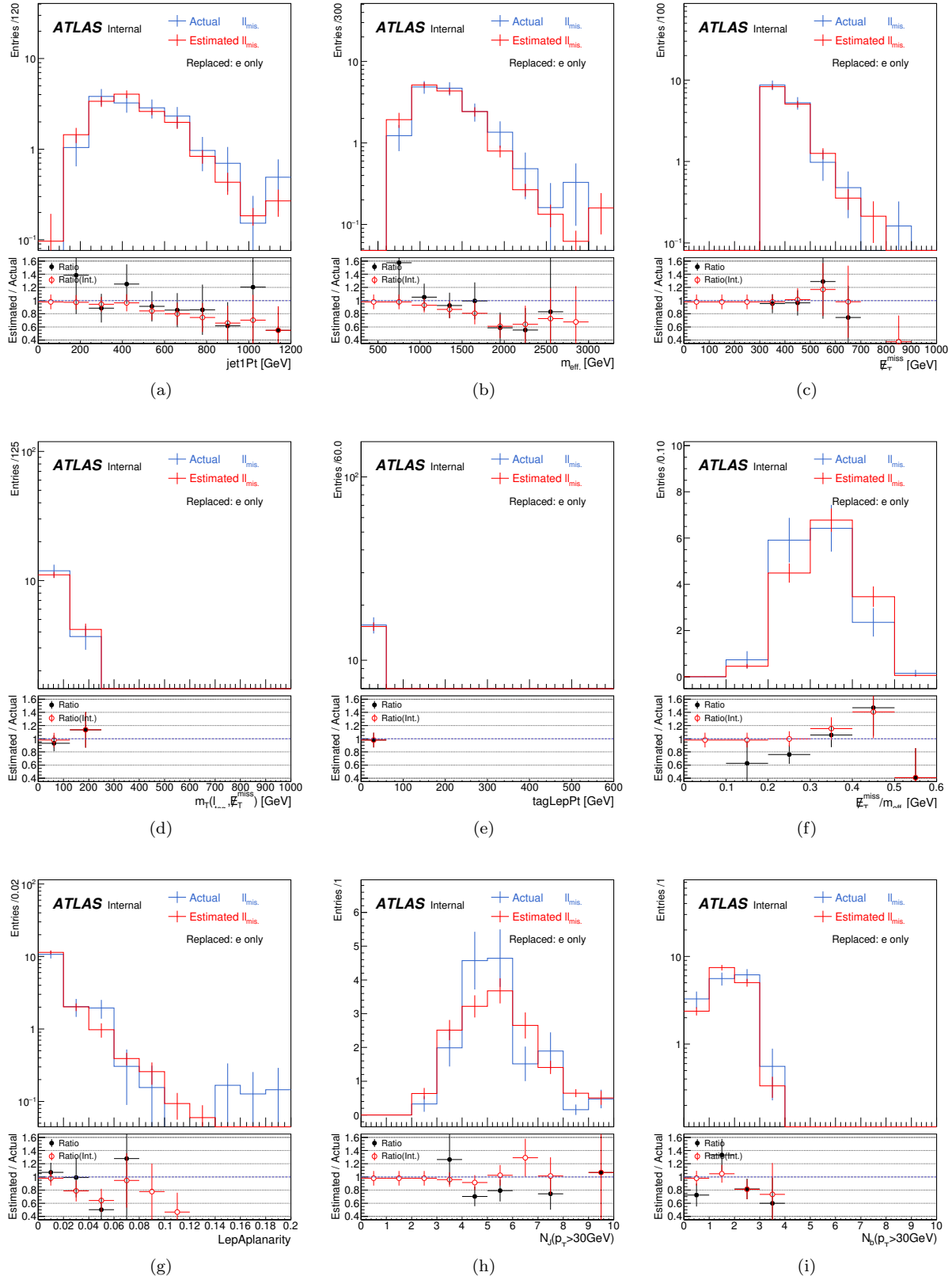


Figure 64: MC closure test for **missing lepton replacement** using di-leptonic $t\bar{t}$ sample (410009). Seed events are collected by the use of MET trigger. $p_T < 35\text{GeV}$ for the leading lepton is required. **Only electrons in the seed events are replaced.** All distribution are normalized with $\int Ldt = 36.5\text{fb}^{-1}$.

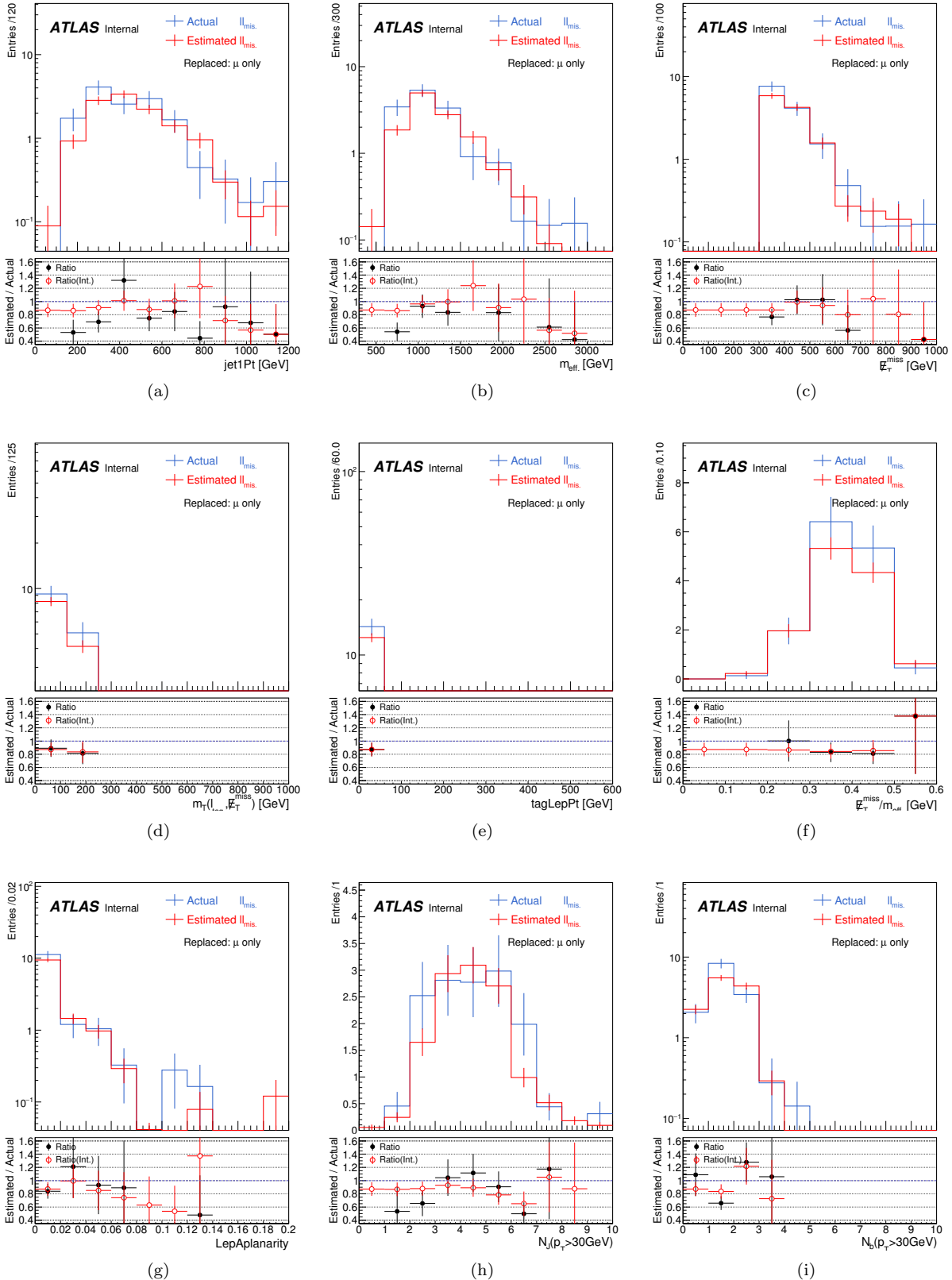


Figure 65: MC closure test for **missing lepton replacement** using di-leptonic $t\bar{t}$ sample (410009). Seed events are collected by the use of MET trigger. $p_T < 35 \text{ GeV}$ for the leading lepton is required. **Only muon in the seed events are replaced.** All distribution are normalized with $\int L dt = 36.5 \text{ fb}^{-1}$.

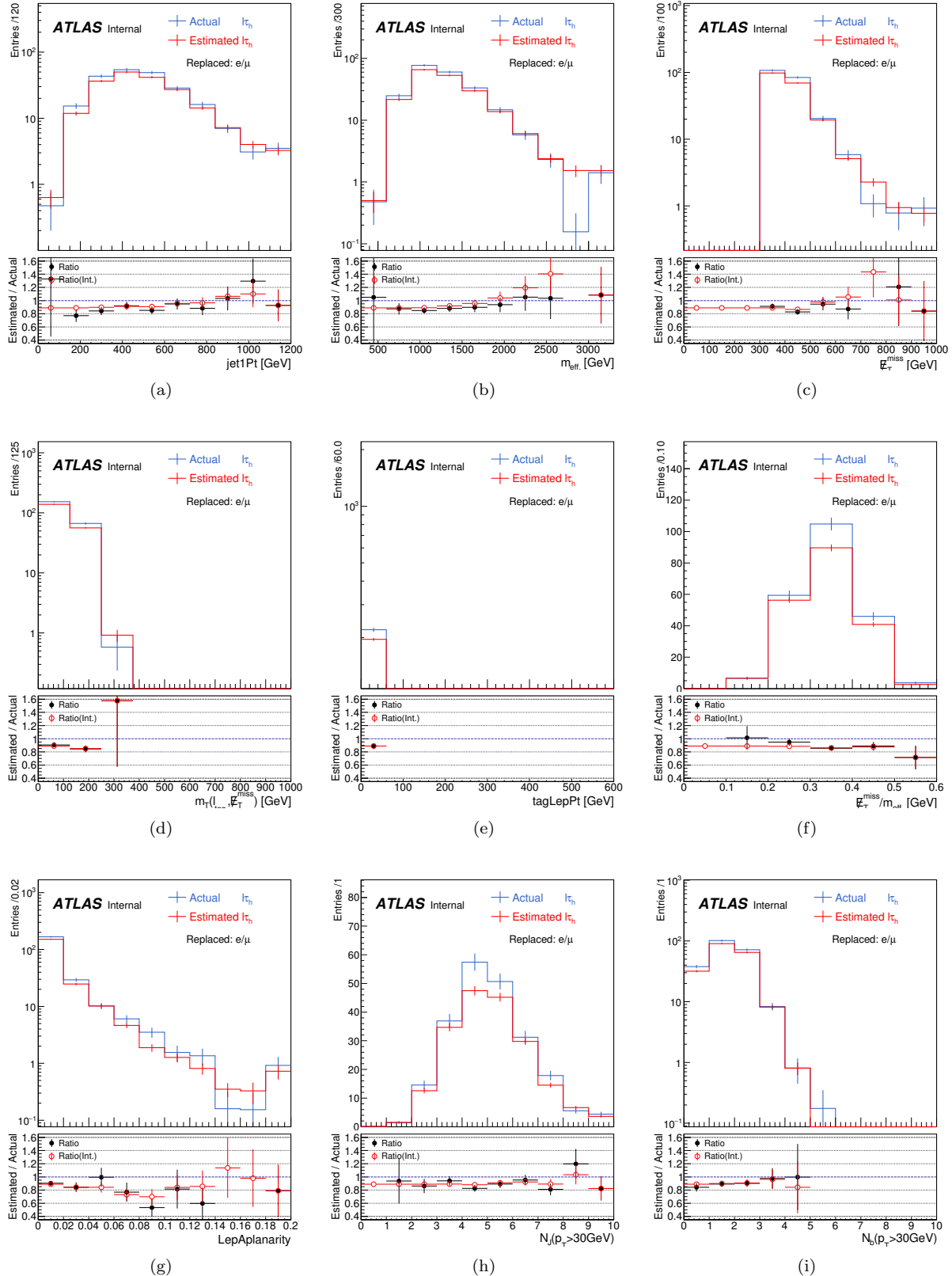


Figure 66: MC closure test for **tau replacement** using di-leptonic $t\bar{t}$ sample (410009). Seed events are collected by the use of MET trigger. $p_T < 35\text{GeV}$ for the leading lepton is required. **Both electrons and muons in the seed events are replaced.** All distribution are normalized with $\int L dt = 36.5\text{fb}^{-1}$.

6.4.4 Source of non-closure

Visible non-closures are found in some distributions such as MET and jetPt etc. These are mainly due to following reasons:

Kinematical bias triggered by the two lepton requirement in seed event selection (All)

Since objects decaying from heavily boosted particles get collimated and overlapped each other, offline selection efficiency for leptons (either eff. of reconstruction, ID, and overlap-removal) is generally deteriorated in phase space with hard kinematics. This is in the same time means that selecting events with exactly two offline leptons already biases the kinematics, since the events in the “boosted topology” tends to be discarded. Therefore spectra estimated by 2 lepton seed events will be generally softer. Electrons address larger effect because the efficiency drop in the boosted environment is more severe than muons (plots will come later).

Too rough treatment of MET soft term for missing muon (missing muon replacement)

Currently missing muons are completely regarded as invisible particles and their 4-vector are naively added in MET recalculation, while in reality their contribution are more likely to be counted in the MET track soft term. This inconsistent modeling is supposed to be the dominant source of non-closure in MET related variables in the missing muon replacement. Naively thinking, this can be improved by simply adding the missing muons into the track soft term. However this seems not the case according to 67. The reason has not been fully understood, but it is perhaps due to the bad resolution of muon tracks added into TST.

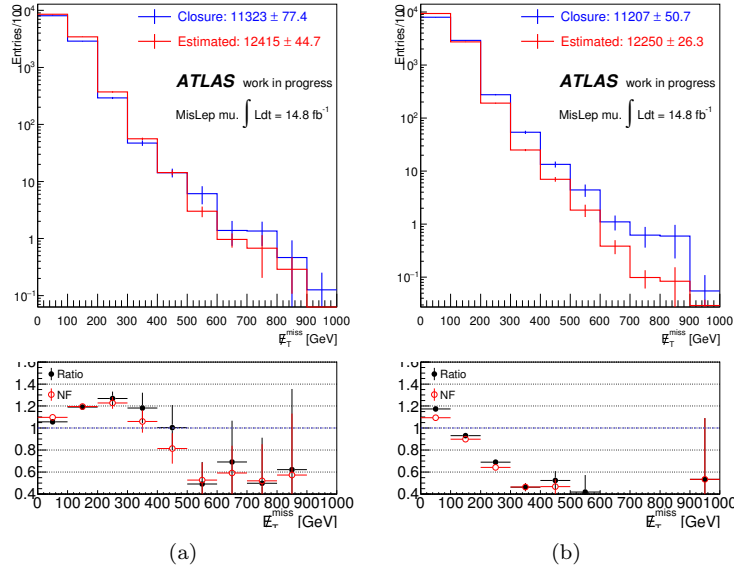


Figure 67: Closure in MET distribution. (a) Default treatment of missing muon (count as invisible). (b) Always add missing muons in the TST.

Wrong assumption on tau polarization (tau replacement)

For technical simplicity, tau leptons are assumed to be unpolarized during the decay. This is of course not true as tau leptons are usually generated through weak decay of W-bosons. In the tau replacement, the MC non-closure in MET (and m_T etc.) is understood by this polarization effect. Fig. 68 and fig.

69 describe a test of reweighting in terms of visible tau fraction $x := E(\tau_h)/E(\tau)$, known as a variable sensitive to the polarization of parent tau, where the closure successfully recover. Although this x -reweighting correction works quite nicely, given the impact of this non-closure is marginal in our signal regions ($< 5\%$), we decided not to apply any corrections to avoid further complexity of the method.

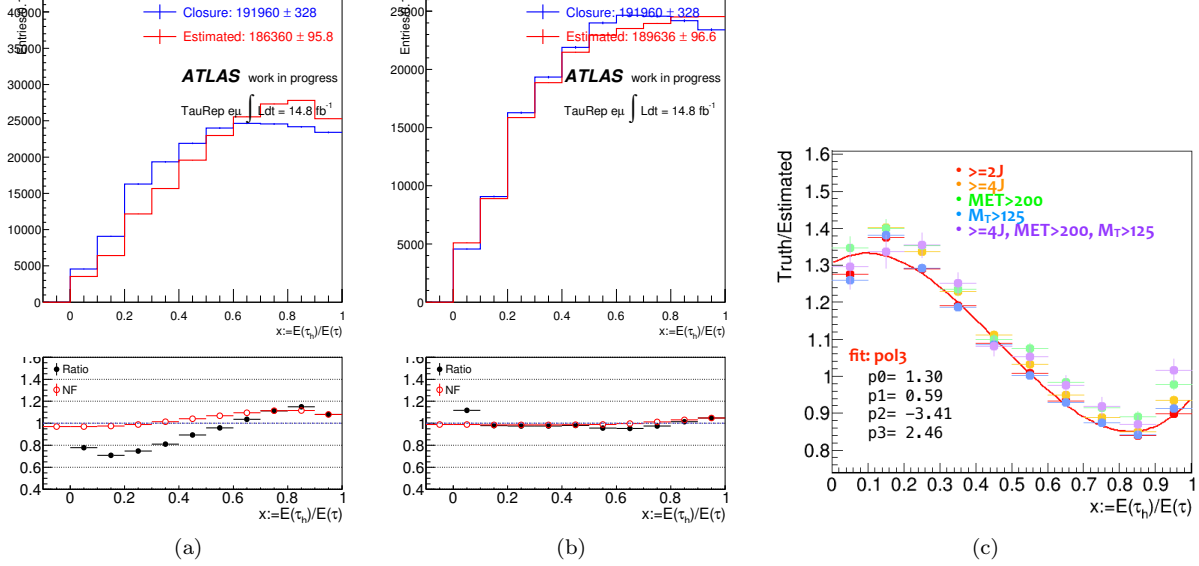


Figure 68: Reweighting in terms of the visible tau fraction $x := E(\tau_h)/E(\tau)$. (a) x distribution before the reweighting , (b) x distribution after the reweighting. (c) An ad hoc fit of the reweighting function by third order polynomial. The reweighting function is almost invariant in terms of phase space.

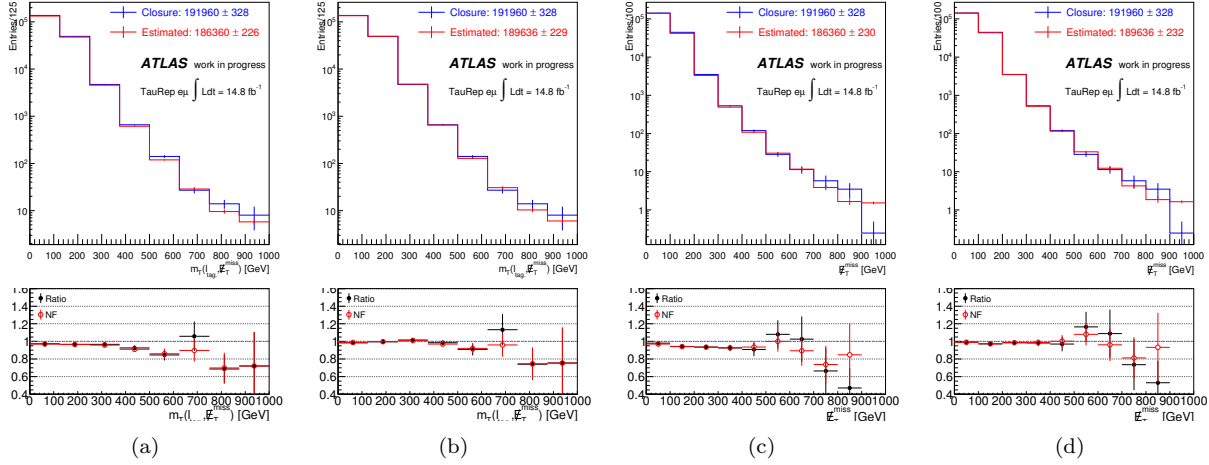


Figure 69: (a) m_T and (c) MET distribution before the reweighting in x , and (b)(d) after the reweighting.

6.4.5 Closuer test with tigher selection

Closure tests are also performed in phase space close to signal regions. Fig. 70 ~ 75 are the btag/bveto-splitted closure in various regions requiring high MET, m_T , m_{eff} . etc. The non-closure stay within 30% (10%) for the missing lepton replacement (the tau replacement).

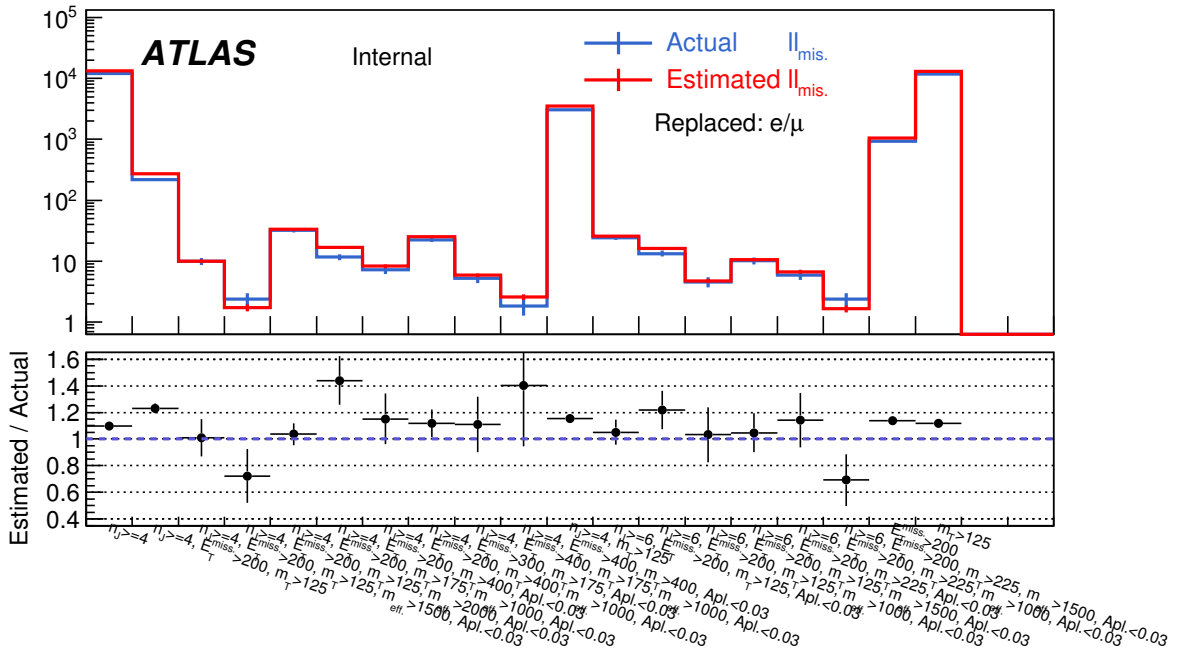


Figure 70: MC closure test for **missing lepton replacement** in SR-like **b-tagged** regions. Pre-selection $p_T(\ell_1) > 35\text{GeV}$ is applied on top of the cuts noted by the labels.

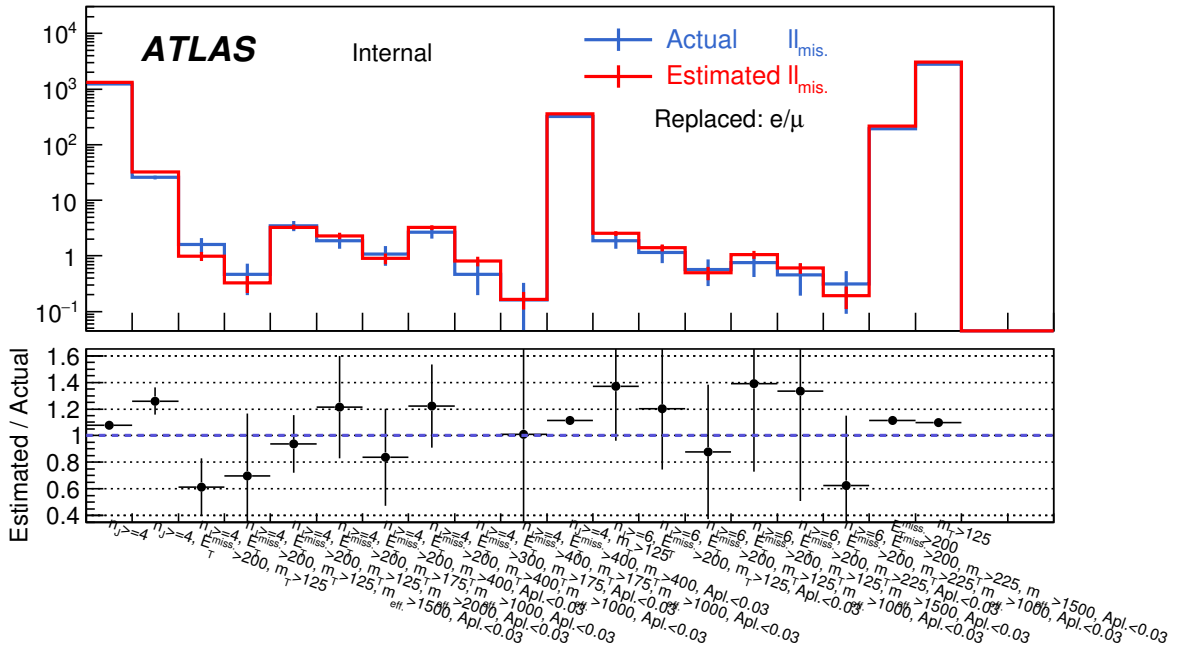


Figure 71: MC closure test for **missing lepton replacement** in SR-like **b-vetoed** regions. Pre-selection $p_T(\ell_1) > 35\text{GeV}$ is applied on top of the cuts noted by the labels.

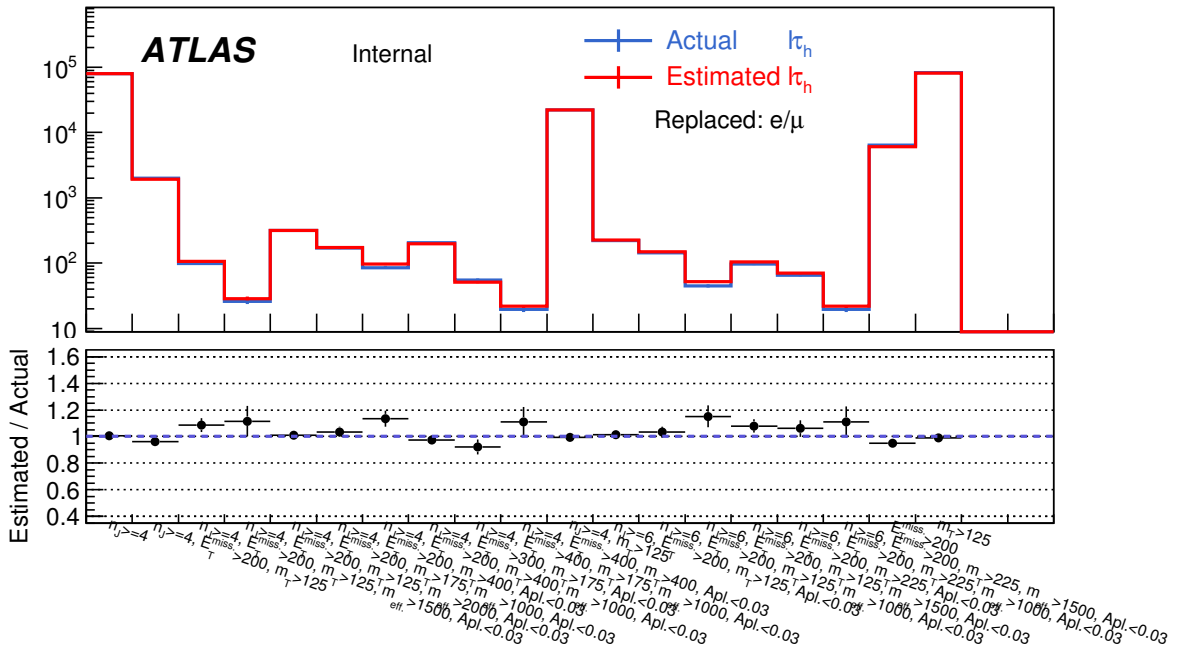


Figure 72: MC closure test for **tau replacement** in SR-like **b-tagged** regions. Pre-selection $p_T(\ell_1) > 35\text{GeV}$ is applied on top of the cuts noted by the labels.

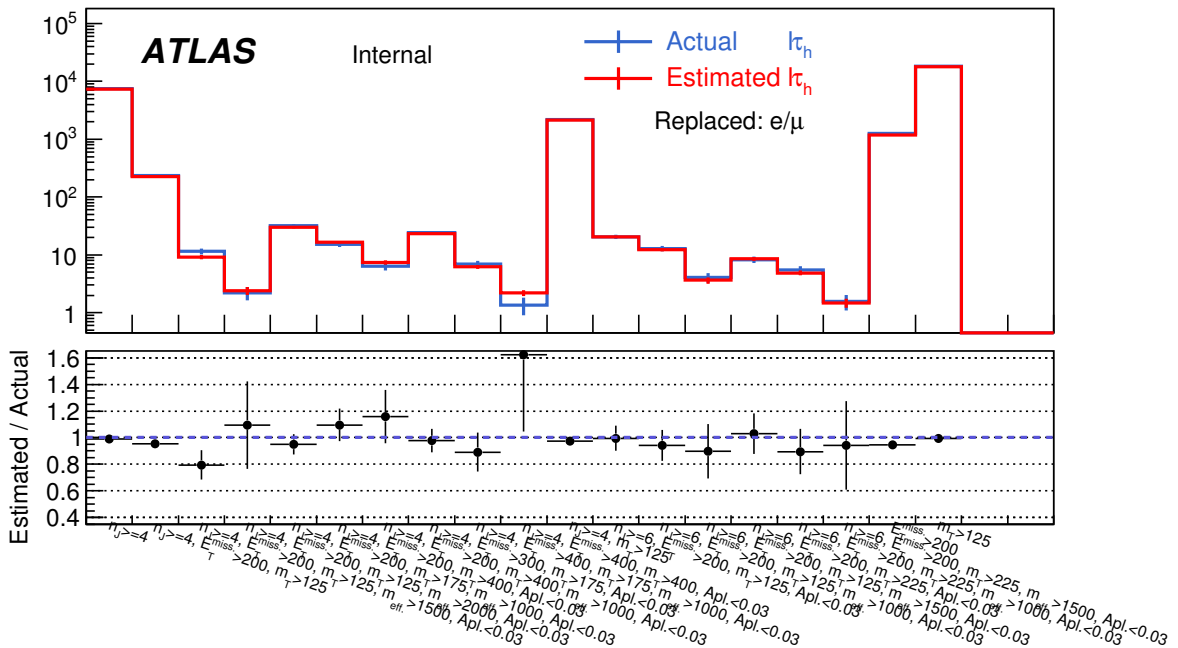


Figure 73: MC closure test for **tau replacement** in SR-like **b-vetoed** regions. Pre-selection $p_T(\ell_1) > 35\text{GeV}$ is applied on top of the cuts noted by the labels.

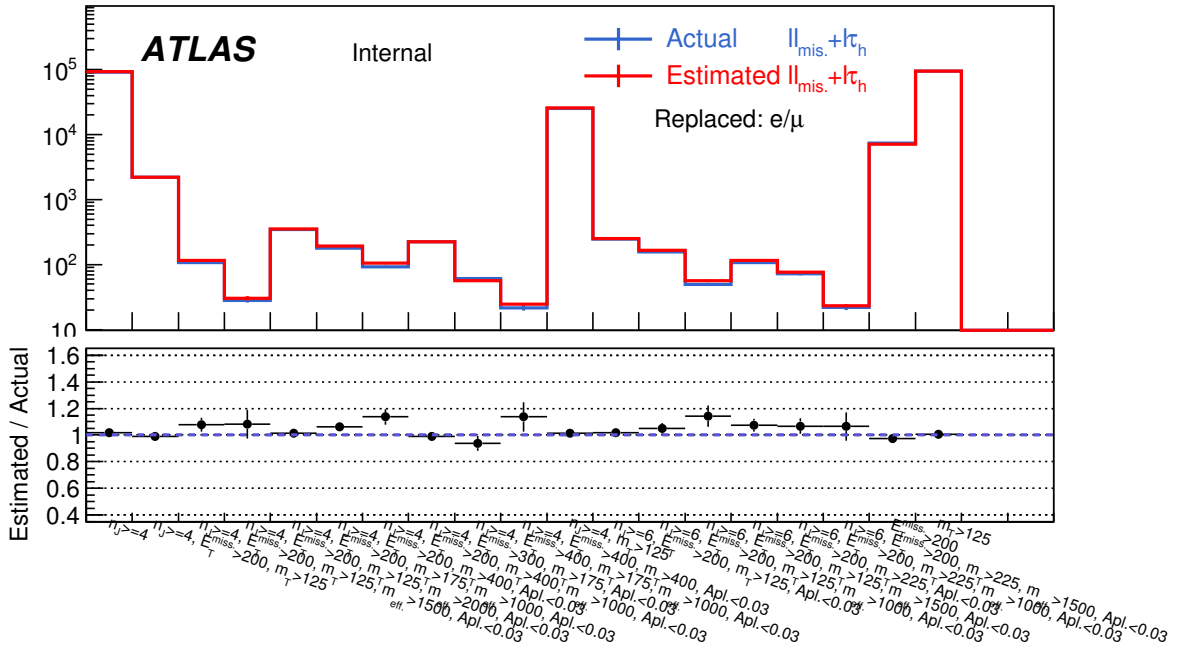


Figure 74: MC closure test for **combined estimation of missing-lep. rep. and tau replacement** in SR-like **b-tagged** regions. Pre-selection $p_T(\ell_1) > 35\text{GeV}$ is applied on top of the cuts noted by the labels.

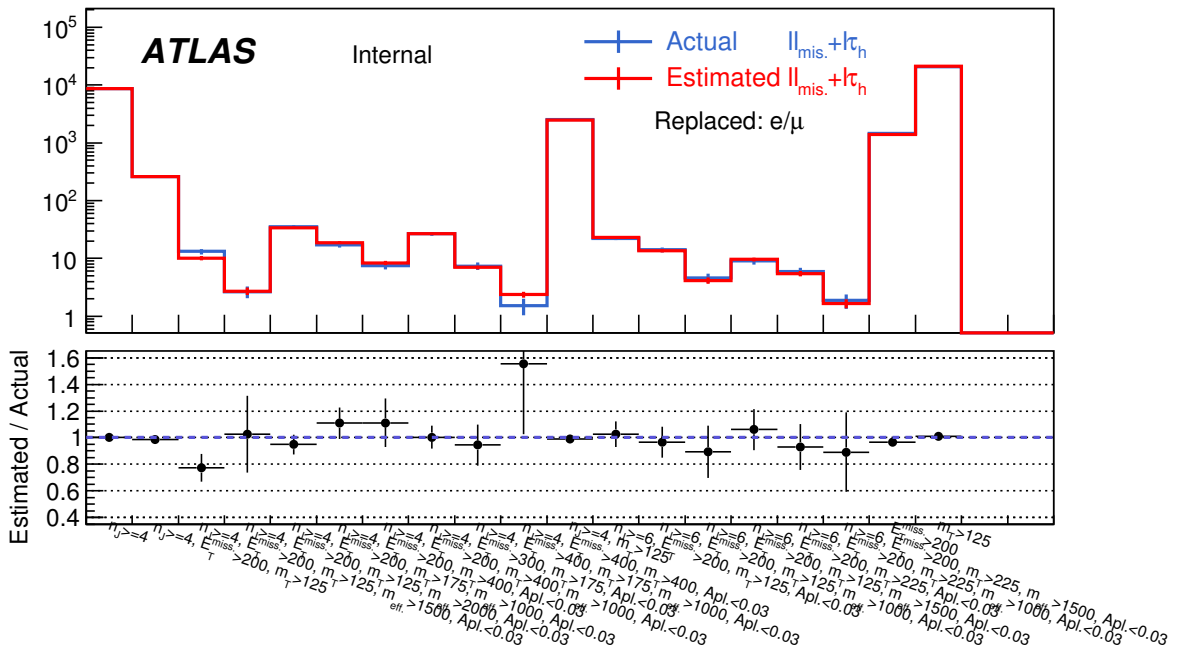


Figure 75: MC closure test for **combined estimation of missing-lep. rep. and tau replacement** in SR-like **b-vetoed** regions. Pre-selection $p_T(\ell_1) > 35\text{GeV}$ is applied on top of the cuts noted by the labels.

6.4.6 Closure test using data in 1-lepton validation regions.

The method is also validated by data using 1L validation regions (1LVRs) dominated by $\ell\ell_{\text{mis.}}$ and $\ell\tau_h$. There are two procedures to be implemented additionally when moving from MC closure test to application to data:

Subtraction of irrelevant component

As it is impossible to know the BG species in a single data event, some of events from irrelevant processes ($W+\text{jets}$ etc.) in 2LCR are inevitably undergo the replacement, generating "fake" sub-events which no processes in 1L regions correspond to. This contribution has to be removed using the knowledge of MC. The example of relevant and irrelevant processes are summarized in tab.15. Basically processes with exactly two leptons are "relevant", except for $\ell\tau, \tau \rightarrow \ell\nu\nu$ ($\ell\tau_\ell$) and $Z \rightarrow \ell\ell$. $\ell\tau_\ell$ is the largest component to be subtracted in the tau replacement (10% \sim 20%). As the impact of MC mis-modeling is usually non-negligible, the ratio to the contribution from relevant components are taken from MC, instead of the absolute yield, to avoid the direct impact of mis-modeling. Namely,

$$y_{\ell\ell}^{\text{Data}} = y_{\ell\ell+\ell\tau_\ell}^{\text{Data}} \times \frac{y_{\ell\ell}^{\text{MC}}}{y_{\ell\ell}^{\text{MC}} + y_{\ell\tau_\ell}^{\text{MC}}} \quad (11)$$

$$= y_{\ell\ell+\ell\tau_\ell}^{\text{Data}} - \frac{y_{\ell\ell}^{\text{Data}}}{y_{\ell\ell}^{\text{MC}}} \times y_{\ell\tau_\ell}^{\text{MC}} \quad (12)$$

where $y_{\ell\ell}^{\text{Data}}$ ($y_{\ell\ell+\ell\tau_\ell}^{\text{Data}}$) denote the yield estimated from data before (after) the subtraction, and $y_{\ell\ell}^{\text{MC}}$ ($y_{\ell\tau_\ell}^{\text{MC}}$) the estimated yields with the seed events being $\ell\ell$ ($\ell\tau_\ell$) MC.

The other sources of irrelevant processes are negligible therefore raw MC prediction is used in subtraction. $\ell\ell_{\text{fake}}$ (e.g. $W+\text{jets}$) is a bit sensitive component since MC prediction is not very reliable, however this is well-suppressed by requiring isolation for both two leptons in 2LCR.

Table 15: Relation between BG components in seed events and estimated components in 1L regions. \times indicates that no components can be estimated by replacing events of the corresponding process in seed events, and need to be subtracted. τ_ℓ ($\tau_{\ell,\text{mis.}}$) denotes (missing) leptons from leptonically decaying tau.

Seed events	Estimated by mis. lep. rep.	Estimated by tau rep.
$t\bar{t} \rightarrow \ell\ell$	$t\bar{t} \rightarrow \ell\ell_{\text{mis.}}$	$t\bar{t} \rightarrow \ell\tau_h$
$Wt \rightarrow \ell\ell$	$Wt \rightarrow \ell\ell_{\text{mis.}}$	$Wt \rightarrow \ell\tau_h$
$WW \rightarrow \ell\ell$	$WW \rightarrow \ell\ell_{\text{mis.}}$	$WW \rightarrow \ell\tau_h$
$t\bar{t} \rightarrow \ell\tau_\ell$	$t\bar{t} \rightarrow \ell\tau_{\ell,\text{mis.}}, t\bar{t} \rightarrow \ell_{\text{mis.}}\tau_\ell$	\times
$Z \rightarrow \ell\ell$	$Z \rightarrow \ell\ell_{\text{mis.}}$	\times
$W \rightarrow \ell\nu + \ell_{\text{fake}}$	\times	\times

Add BG components that can not be estimated by the object replacement using MC

Scale factors are applied for $W+\text{jets}$ and $t\bar{t}$ to account for the MC mis-modeling, while raw MC prediction is quoted for the other minor processes. The scale factors are derived respectively for each 1LVR in a similar manner as the nominal estimation i.e. performing a simultaneous fit of b-tagged and b-veto bins of 1LCR where only the m_T cut is flipped ($m_T \in [60, 125]$), and the other cuts are identical with respect to 1LVR.

The result of the closure test is presented in fig.76. The agreement with data is found to be within statistical uncertainty.

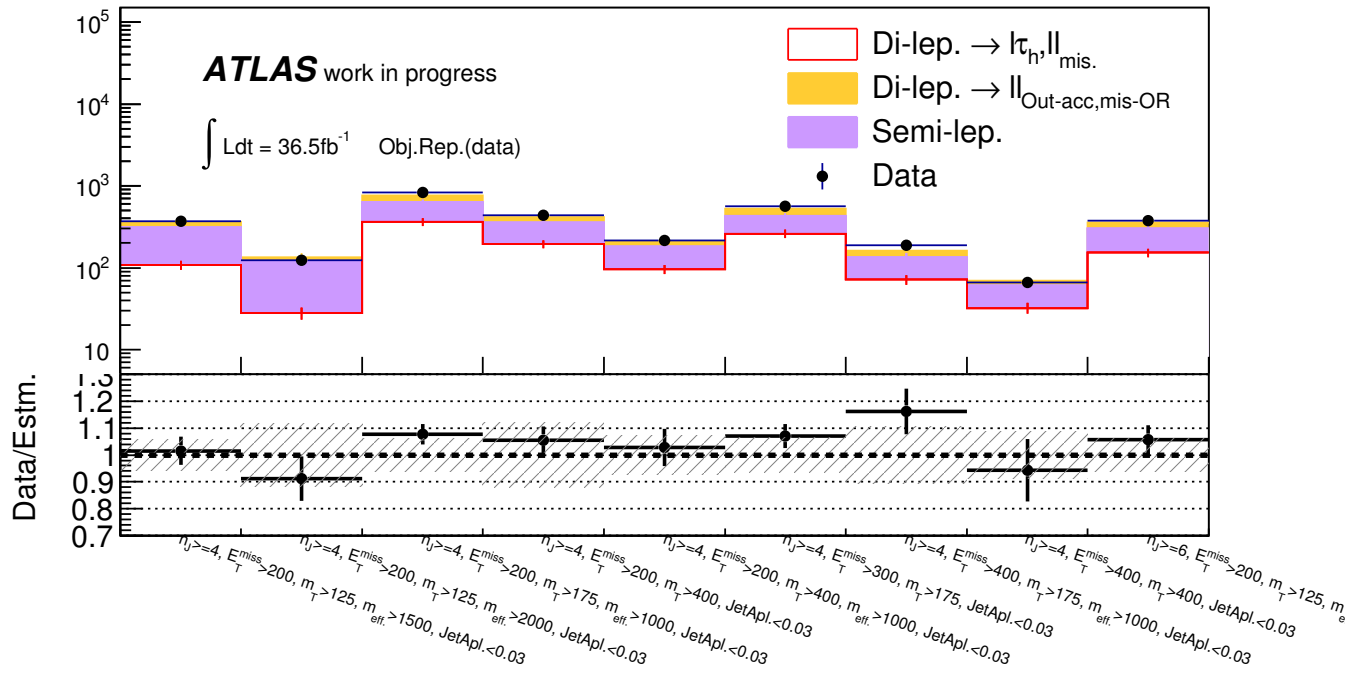


Figure 76: Closure test using data in various 1LVRs.

6.5 Multi-jet Validation using Data

Backgrounds estimation on the multi-jets processes is fully taken from MC as the contribution is shown to be small. However the prediction can drastically change due to the large statistical uncertainty and the questionable modeling of higher order effects. The impact could be fatal once it turns to contribute because of its huge cross-section. Therefore a data-driven validation is performed using the exclusively designed validation regions for the “QCD” components (VR-QCD). VR-QCDs are defined by inverting the isolation requirement on the final state lepton with respect to SRs. Due to the high rejection factor of isolation, which is typically $10 - 20$ ($5 - 10$) for fake electrons (muons), the “QCD” abundance is enhanced by around factor of 10. Fig. 1 are the m_{eff} distribution of VR-QCDs. Note that the multi-jets process is not included in MC thus the contribution would emerge as excess in data if it is significant. Normalization factors calculated in Sec. 1 is applied to $W + \text{jets}$ and $t\bar{t} + Wt$. Nice agreement between MC and data is seen overall, indicating the good background modeling of the kinematical expolation method and the absent contribution from multi-jet process.

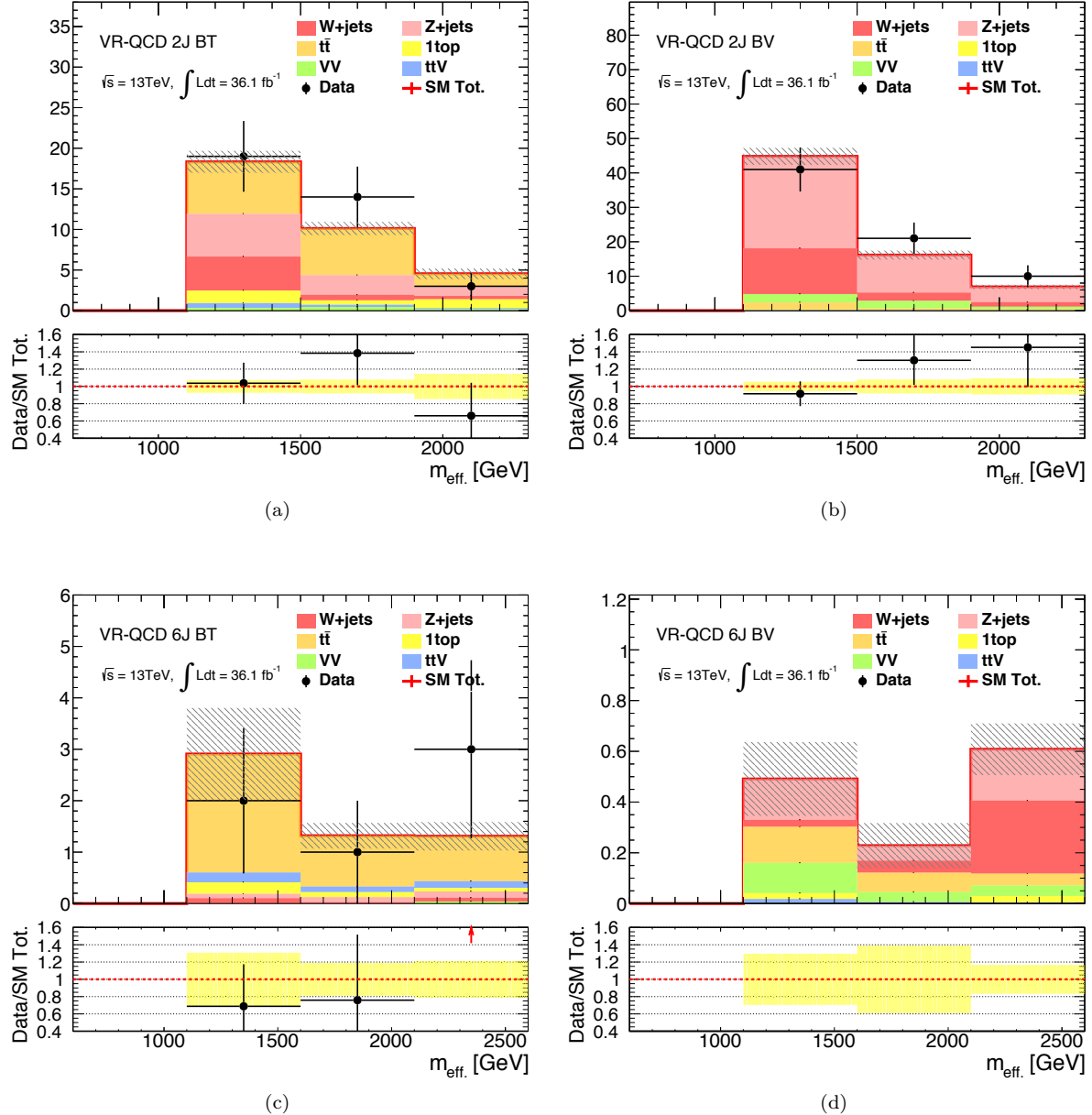


Figure 77: VRQCD for towers (a) 2JBT (b) 2JBV (c) 6JBT (d) 6JBV.

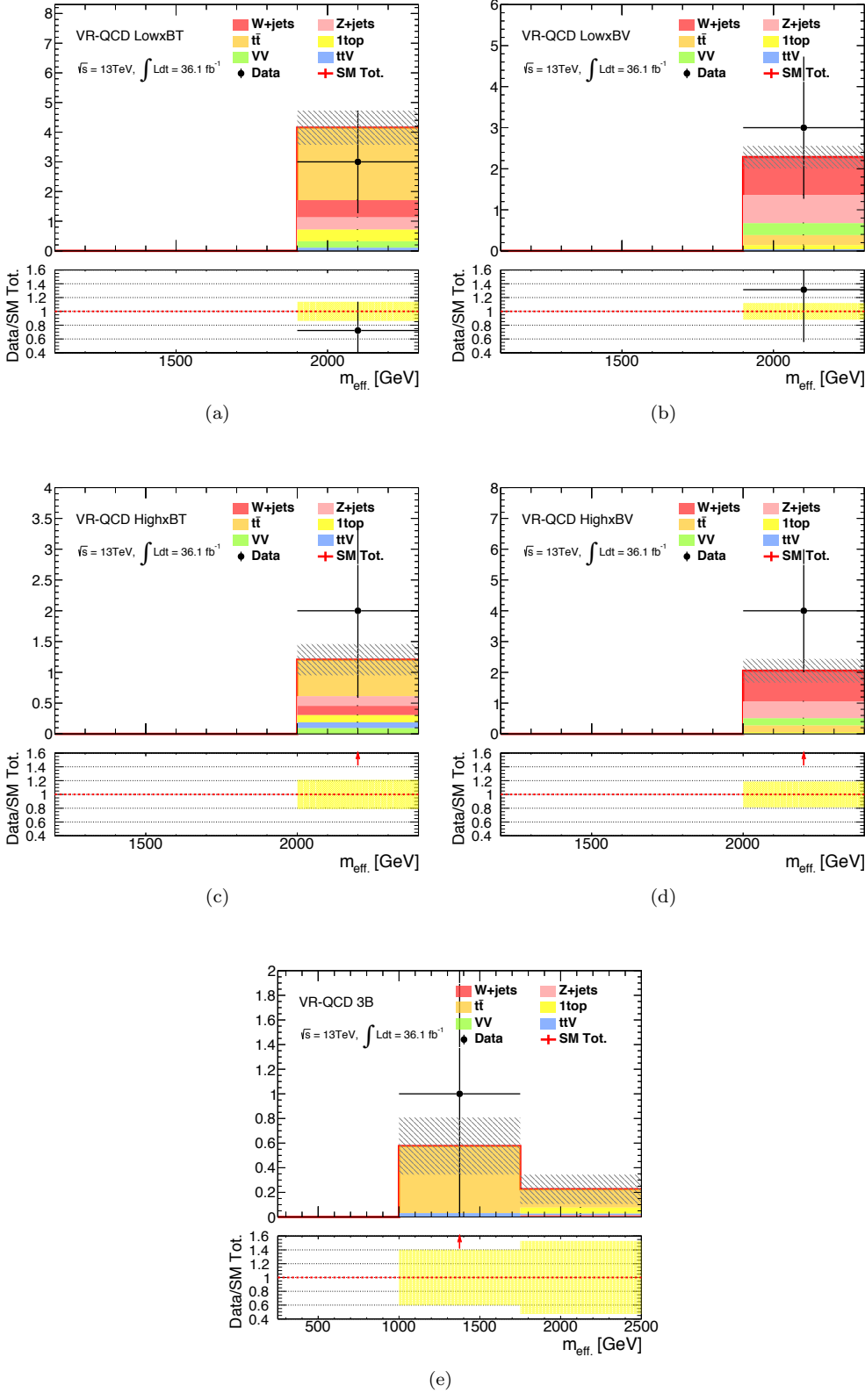


Figure 78: VRQCD for towers (a) LowxBT (b) LowxBV (c) HighxBT (d) HighxBV (e) 3B.

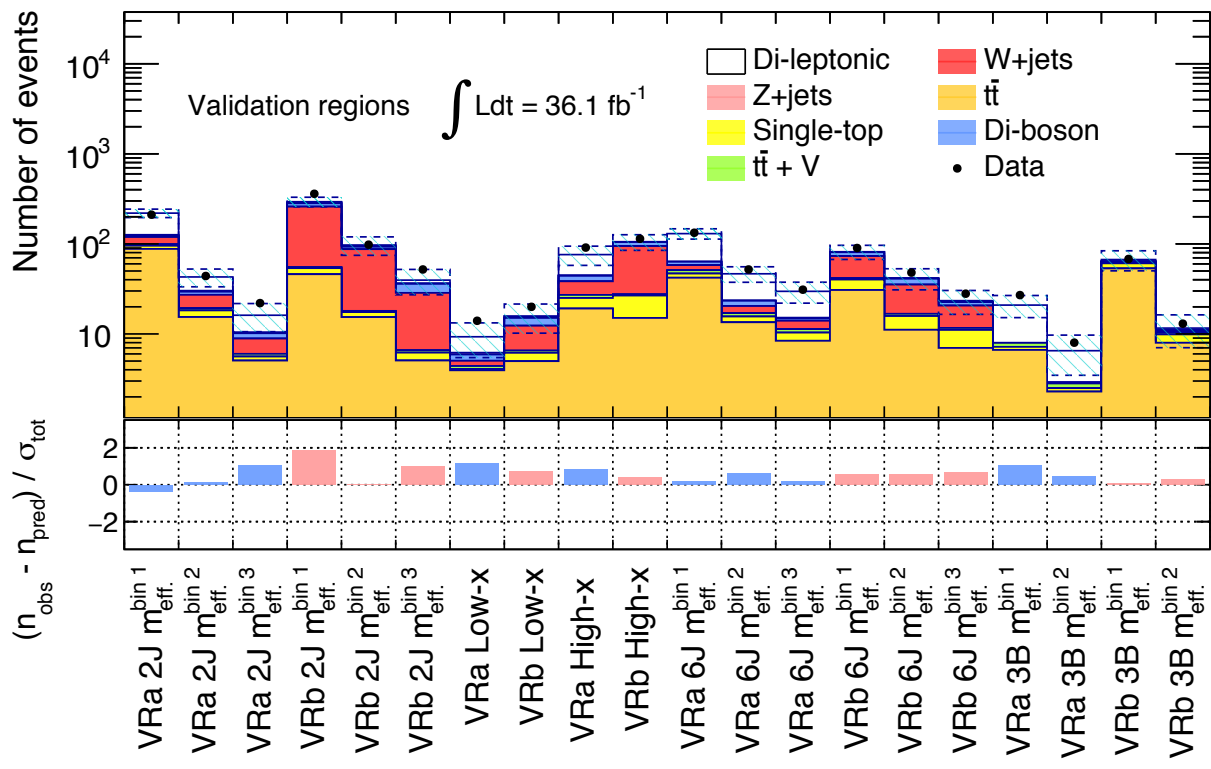


Figure 79:

6.6 Unblinded Validation Regions

7 Systematic Uncertainties

Uncertainties associated with background estimations and the signal modeling is dedicatedly discussed in this section. The listed uncertainties are implemented in the simultaneous fit to determine either the normalization factors and the signal strength, through corresponding nuisance parameters.

7.1 Impact on Kinematical Extrapolation Method

The affected systematics are largely two-fold: modeling uncertainties on the detector response including residual imperfection of calibrations or the error on efficiency measurements (“instrumental uncertainty”) and uncertainties on theoretical description of physics processes (“theoretical uncertainty”).

7.1.1 Instrumental Systematic Uncertainty

Jets Despite the dedicated calibration procedures as noted in Sec. 1, the residual uncertainty on jet energy scale (JES) is the largest source of instrumental uncertainty. The uncertainty arising in each step of the sequential calibration are respectively parametrized by jet’s (p_T, η, ϕ), resulting in 87 independent nuisance parameters. In this thesis, for simplicity, they are reduced into effective 8 nuisance parameters by combining uncertainties under the similar (p_T, η, ϕ) dependency in quadrature. JES for jets from heavy flavor quarks (b,c-quarks) are separately considered. The impact is evaluated using MC by scaling the energy of each jet in the event up and down by 1σ . Uncertainty on jet energy resolution is also taken into account. It is originated mainly from imperfect modeling of hadronic shower shape and its response by calorimeters, and the resolution difference between one calculated from MC and the measured one is quoted as uncertainty. Similar to JES, the MC variation is generated by additionally smearing the jet energy on jet-by-jet basis according to the Gaussian profile with the width of JER uncertainty.

JES/JER uncertainties can have large impact on background estimation since the tail of distribution can significantly prolonged or shortened through the cumulative effect on jets and accordingly the MET measurement, as shown in Fig. 1 for instance. Although the impact is largely cancelled out by the normalization in control regions in the same m_{eff} slice, there is still some residual effect through varied shape of m_T distribution. The eventual effect in final estimation amounts up to $5\% \sim 15\%$.

Systematics on flavor tagging efficiency are also noticeable since the analysis significantly relies on the classification in b-tagged jet multiplicity.

Uncertainty on jet eta scale, pileup modeling, modeling of the JVT profile are also taken into account, which impacts on the final result are found to be negligible.

Electron/Muon The major sources of uncertainty on electron and muon are about the scale, resolution and reconstruction/ID/isolation efficiencies, which are quoted from the observed data/MC discrepancies in the $Z \rightarrow \ell\ell$ tag-probe measurement as described in Sec. 1. None of them provides more meaningful impact than 1% in the background estimation,

MET On top of the uncertainties on jet/lepton kinematics which are propagated, MET suffers from additional uncertainty regarding to the modeling of track soft term.

7.1.2 Theoretical Uncertainty

7.1.3 Others

Control region statistics Reflecting the semi-data driven nature of the method, in most of the high m_{eff} bins, the fitting error on normalization factors turn to be the largest uncertainty in background expectation in signal regions due to the scarce statics of control regions.

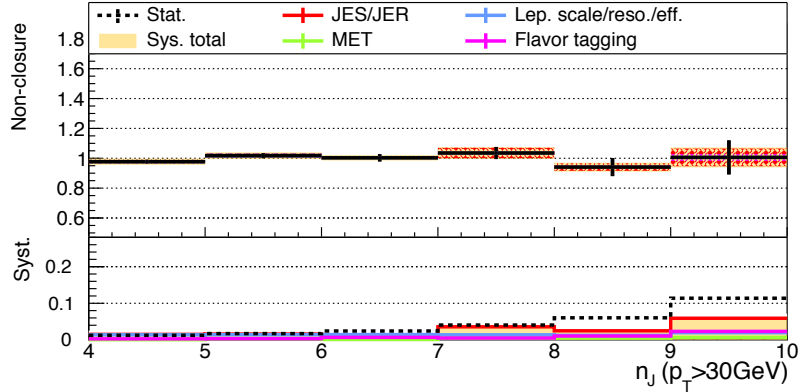
MC statistics Due to the finite computation resource, MC statical error comes to non-negligible in signal regions at tight selection. This is caused typically in processes with large cross-section such as $W + \text{jets}$ and $t\bar{t}$, and some minor processes with less importance (diboson). It could boast 15% of total background expectation at the worst case (SR3BMEFF2), however it never becomes dominant source of uncertainty in either of signal regions.

7.2 Impact on the Object Replacement Method

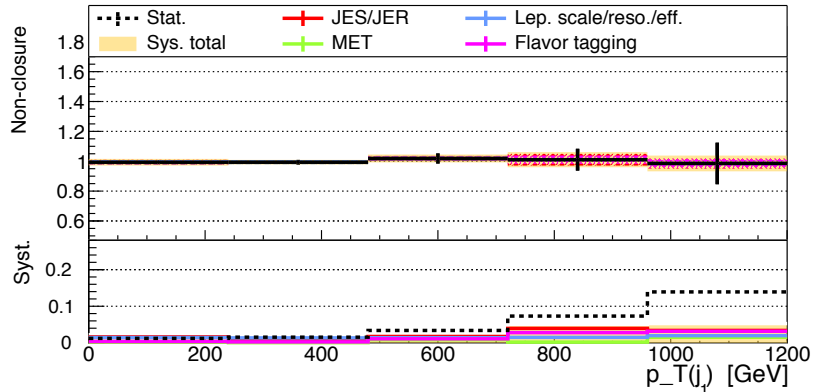
Uncertainty on the object replacement method is predominantly from statistical uncertainty in 2LCR that amounts 20% – 50% regions depending on the tightness of selection. The sub-dominant contributions are from the non-closure error where 10% (25%) is assigned for tau replacement (missing-lepton replacement) based on the closure test. Uncertainty regarding to the MC subtraction is also taken into account (1% \sim 8%) in which MC statics addresses the most.

Though limited, intrumental uncertainties can still have non-zero influence through the modeling of lepton efficiency and the tau response functions that are fully based on the nominal MC configuration. MC closure tests are performed using $t\bar{t}$ samples with all the intrumental variations described in the previous sub-section applied. Fig 80 ~ 82 shows the shifts of non-closure under the variations. Although the variated samples are statistically correlated partially each other, no statistically evident impact above 5% is observed.

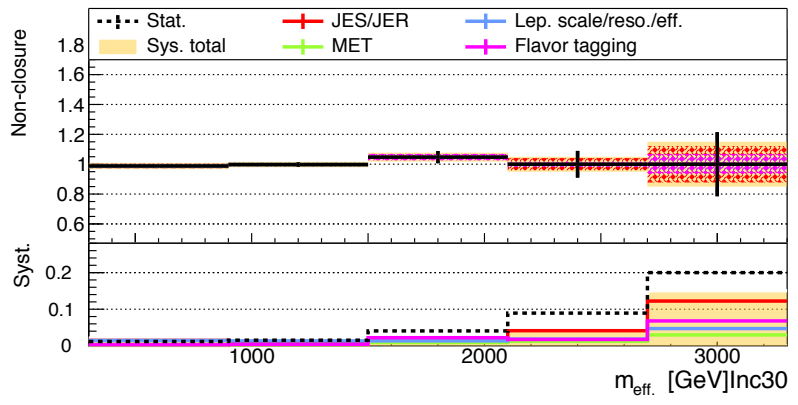
The method is highly robust against the theoretical uncertainties by construction. Fig 83-84 are a part of the validation in which consistent level of closures between the nominal $t\bar{t}$ sample and alternative samples (scaleUp/Down and Powheg+Herwig++ respectivly) are confirmed.



(a)

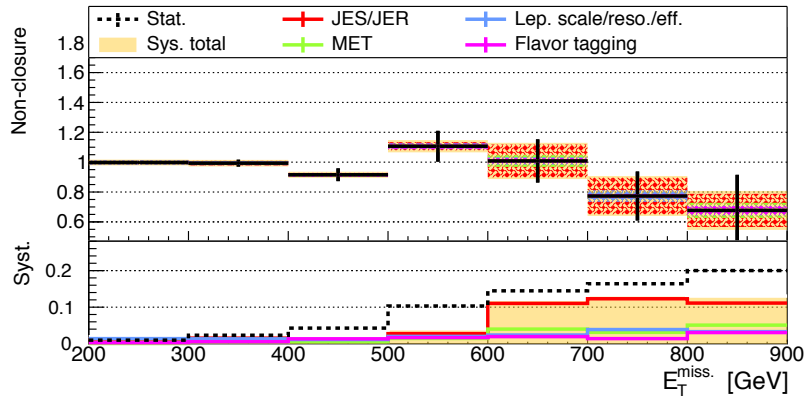


(b)

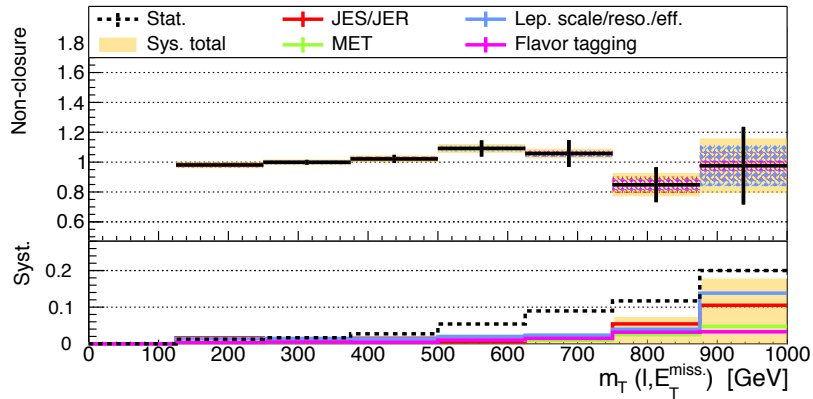


(c)

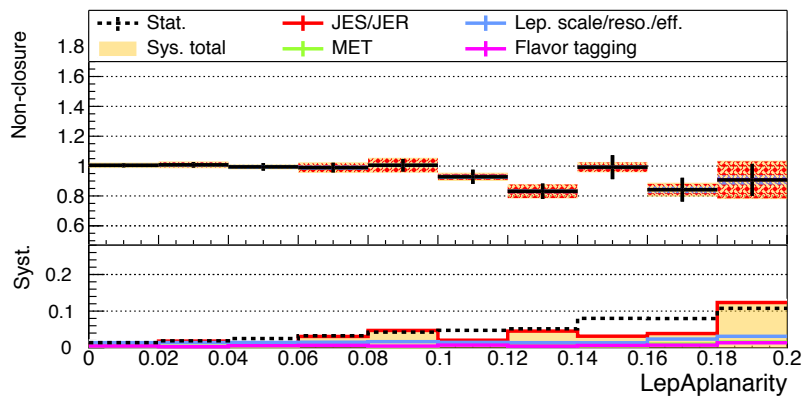
Figure 80: Impact by instrumental systematics on the MC closure for (a) jet multiplicity ($p_T > 30 \text{ GeV}$) (b) leading-jet pt (c) E_T^{miss} (d) m_{eff} . Pre-selection ($n_J \geq 4$, $E_T^{\text{miss}} > 200$, $m_T > 125$) is applied.



(a)

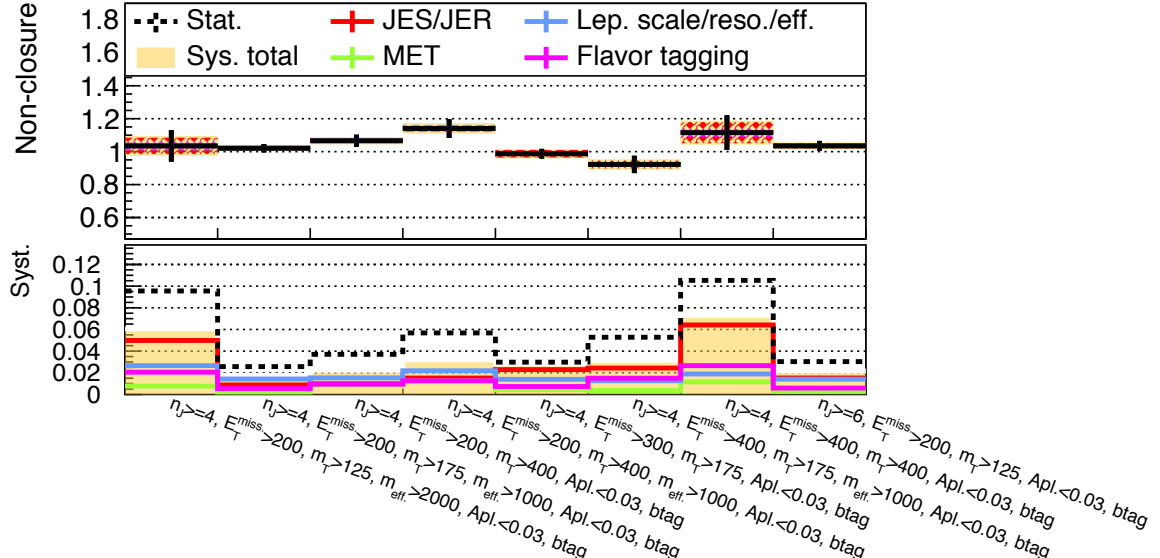


(b)

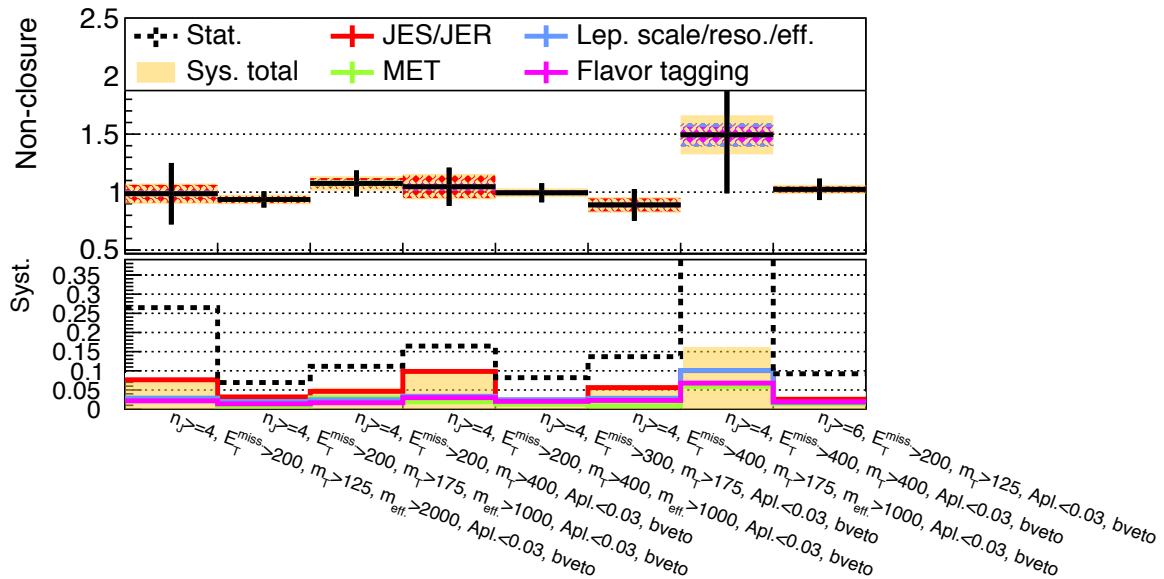


(c)

Figure 81: Impact by instrumental systematics on the MC closure for (a) m_T (b) $p_T(\ell)$ (c) $E_T^{\text{miss}}/m_{\text{eff}}$ (d) aplanarity. Pre-selection ($n_J \geq 4$, $E_T^{\text{miss}} > 200$, $m_T > 125$) is applied.



(a)



(b)

Figure 82: Impact by instrumental systematics on the MC closure under various (a) b-tagged and (b) b-vetoed SR-like selections. (Top) Black dots are the closure with the nominal sample and the error bars are the associated statistical uncertainties. Dashed bands represent the variation caused by the systematic variations. (Bottom) Relative variation in closure with respect to that of the nominal sample.

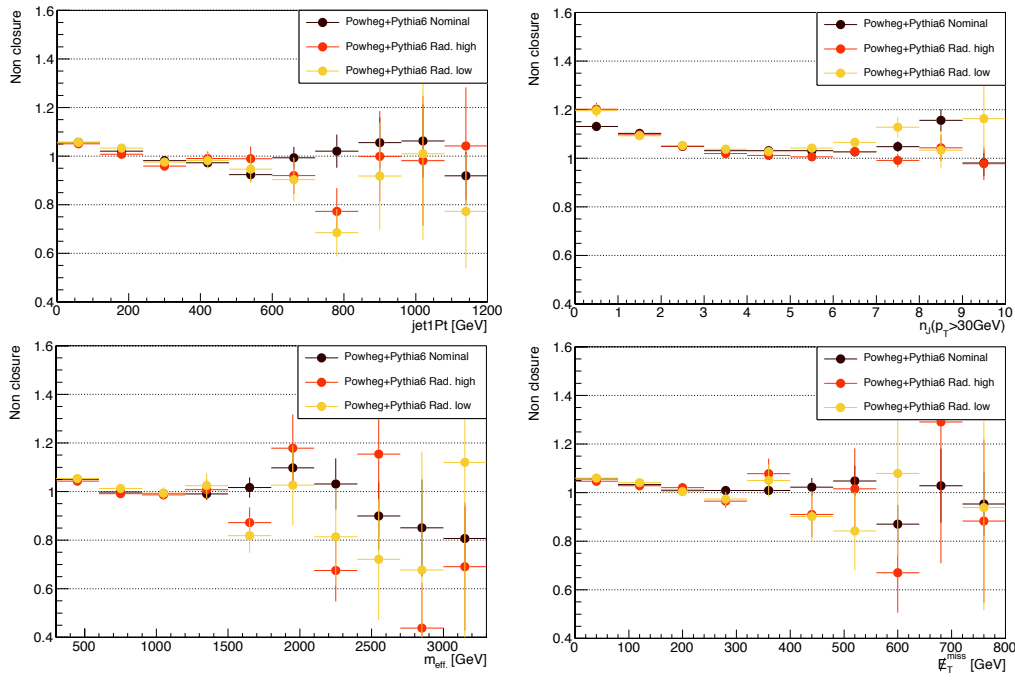


Figure 83: Comparison of MC closure with different radiation configuration. Pre-selection: $p_T(\ell_1) > 35\text{GeV}$.

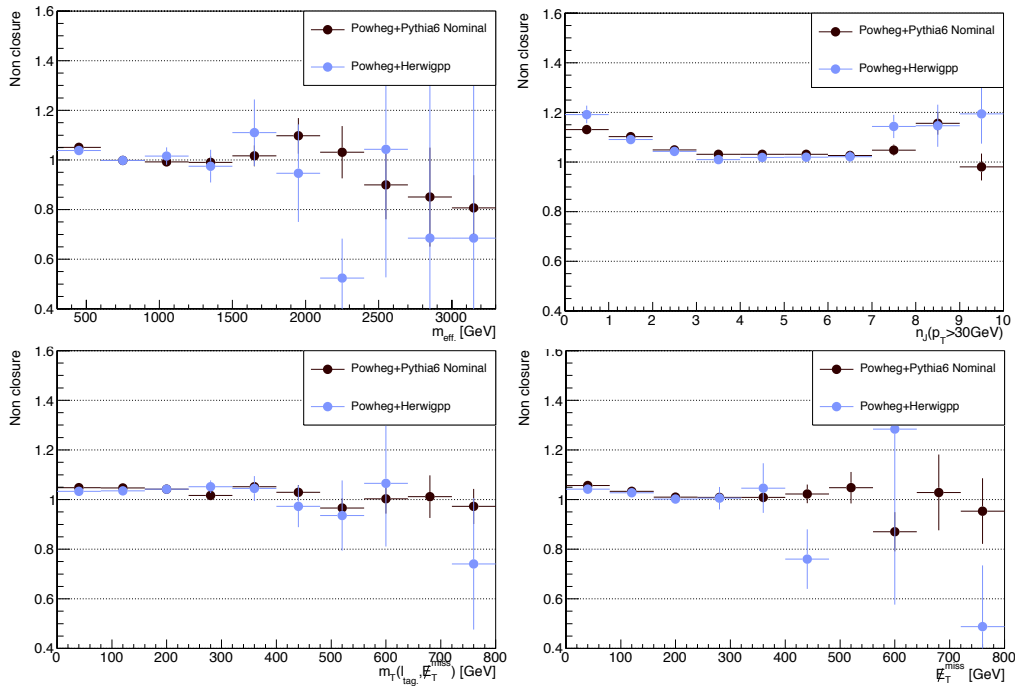


Figure 84: Comparison of MC closure with different hadronization scheme. Pre-selection: $p_T(\ell_1) > 35\text{GeV}$.

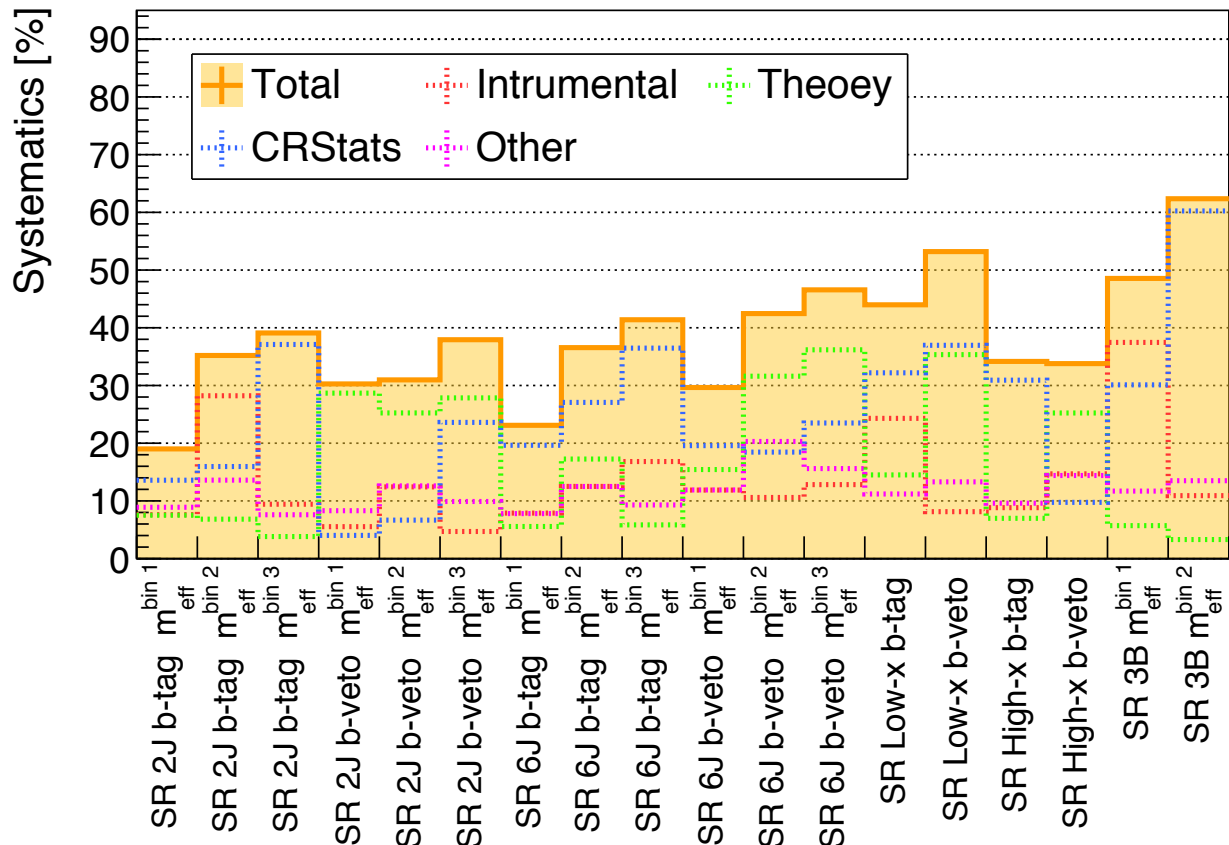


Figure 85:

8 Result

- 8.1 Procedure of Statical Analysis
- 8.2 Unblinded Signal Regions
- 8.3 Observed Constraints on SUSY Models.
 - 8.3.1 Constraints on Simplified Models.

Table 16:

SR 2J b -tag	$m_{\text{eff.}} \in [1100, 1500]$	$m_{\text{eff.}} \in [1500, 1900]$	$m_{\text{eff.}} > 1900$
Observed data	7	2	1
Expected background	8.39 ± 1.59	2.95 ± 1.04	2.21 ± 0.87
Di-leptonic	2.6 ± 1.2	0.9 ± 0.5	1.7 ± 0.8
$W + \text{jets}$	1.1 ± 0.7	0.3 ± 0.3	0.1 ± 0.0
$Z + \text{jets}$	0.8 ± 0.3	0.2 ± 0.1	0.1 ± 0.0
$t\bar{t}$	2.4 ± 0.5	0.9 ± 0.2	0.2 ± 0.1
Single-top	0.5 ± 0.1	0.2 ± 0.1	0.1 ± 0.0
Di-boson	$0.2^{+0.3}_{-0.2}$	$0.1^{+0.8}_{-0.1}$	$0.1^{+0.1}_{-0.1}$
$t\bar{t} + V$	0.8 ± 0.1	0.4 ± 0.1	0.1 ± 0.0
SR 2J b -veto	$m_{\text{eff.}} \in [1100, 1500]$	$m_{\text{eff.}} \in [1500, 1900]$	$m_{\text{eff.}} > 1900$
Observed data	21	8	6
Expected background	13.56 ± 3.87	6.78 ± 1.99	2.57 ± 0.97
Di-leptonic	1.1 ± 0.8	1.8 ± 1.2	$0.5^{+0.6}_{-0.5}$
$W + \text{jets}$	4.7 ± 1.3	1.9 ± 0.9	0.4 ± 0.2
$Z + \text{jets}$	2.3 ± 0.9	1.1 ± 0.4	0.7 ± 0.3
$t\bar{t}$	1.6 ± 0.6	0.5 ± 0.2	0.1 ± 0.1
Single-top	0.2 ± 0.1	0.0 ± 0.0	$0.0^{+0.0}_{-0.0}$
Di-boson	3.6 ± 3.3	1.5 ± 0.9	0.8 ± 0.7
$t\bar{t} + V$	0.2 ± 0.0	0.1 ± 0.0	0.0 ± 0.0
SR 6J b -tag	$m_{\text{eff.}} \in [1100, 1600]$	$m_{\text{eff.}} \in [1600, 2100]$	$m_{\text{eff.}} > 2100$
Observed data	7	2	0
Expected background	4.78 ± 1.10	2.29 ± 0.84	1.81 ± 0.75
Di-leptonic	2.3 ± 1.0	1.2 ± 0.6	1.2 ± 0.7
$W + \text{jets}$	0.4 ± 0.2	0.1 ± 0.1	0.2 ± 0.1
$Z + \text{jets}$	$0.0^{+0.0}_{-0.0}$	0.0 ± 0.0	$0.0^{+0.0}_{-0.0}$
$t\bar{t}$	1.0 ± 0.3	0.3 ± 0.1	0.1 ± 0.1
Single-top	0.1 ± 0.0	0.1 ± 0.0	0.1 ± 0.1
Di-boson	$0.1^{+0.2}_{-0.1}$	$0.3^{+0.4}_{-0.3}$	$0.0^{+0.1}_{-0.0}$
$t\bar{t} + V$	0.9 ± 0.2	0.3 ± 0.1	0.1 ± 0.0
SR 6J b -veto	$m_{\text{eff.}} \in [1100, 1600]$	$m_{\text{eff.}} \in [1600, 2100]$	$m_{\text{eff.}} > 2100$
Observed data	5	0	1
Expected background	3.90 ± 1.16	0.89 ± 0.38	0.45 ± 0.21
Di-leptonic	1.5 ± 0.8	$0.1^{+0.1}_{-0.1}$	0.0 ± 0.0
$W + \text{jets}$	1.1 ± 0.4	0.6 ± 0.3	0.3 ± 0.2
$Z + \text{jets}$	0.1 ± 0.1	0.0 ± 0.0	0.0 ± 0.0
$t\bar{t}$	$0.1^{+0.1}_{-0.1}$	0.1 ± 0.0	0.0 ± 0.0
Single-top	0.0 ± 0.0	0.0 ± 0.0	0.0 ± 0.0
Di-boson	1.0 ± 0.6	$0.1^{+0.2}_{-0.1}$	$0.1^{+0.1}_{-0.1}$
$t\bar{t} + V$	0.1 ± 0.0	0.0 ± 0.0	0.0 ± 0.0

Table 17:

SR Low-x	<i>b</i> -tag	<i>b</i> -veto
Observed data	0	3
Expected background	2.03 ± 0.89	1.56 ± 0.83
Di-leptonic	1.0 ± 0.6	0.6 ± 0.6
$W + \text{jets}$	0.1 ± 0.1	0.2 ± 0.1
$Z + \text{jets}$	0.0 ± 0.0	0.1 ± 0.0
$t\bar{t}$	0.5 ± 0.2	0.2 ± 0.1
Single-top	0.1 ± 0.1	0.1 ± 0.0
Di-boson	$0.2^{+0.5}_{-0.2}$	$0.5^{+0.5}_{-0.5}$
$t\bar{t} + V$	0.1 ± 0.0	0.0 ± 0.0

SR High-x	<i>b</i> -tag	<i>b</i> -veto
Observed data	6	3
Expected background	2.38 ± 0.81	3.27 ± 1.10
Di-leptonic	1.3 ± 0.8	0.3 ± 0.2
$W + \text{jets}$	0.4 ± 0.2	1.5 ± 0.5
$Z + \text{jets}$	$0.0^{+0.0}_{-0.0}$	0.5 ± 0.3
$t\bar{t}$	0.2 ± 0.1	0.1 ± 0.0
Single-top	0.1 ± 0.0	0.0 ± 0.0
Di-boson	0.1 ± 0.1	0.8 ± 0.8
$t\bar{t} + V$	0.3 ± 0.1	0.1 ± 0.0

Table 18:

SR 3B	$m_{\text{eff.}} \in [1000, 1750]$	$m_{\text{eff.}} > 1750$
Observed data	2	0
Expected background	1.61 ± 0.78	0.83 ± 0.52
Di-leptonic	1.0 ± 0.5	0.6 ± 0.5
$W + \text{jets}$	0.0 ± 0.0	0.0 ± 0.0
$Z + \text{jets}$	0.0 ± 0.0	0.0 ± 0.0
$t\bar{t}$	$0.4^{+0.6}_{-0.4}$	0.1 ± 0.0
Single-top	0.0 ± 0.0	$0.0^{+0.0}_{-0.0}$
Di-boson	0.0 ± 0.0	0.0 ± 0.0
$t\bar{t} + V$	0.2 ± 0.1	0.1 ± 0.0

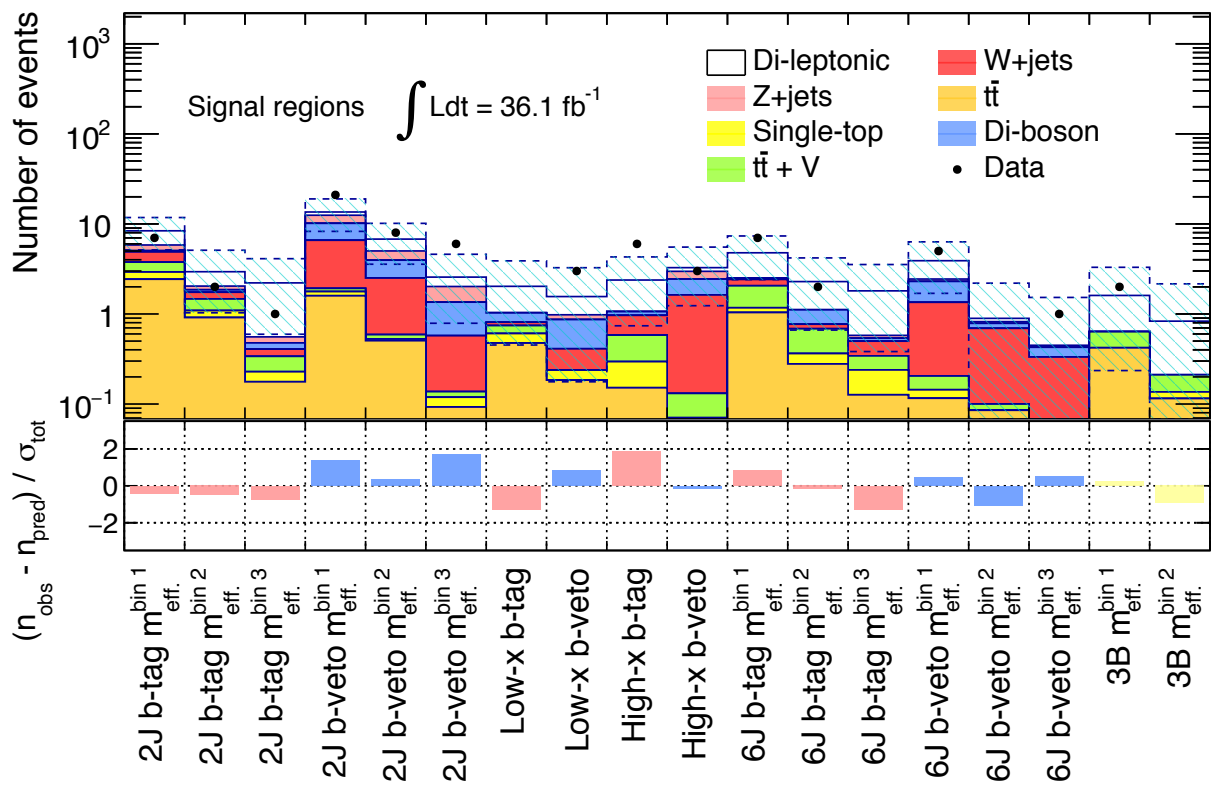


Figure 86:

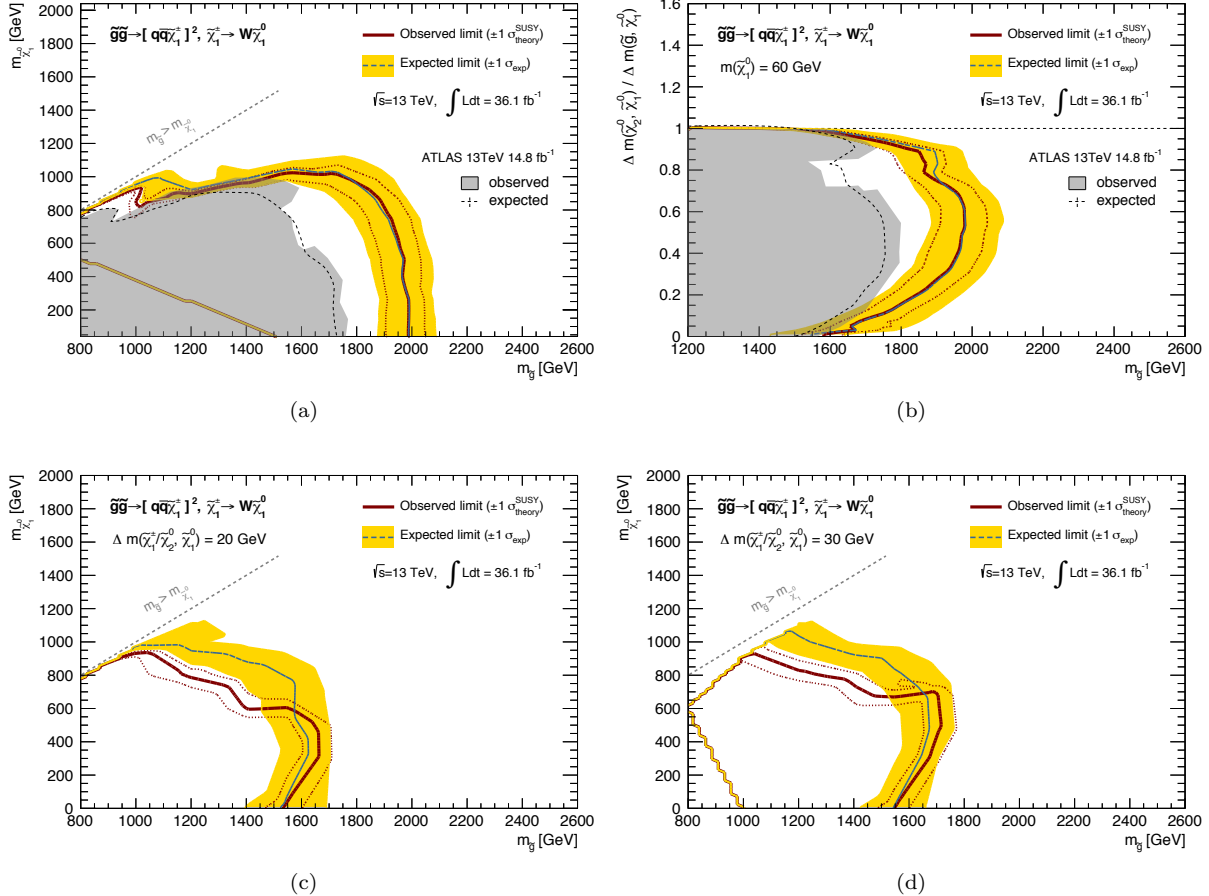


Figure 87: Projected exclusion limit (95% CL) for benchmark model **GG_onestepCC** onto the grids (a) $x = 1/2$ (b) $m_{\tilde{\chi}_1^0} = 60$ GeV (c) $\Delta m(\tilde{\chi}_1^\pm/\tilde{\chi}_2^0, \tilde{\chi}_1^0) = 20$ GeV (d) $\Delta m(\tilde{\chi}_1^\pm/\tilde{\chi}_2^0, \tilde{\chi}_1^0) = 30$ GeV.

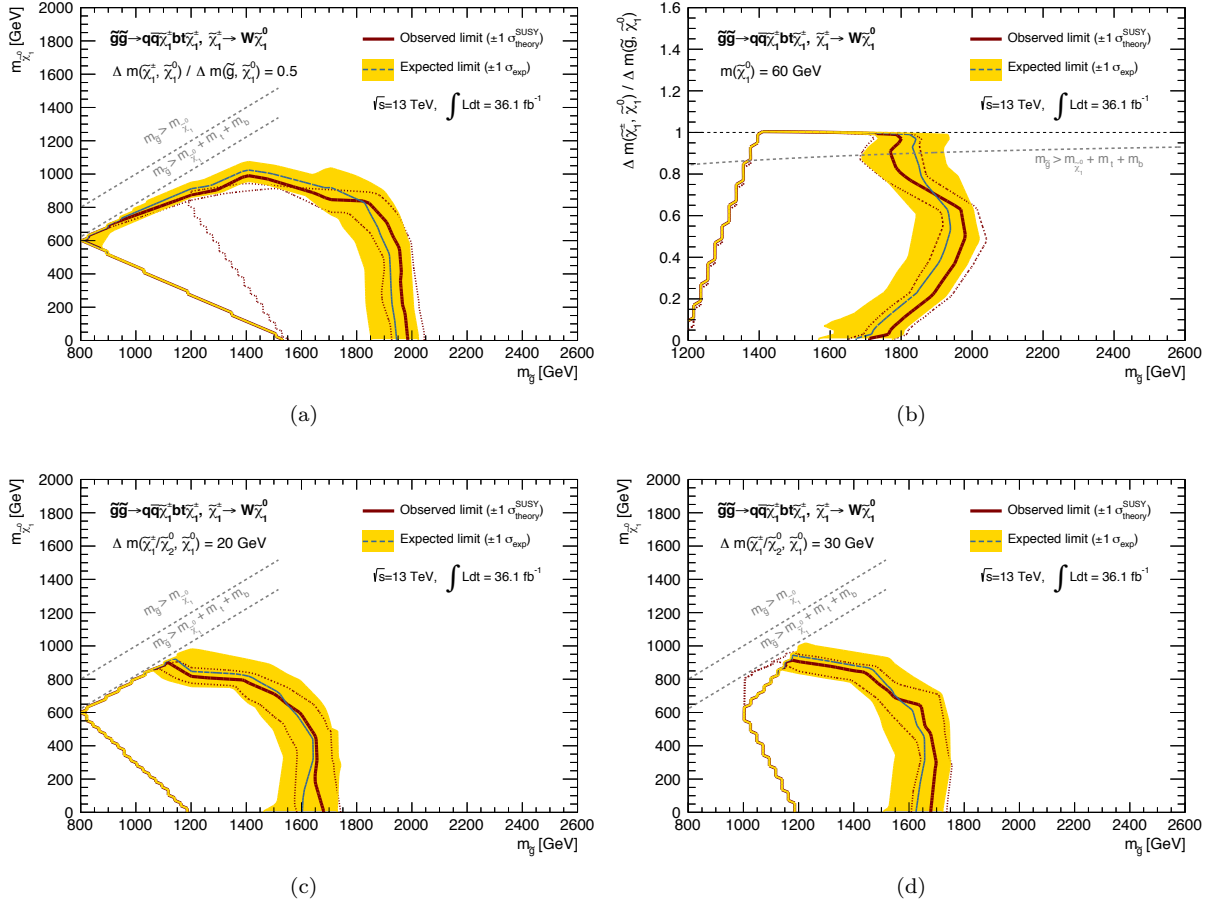


Figure 88: Projected exclusion limit (95% CL) for benchmark model **GG_QQC1BTC1** onto the grids (a) $x = 1/2$ (b) $m_{\tilde{\chi}_1^0} = 60 \text{ GeV}$ (c) $\Delta m(\tilde{\chi}_1^\pm, \tilde{\chi}_1^0) = 20 \text{ GeV}$ (d) $\Delta m(\tilde{\chi}_1^\pm, \tilde{\chi}_1^0) = 30 \text{ GeV}$.

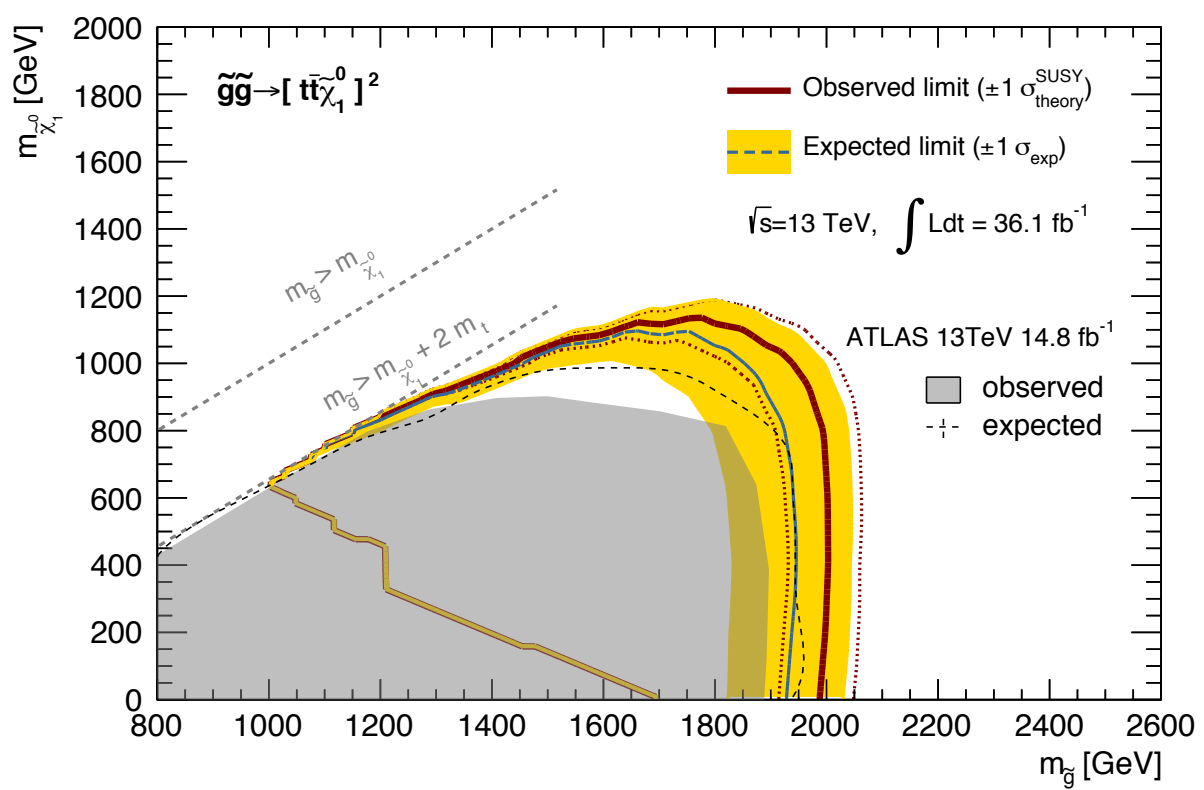


Figure 89: Exclusion limit (95% CL) for benchmark model **GG_ttn1**.